E.O. Paton Electric Welding Institute of the National Academy of Science of Ukraine
International Association “Welding”

The Paton Welding Journal

08
2025

International Scientific-Technical and Production Journal ♦ Founded in January 2000 (12 Issues Per Year)

Address of Editorial Office:
E.O. Paton Electric Welding Institute, 11 Kazymyr Malevych Str., 03150, Kyiv, Ukraine
E-mail: office@paton.kiev.ua; https://paton.org.ua/en/

Address of Publisher:
International Association “Welding”, 11 Kazymyr Malevych Str., 03150, Kyiv, Ukraine
Tel.: (38044) 205 23 90, E-mail: patonpublishinghouse@gmail.com; journal@paton.kiev.ua
https://patonpublishinghouse.com/eng/journals/tpwj

The Journal was registered by the National Council of Ukraine on Television and Radio Broadcasting on 09.05.2024, carrier identifier R30-04569
ISSN 0957-798X (Print), ISSN 3041-2293 (Online)
DOI: https://doi.org/10.37434/tpwj, from #01, 2020 to now; DOI: https: //doi.org/10.15407/tpwj from #01, 2014 to #12, 2019.

Subscriptions, 12 issues per year:
348 Euro — annual subscription for the printed (hard copy) version, air postage and packaging included;
288 Euro — annual subscription for the electronic version (sending issues in pdf format or providing access to IP addresses).

Representative Offices of “The Paton Welding Journal”:

BRAZIL, Arc Dynamics
Address: Nova Iguacu, Rio de Janeiro, Brazil
Daniel Adolpho, Tel.: +55 21 9 6419 5703,
E-mail: dadolpho@arcdynamics.com.br

CHINA, China-Ukraine Institute of Welding, Guangdong Academy of Sciences
Address: Room 210, No. 363 Changxing Road, Tianhe, Guangzhou, 510650, China
Zhang Yupeng, Tel.: +86-20-61086791,
E-mail: patonjournal@gwi.gd.cn

BULGARIA, Bulgarian Welding Society
Address: Blvd. Asen Yordanov No.10, Sofia 1592, Bulgaria
Pavel Popgeorgiev, Tel.: +359 899 96 22 20,
E-mail: office@bws-bg.org

POLAND, PATON EUROPE Sp. z o. o.
Address: ul. Kapitałowa 4, 35-213, Rzeszów, Poland
Anton Stepakhno, Tel.: +38067 509 95 67,
E-mail: Anton.Stepakhno@paton.ua

The content of the Journal includes articles received from authors from around the world in the field of welding, cutting, cladding, soldering, brazing, coating, 3D additive technologies, electrometallurgy, material science, NDT and selectively includes translations into English of articles from the following journals, published in Ukrainian:

- «Avtomatychne Zvaryuvannya» (Automatic Welding), https://patonpublishinghouse.com/eng/journals/as;
- «Suchasna Elektrometalurhiya» (Electrometallurgy Today), https://patonpublishinghouse.com/eng/journals/sem;
- «Tekhnichna Diahnostyka ta Neruinivnyi Kontrol» (Technical Diagnostics & Nondestructive Testing), https://patonpublishinghouse.com/eng/journals/tdnk.

CONTENTS

ORIGINAL ARTICLES

I.V. Ziakhor, Ye.V. Antipin, O.V. Didkovskyi, A.M. Levchuk, V.V. Kalyuzhny, V.V. Ozyumenko, P.M. Rudenko, Yu.A. Shylo
URGENT PROBLEMS OF WELDING RAILWAY RAILS UNDER MARTIAL LAW IN UKRAINE* 3

V. Kachynskyi, D. Allford, V. Klymenko
MIAB WELDING TECHNOLOGY OF PIPES AND PARTS OF AUTOMOTIVE INDUSTRY 19

V. Korzhyk, A. Grynyuk, O. Babych, O. Berdnikova, Ye. Illiashenko, O. Bushma
OBTAINING FUNCTIONALLY-GRADED METAL-MATRIX MATERIALS Ti–6Al–4V + WC IN THE PROCESS OF 3D PRINTING BY THE METHOD OF ADDITIVE PLASMA-ARC DEPOSITION 29

L.M. Lobanov, M.O. Pashchyn, O.L. Mikhodui, O.M. Tymoshenko
ELECTRODYNAMIC TREATMENT FOR THE CONTROL OF RESIDUAL STRESSES IN WELDED JOINTS MADE OF LIGHT, HEAT-RESISTANT ALLOYS AND AUSTENITIC STEEL* 37

I.V. Krivtsun, A.I. Momot, I.B. Denysenko, U. Reisgen, O. Mokrov, R. Sharma
MODEL OF THE ANODE BOUNDARY LAYER IN WELDING ARCS 44

L.M. Lobanov, O.V. Makhnenko, O.S. Milenin, O.A. Velykoivanenko, G.P. Rozynka, N.R. Basystuk, G.Yu. Saprykina
COMPUTER SOFTWARE FOR MODELING A CIRCUMFERENTIAL WELDED JOINT 55

O.I. Som
IRON-BASED BINDER ALLOY FOR PLASMA TRANSFERRED-ARC SURFACING OF COMPOSITE ALLOYS REINFORCED WITH CAST TUNGSTEN CARBIDES 68

INFORMATION

PATON INTERNATIONAL — EVOLUTIONS IN YEARS 75

*Translated Article(s) from “Avtomatychne Zvaryuvannya” (Automatic Welding), No. 4, 2025.

Indexing: The electronic edition of the Journal is stored in the V.I. Vernadsky National Library of Ukraine (eVerLib), included in the OPEN UKRAINIAN CITATION INDEX database and international databases: CROSSREF, EBSCO, Google Scholar, INDEX COPERNICUS, ULRICHSWEB.

DOI: https://doi.org/10.37434/tpwj2025.08.01

URGENT PROBLEMS OF WELDING RAILWAY RAILS UNDER MARTIAL LAW IN UKRAINE

I.V. Ziakhor[1], Ye.V. Antipin[1], O.V. Didkovskyi[1], A.M. Levchuk[1], V.V. Kalyuzhny[2], V.V. Ozyumenko[2], P.M. Rudenko[1], Yu.A. Shylo[1]

[1]E.O. Paton Electric Welding Institute of the NASU
11 Kazymyr Malevych Str., 03150, Kyiv, Ukraine
[2]Branch "Center for Track Construction and Repair" of the JSC "Ukrainian Railways"
5B Zaliznychne Shosse, 01103, Kyiv, Ukraine

ABSTRACT

Rail joining in stationary and field conditions is mainly performed by flash butt welding (FBW), which has been successfully used for many years on the railways of Ukraine and abroad. The article analyzes the critical challenges for ensuring the operability of the railway infrastructure under martial law in Ukraine. To solve urgent problems, the E.O. Paton Electric Welding Institute of the NAS of Ukraine (PWI) together with the Branch "Center for Track Construction and Repair" of the JSC "Ukrainian Railways" have developed a set of measures to ensure high-quality welding of rails in stationary and field conditions during the repair and construction of continuous welded rails in accordance with the requirements of acting regulatory documents. The results of works (research, technological, scientific and technical expertises) on the implementation of these measures for the period of 2022–2025 are presented. In particular, the technical condition of rail welding machines was successfully audited, the technology was improved and technological modes of FBW of railway rails were practiced, the system of quality assurance of joints during FBW of railway rails was improved, new revisions of regulatory documents for FBW of railway rails were prepared, the works are being conducted to update the design of FBW machines, cooperation with companies is developed to renew the production of rail welding equipment in Ukraine.

KEYWORDS: railway rails, welded joint, flash butt welding, railroad frog

INTRODUCTION

Continuous welded rail (CWR) is considered a progressive construction method for railway track superstructures in modern operations [1]. Rail joining in stationary and field conditions is mainly performed by flash butt welding (FBW), which has been successfully used for many years on the railways of Ukraine and abroad [2]. Since the 1950s, the PWI has been a world leader in the field of development of technologies and equipment for FBW of railway rails [3–5].

Under the general supervision of Academician B.E. Paton and the direct supervision of Academicians of the NAS of Ukraine V.K. Lebedev and S.I. Kuchuk-Yatsenko, PWI created the world's first highly efficient mobile equipment for FBW of railway rails in the field conditions. It is based on the original design of the secondary circuit of welding transformers with reduced short-circuit resistance and the technology of continuous flash butt welding with a programmable variation of the FBW process basic parameters. The unique welding equipment was created [4, 5], which, unlike the best foreign analogues, was distinguished by significantly smaller dimensions, lower weight and power consumption, high efficiency, and full automation of the welding process, which provided the ability to weld rails at the track laying location.

The first mobile rail welding machines were produced by PWI, and since 1961, the Kakhovka Electric Welding Equipment Plant has mastered the serial production of mobile (K155, K255, K255L, K355) and stationary (K190, K190M, K190PA) rail welding machines, which have successfully operated in Ukraine and dozens of countries on all continents [4]. The equipment and licenses for technological developments of PWI were purchased by a number of leading foreign companies, including Plasser & Theurer (Austria), Holland and Progress Rail Services (USA), Network Rail (UK). When travelling by rail in Ukraine, the USA, China, the European Union and many other countries, most passengers do not realize that the welded rail butts are made using technologies and equipment developed at PWI. This also applies to subway tracks in Kyiv, Washington, New York, Singapore, Shanghai, Beijing, Bangkok and other cities. Rail welding enterprises of the JSC "Ukrainian Railways" use exclusively technologies and equipment for FBW developed by PWI.

In the 2000s, based on the results of fundamental research, PWI developed and implemented the technology for FBW of rails with pulsating heating mode (pulsating flashing), designed and mastered the production of a new generation of mobile (K900, K920, K921, K922, K930, K945, K950, K960, K963, K1045) and stationary (K1000, K924) rail welding

machines. They are the first in the world to implement a number of innovative technical solutions protected by international patents in the field of welding technology, design of welding machines, principles of rail alignment, FBW process control systems and quality testing of rail welded joints [6–10].

The russian military invasion of Ukraine in 2022 led to a number of critical challenges for ensuring the operability of the railway infrastructure under martial law. These challenges include the suspension of domestic rail production by Azovstal Metallurgical Combine as a result of the occupation, which has raised the issue of welding used [11]and new [12–17] rails of different grades and manufacturers, with various heat treatment modes, in particular, in a heterogeneous combination; suspension of production of domestic rail welding equipment by Kakhovka Electric Welding Equipment Plant (KZESO PJSC), which led to the disruption of the delivery of a stationary K924 machine for FBW of railroad frogs to JSC "Dnieper Railway Switch Plant" and eight newest KSM007 rail welding complexes equipped with K922-1 machines to the JSC "Ukrainian Railways", and necessitated an urgent solution to the problem of extending the operational life of existing welding equipment.

To solve the above problems, PWI together with the Branch "Center for Track Construction and Repair" (CTCR) of the JSC "Ukrainian Railways" developed a set of measures to ensure high-quality rail welding in stationary and field conditions during the repair and construction of CWR in accordance with the requirements of acting regulatory documents [11–13]. The mentioned set of measures includes organizational, research, design and technological works, scientific and technical expertise.

The following tasks were identified as the most urgent and priority ones:

- establishing the causes for the non-compliance of some welded joints of railway rails of different grades and plants-manufacturers with the requirements of regulatory documents;
- audit of the technical condition of rail welding equipment available at the JSC "Ukrainian Railways" and development of measures to extend its operational life;
- improvement of technology and optimizing technological modes for FBW of railway rails of converter production;
- improving the quality assurance system for joints during FBW of railway rails;
- preparation of recommendations and amendments to existing regulatory documents, development of a new revision of technical specifications for FBW of railway rails;
- improving the design of mobile rail welding machines;
- search for companies that have the production capacity to renew the production of FBW equipment.

THE AIM

of the article is to provide brief information on the results of works for the period of 2022–2025 to implement the developed set of measures for ensuring high-quality welding of railway rails under martial law in Ukraine.

ESTABLISHING OF THE CAUSES OF NON-COMPLIANCE OF SOME WELDED TO JOINTS OF RAILWAY RAILS WITH THE REQUIREMENTS OF REGULATORY DOCUMENTS

At the request of the Branch "CTCR" of the JSC "Ukrainian Railways", PWI specialists performed scientific and technical expertise of the causes for non-compliance of welded joints of rails of various grades from different manufacturers with the requirements of regulatory documents, in particular, during their mechanical tests in accordance with the requirements of acting standards [11–13]. Based on the results of in-process control, analysis of welding protocols, macroanalysis and metallographic examinations of rail joints, fractographic examinations of fractures of rail welded joints, the causes of their fracture during mechanical tests for static bending and under cyclic loads during the operation of the railway track were determined. The methods of macroanalysis, microanalysis, hardness (NOVOTEST TC-GPB) and microhardness (M400, Leco) measurements, optical microscopy (Neophot-32), scanning electron microscopy (SEM), energy dispersive X-ray microanalysis (EDXMA), Auger electron spectroscopy (Auger-microprobe JAMP-9500F, JEOL with built-in EDS spectrometer OXFORD EDS INCA Energy 350) were used [18].

As an illustration of the scope of the complex of works carried out in this area, below is a fragment of the report of the scientific and technical expertise of the causes for non-compliance with the requirements of regulatory documents (fracture during static bending tests) of the welded joint of R65 type rails of E76F grade, made by continuous FBW using K355 mobile rail welding machine. The subject of the study is the defects in the rail foot according to code 66.3 and the defect in the rail web according to code 56.3 detected at the fracture (Figure 1) of the rail welded joint [19].

The fracture of a rail welded joint butt is heterogeneous in terms of the macrogeometry of the fracture surface [20], since it has geometric zones with different macrorelief of the fracture surface. According to the surface condition and fracture micromechanism, the fracture in the head and the bulk part of the web and foot is crystalline, quasi-brittle and intergranular [21, 22].

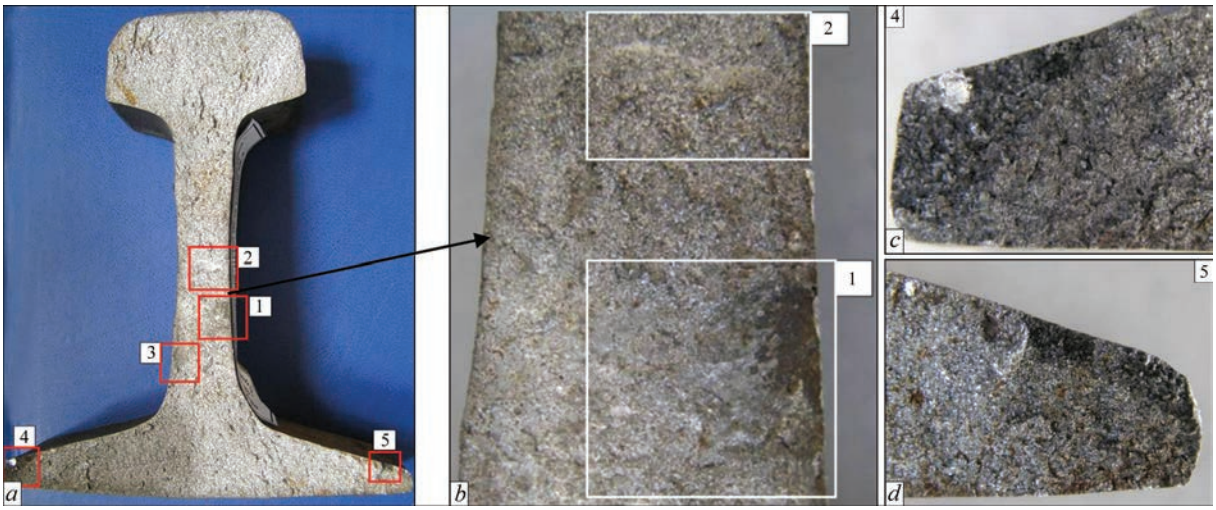

Figure 1. Fracture of welded rail (*a*), defects in the rail web (*b*) and foot (*c*, *d*)

Defects in the form of dark spots without metallic luster and signs of crystalline fracture (Figure 2) are observed in the rail web at fracture regions Nos 1, 3 (see Figure 1, *a*). The total area of these defects is about 60 mm^2, which indicates that the rail welded joint does not meet the requirements [11–13].

The chemical composition of the dark areas approximately corresponds to the composition of iron oxide FeO (Figure 2, *b*). According to [21], this type of defect can be attributed to group 4 "Lack of fusion" of subgroup P401 "No weld» or subgroup P403 "Insufficient fusion (stuck weld)". The most probable cause for the formation of such defects is a violation of the flashing process before upsetting at the stage of intensive flashing.

In region 2 of the fracture, a defect of 0.3–2×10 mm in size was found in the rail web (Figure 3, *a*) in the form of a light spot with a metallic luster without signs of crystalline fracture. The defect is elongated in the transverse direction of the web; its total area is about 18 mm^2, which exceeds the admissible maximum value according to [11–13]. The fracture surface in regions 2 and 3 has no signs of crystalline fracture, has the appearance of a locally melted surface with a slight metallic luster, the main component is iron (about 85 %) with a small oxygen content (about 6 %). In terms of chemical composition, numerous inclusions located on the surface of the defect correspond to ferromanganese silicates present in the base metal of rail steel, which indicates their metallurgical origin [23].

Metallographic examinations of regions of the heat-affected zone (HAZ) adjacent to the welded butt fracture revealed that the total width of the HAZ significantly exceeds the requirements of [17], which regulates the admissible value of the HAZ width within 20–45 mm. The significant increase in the HAZ width compared to the requirements of [17] could be caused by several factors, namely: rails overheating (excessive heat input into the welded butt), long-term

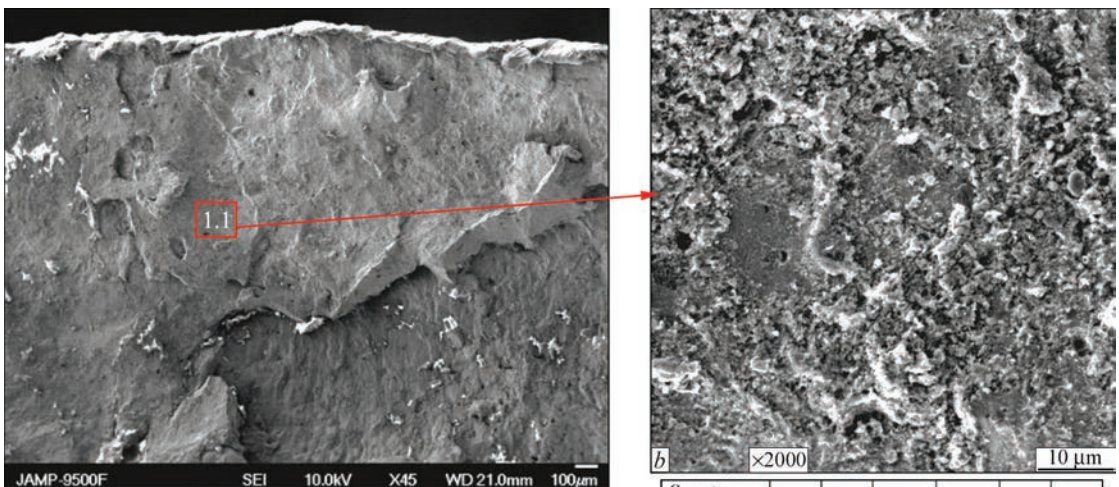

Spectrum, at.%	C	N	O	Fe	Ca	S
2	6.0	1.5	48.8	43.0	0.6	0.1

Figure 2. SEM images of fracture regions No. 1 (*a*) and No. 1.1 (*b*) after ion etching with Ar+ ions at 3 keV to a depth of 60 nm, Auger spectrometry results of region No. 1.1

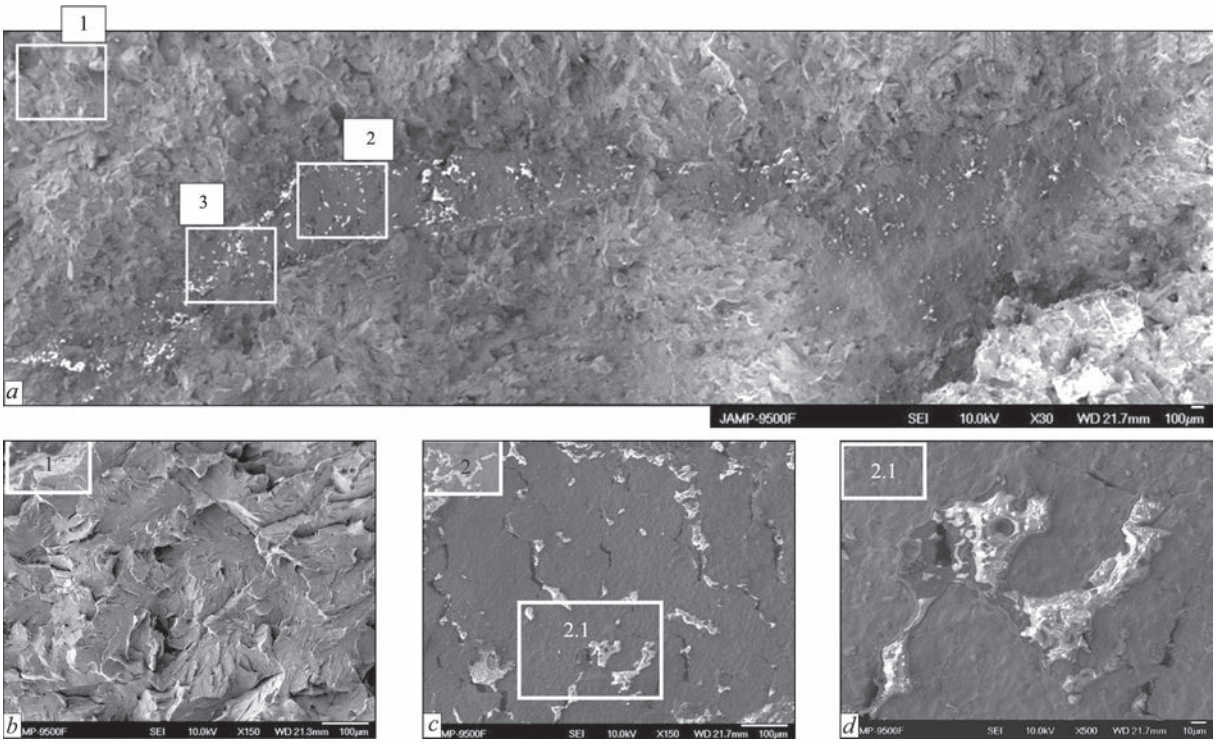

Figure 3. SEM images of the fracture surface in region 2 (see Figure 1): (*a*) and locations 1, 2 and 2.1 (*b*, *c*)

short circuit of rail ends during flashing, excessively long flashing process.

Defects were detected in the fracture regions of the rail foot (Figure 1, *c* — regions 4, 5), which are defects of group 3 "Solid inclusions", P306 "Inclusion of cast metal (Solidified residual molten material enclosed in the joint including impurities)" [21].

Defects in rail foots (group 3, P306) are relatively hard to detect with existing ultrasonic flaw detectors after welding a joint, as they have a monolithic structure of overheated metal oxidized along the grain boundaries without any cavities. During ultrasonic inspection with existing flaw detectors, such defects can be interpreted as structural noise.

The probable causes for the formation of the above defects and the non-compliance of the rail welded joint with regulatory requirements [11–13, 17] are the combination of several factors, in particular, excessive heat input into the rail welded joint, local oxidation of rail ends at the stage of intensive flashing, and the penetration of overheated metal into the joint plane when cutting burr. It was revealed that the zone of initial crack propagation and welded rail welded joint fracture were caused by defects in the rail foot; rail welded joint fracture was caused by the location of defects in the tensile stress zone.

The main results of scientific and technical expertises of the causes for non-compliance of rail welded joints with the requirements of regulatory documents are presented in the conclusions, which include the classification of rail welded joint fracture by macrogeometry of the fracture surface, fracture characteristics by surface condition and fracture micromechanism, classification of defects, conclusions on compliance of the rail welded joint with regulatory requirements, substantiation of probable causes of defects and causes of rail welded joint fracture, assessment of the possibility of detecting existing defects by ultrasonic inspection methods.

Based on the results of scientific and technical expertises of welded joints of R65 type rails of various grades (E76F, K76, K76F, R350HT) and of different plants-manufacturers, produced by mobile rail welding machines K355, K900, K922-1 during 2024–2025, PWI experts developed recommendations to prevent arising of defects in rail welded joints and to reliably detect probable defects during non-destructive testing of joints, as well as a list of practical measures for their implementation. The main measures to prevent defective welded joints in the CWR are the improvement of technology and optimizing technological modes of FBW of rails of different grades, strict compliance by personnel with the requirements [11–13] for auxiliary and welding works; the use of welding machines equipped with systems for recording the basic parameters of the FBW process; monitoring of rail welding technology based on electronic reports from rail welding enterprises of the JSC "Ukrainian Railways". The use of phased array technology for ultrasonic inspection of rail welded joints is also recommended.

AUDIT OF THE TECHNICAL CONDITION OF RAIL WELDING EQUIPMENT

During the reporting period, PWI specialists conducted an audit of the technical condition of welding ma-

Figure 4. Mobile K922-1 machines as part of rail welding KZM 005 (*a*), KZM 007 (*b*) and KRZ 1 (*c*) complexes

chines at all rail welding enterprises (RWE) of the JSC "Ukrainian Railways", in particular, stationary K1000 and mobile K355A, K900, K920 and K922-1 machines. As a result of the performed works, the existing problems listed in the technical condition reports of the equipment were identified; together with the Branch "CTCR" of the JSC "Ukrainian Railways", a set of measures was developed to maintain the specified technical characteristics and extend the operational life of rail welding machines as part of KZM 005, KZM 007, KRZM 3, KRZM 4 and KRZ 1 complexes (Figure 4), new contracts for similar works were concluded, and fruitful cooperation in this area continues.

IMPROVEMENT OF TECHNOLOGY AND OPTIMIZING TECHNOLOGICAL MODES OF FBW OF RAILWAY RAILS OF CONVERTER PRODUCTION

After Azovstal Metallurgical Combine suspended the production of domestic rails in 2022 as a result of the occupation of Mariupol, Ukrainian railways began the use of R65 (60EI) rails of converter production of various grades with different heat-treatment modes, which are purchased from different manufacturers and received as humanitarian aid. Rail welding enterprises of the JSC "Ukrainian Railways" together with PWI had to solve the problem of improving the technology and optimizing technological modes of FBW of rails of different grades (R350HT, R350LHT, R400HT), in particular, in a heterogeneous combination, in short terms. A similar problem arose with used rails of open-hearth and converter production of M76, E76, E76F, K76 and K76F grades, which, when laying in the railway track, must be welded together and in a heterogeneous combination.

In previous years, the technological modes of FBW of rails were determined experimentally for the available type of rails and a specific rail welding machine. The requirements of acting regulatory documents [11–13] regulate the admissible ranges of variation in certain parameters of FBW of rails, in particular, the voltage of the primary circuit of welding transformers and the value of displacement at different stages of the FBW process, upsetting pressure, displacement rate during flashing, forcing and upsetting, time of upsetting under current, etc. Based on the analysis of the results of many years of practical experience in FBW of rails at rail welding enterprises of the JSC "Ukrainian Railways", mechanical tests and metallographic examinations of welded joins, it was found that ensuring the technological parameters of FBW within certain limits is a necessary but not sufficient condition for producing welded joints of rails that meet the requirements [11–13].

Moreover, ensuring the compliance of rail welded joints with the requirements of the national standard [17], harmonized with the relevant European regulatory document, provides for certain parameters of the HAZ, namely: the admissible range of HAZ width values (minimum $H_{\text{HAZ min}}$ and maximum $H_{\text{HAZ max}}$ values) and its nonuniformity along the length and cross-section of the rails, and additionally contains

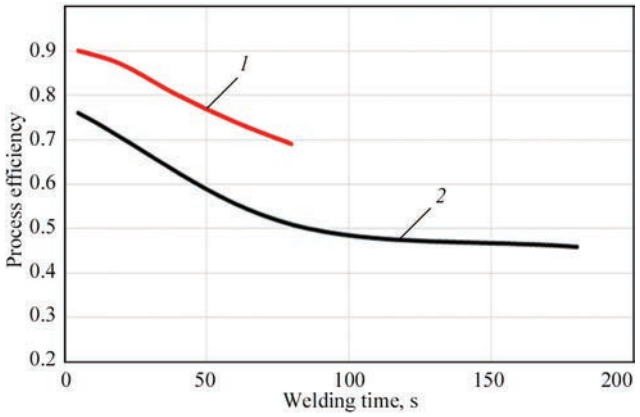

Figure 5. Variation in efficiency over time at FBW: *1* — PF; *2* — CF (calculated data)

requirements for the microstructure of the metal in the HAZ — there shall be no evidence of martensite or bainite at 100× magnification in the visible heat affected zone.

The development and approval of the FBW mode for each rail grade in a specific rail welding machine required conducting a complex of works, including mechanical testing, metallographic and factographic examinations, non-destructive testing, determination of hardness distribution, etc. Until now, no reliable algorithm has been determined to ensure the quality of welded rail joints at varying external factors (condition of the welding machine, diesel generator parameters, quality of rail end preparation, etc.). The development of the mentioned algorithm for rail joint quality was based on the idea of Academician of the NASU S.I. Kuchuk-Yatsenko to use the value of the total heat input Q_{fl} in the rail flashing process as a complex parameter that takes into account the influence of other energy parameters of the FBW process on the temperature distribution in the HAZ, microstructure formation and mechanical properties of welded rail joints. The implementation of this idea consisted in determination and scientific substantiation of the range of changes in Q_{fl} during FBW of modern rails of converter production, which ensures that welded joints meet the requirements of acting standards. From a practical point of view, this will

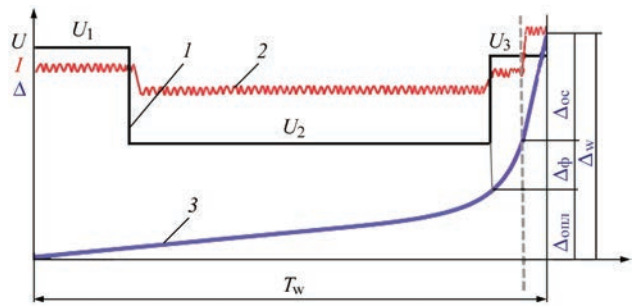

Figure 6. FBW process cyclogram with a programmable primary voltage variation: *1* — voltage, *2* — current, *3* — welding allowance

significantly reduce the time and scope of research and testing when developing and optimizing FBW process modes for different rail grades, regardless of the electric mains parameters, condition of the rail welding machine, etc. Below is a brief description of the conducted research and the obtained results.

The calculations of variation in the thermal efficiency of the rail heating processes at continuous flashing (CF) and pulsating flashing (PF) established that at CF of rails, the value of the efficiency decreases from 0.7 (in the initial period) to 0.45 at t_{fl} = 180 s, and at PF, the efficiency decreases from 0.9 in the initial flashing period to 0.7 at t_{fl} = 80 s (Figure 5). Our calculations substantiate the use of PF as a basic process in the development of an efficient FBW technology for modern railway rails of converter production.

A computational study of heating R65 (60E1) type rails at PF with a programmable voltage U variation (Figure 6) at different stages of the flashing process was carried out.

Mathematical models and appropriate computer simulation tools for the kinetics of temperature fields during FBW of railway rails were developed jointly with the Department 34 of PWI. The numerical solution of the nonstationary thermal conductivity equation was used along with a set of necessary laboratory measurements of the influence of FBW process parameters on temperature cycles in the welded rails. This made it possible to take into account the multiphysical processes of rail end flashing and determine the characteristic thermal efficiency of the FBW process.

The mathematical model was used to calculate the thermal cycles and temperature distribution in the HAZ during FBW of R65 type rails of K76F grade. When performing the calculations, the values of the basic parameters of FBW modes (Table 1) were set within the limits provided for in [13].

To assess the reliability of the mathematical model, experimental studies of thermal cycles were carried out and the temperature distribution in welded joints produced by FBW was determined according to Table 1. Experiments to study thermal cycles at FBW were performed in stationary K1000 and mobile K922-1 machines (Figure 7). A system of thermocouples was used, mounted in the rail head at different distances from the rail end in a step of 5 mm. The first thermocouple was placed at a distance of 18 mm from the rail end, which involved placing it at a distance of 5 mm from the joint line (JL) after the FBW process.

A comparative analysis of the calculated and experimental data of the study of thermal cycles during flashing (Figure 8) shows that the mathematical model has a calculation error of about 8 %, which makes it possible to predict the kinetics of the temperature field

Table 1. FBW mode of K76F rails

Parameter	Value
Primary voltage at different stages of flashing U, V	$U_1 = 400$, $U_2 = 305$, $U_3 = 400$
Mean value of the primary current I at different stages of flashing, A	$I_1 = 420$, $I_2 = 380$, $I_3 = 420$
Total flashing time t_{fl} ($t_{1,2,3}$ – by stages), s	$T_{fl} = 80$ ($t_1 = 30$, $t_2 = 45$, $t_3 = 5$)
Upsetting time under current, s	1
Total displacement for total flashing Δ_{fl} ($\Delta_{1,2,3}$ – by stages), mm	14 ($\Delta_1 = 3$, $\Delta_2 = 7$, $\Delta_3 = 4$)
Upsetting value Δ_{ups}, mm	12
Calculated heat input value Q_{fl}, MJ	12.8

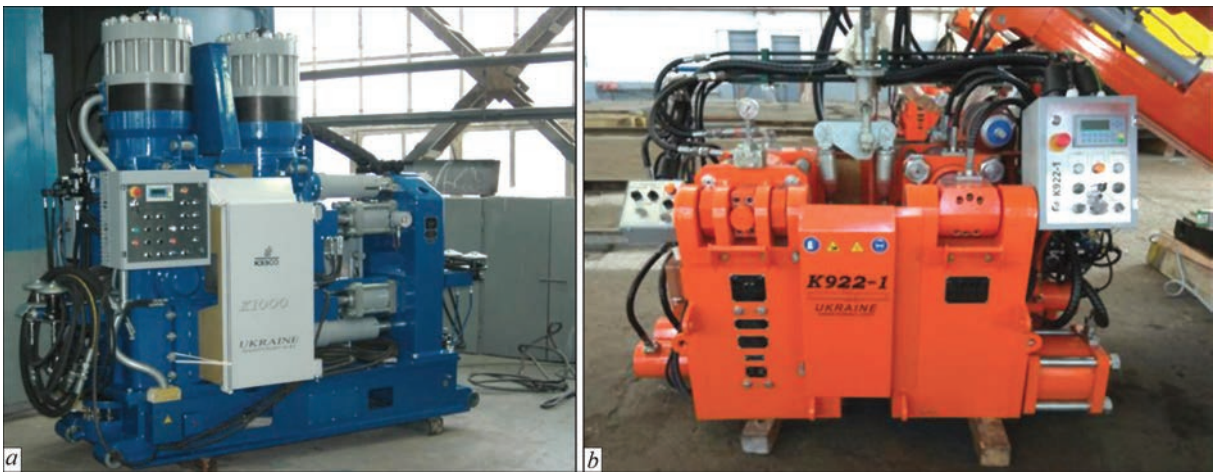

Figure 7. Rail welding K1000 (*a*) and K922-1 (*b*) machines

in rails at FBW with satisfactory accuracy. This makes it possible to use a mathematical model to study the influence of the basic FBW parameters on the heating and cooling processes of rail welded joints. It was found that the maximum value of the cooling rate in the welded joint and HAZ is achieved along the JL, where the heating temperature in the FBW process was maximum.

Using the developed mathematical model, the effect on the efficiency of the heating process and the temperature distribution in the welded joint zone of R65 (60E1) type rails of the FBW process parameters was studied, namely: the primary voltage U of the power source at different stages of the flashing process (U_1–U_3), the allowance Δ_f of the progressive flashing stage, the flashing duration t_{fl}, and the value of the heat input Q_{fl}). The temperature distribution along the axis of the rail welded joint at FBW with different values of voltage U at stage 2 of the process is shown in Figure 9.

Based on the obtained results, the use of the FBW process with a programmable variation of the power supply voltage in time is substantiated, the cyclogram of the flashing process is specified, which provides for a stage-by-stage variation of U in the range U_1 = 355–440 V at the first stage of flashing, in the range U_2 = 250–300 V at the second stage (quasi-stationary heating), and within U_3 = 355–440 V at the third stage (progressive flashing).

The temperature distribution along the axis of the welded rail joint at FBW at different flashing process duration t_{fl} was determined. The calculation results for t_{fl} = 90 and 120 s are shown in Figure 10. The criteria for selecting the minimum allowable t_{fl} was to achieve a temperature distribution along the axis of the flashed rails, at which the conditions for upsetting by a set

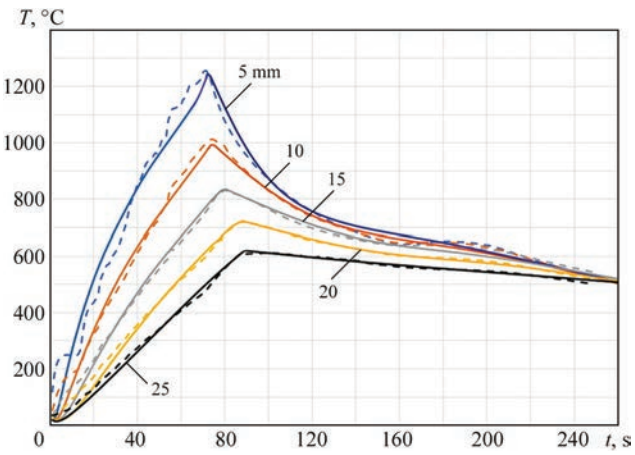

Figure 8. Calculated (dashed lines) and experimental (solid lines) thermal cycles at FBW of R65 (60E1) rails of K76F grade at different distances from the JL

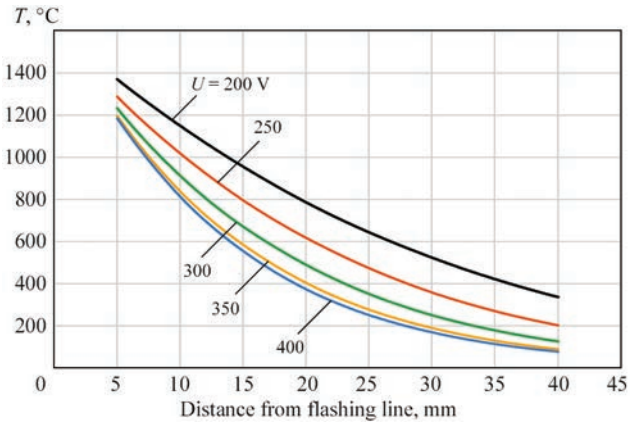

Figure 9. Temperature distribution along the axis of the welded rail joint at FBW with different voltage *U* at stage 2 of the flashing process (see Figure 6)

value of upsetting displacement Δ_{ups} = 12 mm (the width of the HAZ with a heating temperature of up to 1000 °C should exceed Δ_{ups} = 12 mm) are ensured. As is seen from the obtained data, for t_{fl} = 90 s and more, the above condition is met.

The dependence of the minimum $H_{HAZ\ min}$ and the maximum $H_{HAZ\ max}$ values of the welded joint HAZ width (according to the requirements of [17]) on the duration of the flashing process t_{fl} in the range from 50 to 140 s was determined by calculations. It was established that during PF of railway rails of R65 (60E1) type, with an increase in t_{fl} in the range from 50 to 140 s, the value of heat input Q_{fl} varies in the range of Q_{fl} = 9–18 MJ, while the value of $H_{HAZ\ min}$ increases from 16 to 22 mm, and the value of $H_{HAZ\ max}$ — from 36 to 54 mm.

An important parameter of the thermal cycle in FBW of rails is the cooling rate $W_{8/5}$ of the welded joint metal in the temperature range of 800–500 °C. This parameter determines the presence or absence of hardening structures, pearlite dispersion, strength and hardness indices in the HAZ of the welded joint. The dependence of the cooling rate $W_{8/5}$ of welded joints

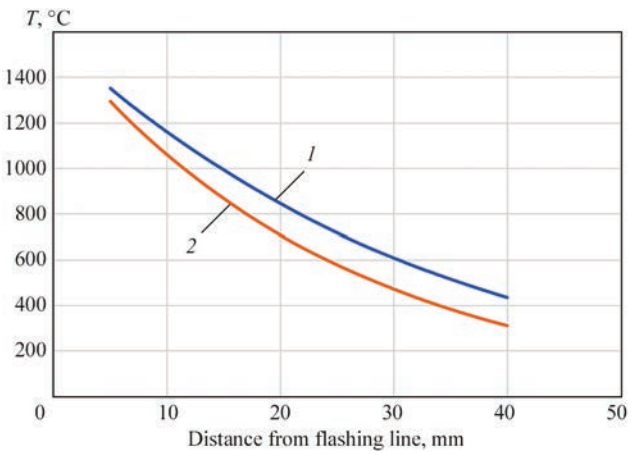

Figure 10. Temperature distribution along the axis of the welded rail joint at FBW with different value of flashing time t_{fl}, s: *1* — 120; *2* — 90

after FBW of R65 (60E1) type rail of K76F grade on the value of Q_{fl} was studied by calculation. When calculating the cooling rate $W_{8/5}$ of metal in the HAZ of the joints, the value of Q_{fl} varied within the above limits, namely: t_{fl} = 50–140 s, Q_{fl} = 9–18 MJ.

To evaluate the structural state of the metal in the HAZ of R65 rail joints of K76F grade, the continuous cooling transformation diagram (CCT diagram) of K76F rail steel was used [14]. The aim of the study was to determine the range of changes in the value of heat input Q_{fl}, in which there are no hardening structures (martensite) in the welded joint of rails, the pearlite structure of the HAZ metal is ensured, and hardness values are achieved in accordance with the requirements [11–13, 17]. During the calculations, the values of current, flashing displacement and time, upsetting displacement and heat input were set for three different FBW modes (Table 2). The calculated temperature distribution in the HAZ of joints at FBW of R65 (60E1) rails of K76F grade for modes 1–3 is shown in Figure 11.

To assess the structural state of the metal in the HAZ of rail joints, the calculated cooling curves (logarithmic time scale) for different FBW modes were superimposed on the continuous cooling transformation diagram of K76F rail steel. The CCT diagram of K76F steel with the maximum carbon content within the regulatory requirements [24] and the calculated cooling curves of joints for the value of heat input Q_{fl} = 9.0, 9.7, 12.6 and 16.2 MJ at FBW are shown in Figure 12. Analysis of the data in Figure 12 shows that for Q_{fl} = 9 MJ (within mode 1), the maximum cooling rate along the JL is $W_{8/5}$ = 8.7 °C/s, the cooling curve is partially contained within the bainite region, and the hardness value reaches 395 *HV*30. The presence of bainite in the structure of the to ints of rail welded joint metal is not allowed, therefore, mode 1 at a value Q_{fl} = 9 MJ is unacceptable according to the criterion of the structural state of the metal in the joint zone when examining the microstructure [17]. For Q_{fl} = 12.6 MJ (within mode 2), the cooling rate along the JL is $W_{8/5}$ = 3.75 °C/s, the cooling curve is within the pearlite transformation region, the hardness value reaches 380 *HV*30, which meets the

Table 2. FBW modes of R65 rails of K76F grade

Parameter	Values for FBW modes		
	Mode 1	Mode 2	Mode 3
Flashing time t_{fl}, s	50–60	70–90	110–140
Flashing current *I*, A	370-390		
Flashing displacement Δ_{fl}, mm	7–8	9–12	14–15
Value of heat input Q_{fl}, MJ	9–10.8	11.5–14.0	14.4–18

requirements of acting regulatory documents. For Q_{fl} = 16.2 MJ (within mode 3), the cooling rate along the JL is $W_{8/5}$ = 2.75 °C/s, the cooling curve is completely within the pearlite transformation region, and the hardness value reaches 368 *HV*30. Consequently, during FBW at modes 2 and 3, rail welded joints meet the regulatory requirements in terms of the structural state of the metal in the joint zone [17].

Thus, the minimum values of the flashing time $t_{fl.mi}$ = 55 s and heat input $Q_{fl.min}$ = 9.7 MJ at FBW of heat-strengthened K76F rails with a maximum carbon content within the regulatory requirements, at which the cooling rate along the JL does not exceed $W_{8/5}$ = 7.0 °C/s and the absence of bainite and martensite in the joint zone is ensured, were determined by calculation.

The technological modes of FBW of R65 (60E1) type rails of K76F and R350HT grades were optimized based on the results of mechanical tests and metallographic examinations. Bend testing [11–13, 17] of welded rail joints made using different FBW modes were performed (see Table 2). The test results are shown in Tables 3 and 4.

Obviously, only mode 2 meets the regulatory requirements for the values of bend test deflection and force of welded K76F and R350HT rail joints. After the bend testing of welded K76F rail joints produced by FBW at mode 1, fracture analysis was performed. Defects are observed in the fractures (Figure 13), which are defined as "flat spots" [23, 25, 26] with a total area of more than 15 mm^2, which do not correspond to [11–13]. FSs are distinguished on the fracture surface by an undeveloped relief and are gray in color. In the structure of FSs, there are numerous

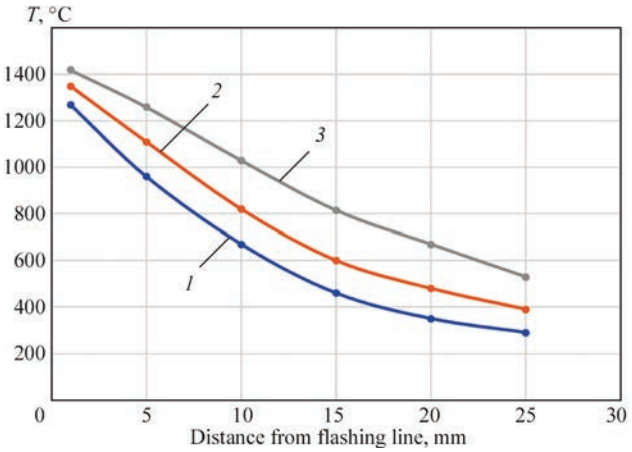

Figure 11. Temperature distribution in the HAZ before upsetting at PF of R65 (60E1) rails at modes *1–3*

melted inclusions (Figure 13), which are based on particles of complex oxides several microns in size, which include manganese, silicon.

An increase in the heat input during FBW (mode 3) leads to a decrease in indices of bend test rail welded joints. This is primarily predetermined by an increase in the grain size along the JL and in the HAZ and the development of the process of pre-eutectoid ferrite precipitation along the boundaries of primary austenitic grains [25]. Thus, mode 3 (t_{fl} = 110–140 s, Q_{fl} = 14.4–18 MJ) does not meet the requirements [11–13], although it is acceptable according to the micro examination requirements of the rail welded joints [17]. At FBW at mode 2, the regulatory requirements for welded joints of rails of K76F and R350HT grades are met by both criteria: structural state of the metal and indices of mechanical properties of joints during bending tests.

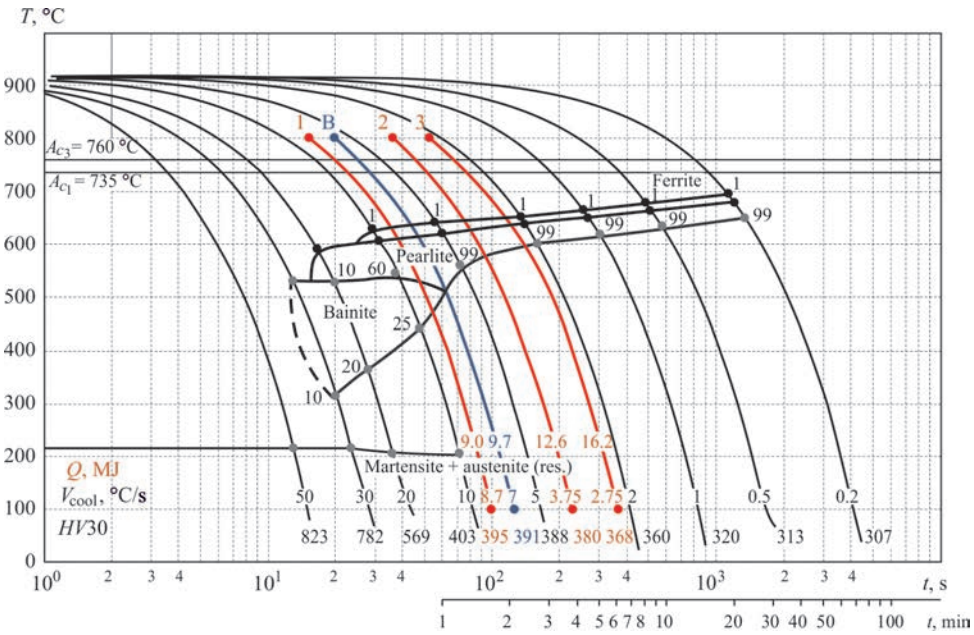

Figure 12. CCT diagram of K76F steel [24] and calculated curves of cooling rails made by FBW with different value of heat input Q_{fl}, MJ

Table 3. Test results of welded joints of R65 rails of K76F grade

Mode number	Bend test force, kN	Bend test deflection, mm
Requirements [13]	≥1650	≥30
Mode 1	1950–2250 1950	27–32 28
Mode 2	2000–2300 2150	35–45 38
Mode 3	1800–2000 1900	25–34 29

Table 4. Test results of welded joints of 60E1 rails of R350HT grade

FBW mode	Bend test force, kN	Bend test deflection, mm
Requirements [13]	≥1650	≥30
Mode 1	1900–2100 1900	27–31 28
Mode 2	2100–2350 2200	34–41 37

Metallographic examinations of welded joints of K76F and R350HT rails produced by FBW at mode 2 were performed. The macrosection, microstructure, SEM image of the metal in the joint zone and the hardness distribution for the joint of R350HT rails are shown in Figure 14. Within the HAZ, a decrease in hardness to 280 *HV* 30 is observed, which is predetermined by the process of cementite spheroidization in the zone of partial recrystallization. This is typical

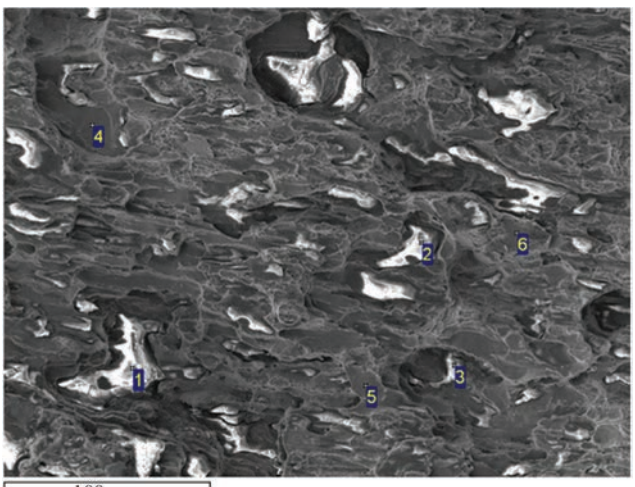

Spectrum	C	O	Al	Si	Cr	Mn	Fe
1	1.51	46.66	0.00	22.15	0.00	24.77	4.90
2	20.02	43.54	0.23	15.99	0.11	17.14	2.96
3	1.50	37.53	0.06	20.94	0.08	33.93	5.73
4	1.83	0.54	0.00	0.40	0.00	0.76	96.47
5	2.12	1.49	0.08	0.46	0.06	1.65	94.13
6	0.87	0.52	0.00	0.27	0.00	0.08	98.26

Figure 13. SEM image and micro EDXMA results of a flat spot in the fracture of K76F rail joints at FBW, mode 1

for welded joints of heat-strengthened rails made of eutectoid grade steels [26–30]. The length of such areas on both sides of the JL does not exceed 4 mm, the total width of the HAZ is 24–29 mm, which meets the requirements of [17].

Based on the results of calculations and experimental studies of thermal cycles at FBW, macroanalysis, metallographic examinations, and mechanical tests of welded joints of rails, the general range of changes in Q_{fl} at FBW of heat-strengthened rails of K76F and R350HT grades was determined, which ensures the formation of high-quality joints that meet the requirements of acting regulatory documents for rail welded joints, namely the value of heat input during flashing should be Q_{fl} = 11.88–14.0 MJ. Varying the value of heat input Q_{fl} within certain limits ensures a set cooling rate of welded rail joints in the austenite transformation temperature range and causes the formation of highly dispersed lamellar pearlite without structural components of martensite and bainite.

The determined range of optimal Q_{fl} values was used in developing and optimizing technological modes of FBW of rails of different grades and manufacturers, regardless of the parameters of the power mains and the condition of the rail welding machine. Based on the research results, the FBW technology for heat-strengthened rails was improved [31], a unit of measuring transducers was developed [32], and an algorithm for controlling the FBW process with a regulated cooling mode for welded joints [33] was adapted to the existing programs of the control system of K922-1 and K1000 rail welding machines. Due to the dosed heat input in the flashing process during FBW, the ability to regulate cooling of to rail welded joints was implemented to ensure their compliance with the requirements of acting standards for the indices of hardness and structural state of the joint zone metal (absence of martensite and bainite).

The above procedure of calculation and experimental studies was used to determine the admissible ranges of variation in the technological parameters of the FBW process of railroad frogs. Replacing M76 rails of open-hearth steel with heat-strengthened K76F and R350HT rails of converter steel required improvement of the FBW technology of the frog core of 110G13L steel with rail ends of K76F steel through a transition element (TE) of austenitic chromium-nickel 08Kh18N10T steel. The problems typical of welding dissimilar steels are associated with structural and chemical heterogeneity of the joint zone, the probability of forming a brittle interlayer of variable chemical composition, in particular, areas with a martensitic structure. The problem was solved by applying FBW technology by pulsating flashing, which ensures the

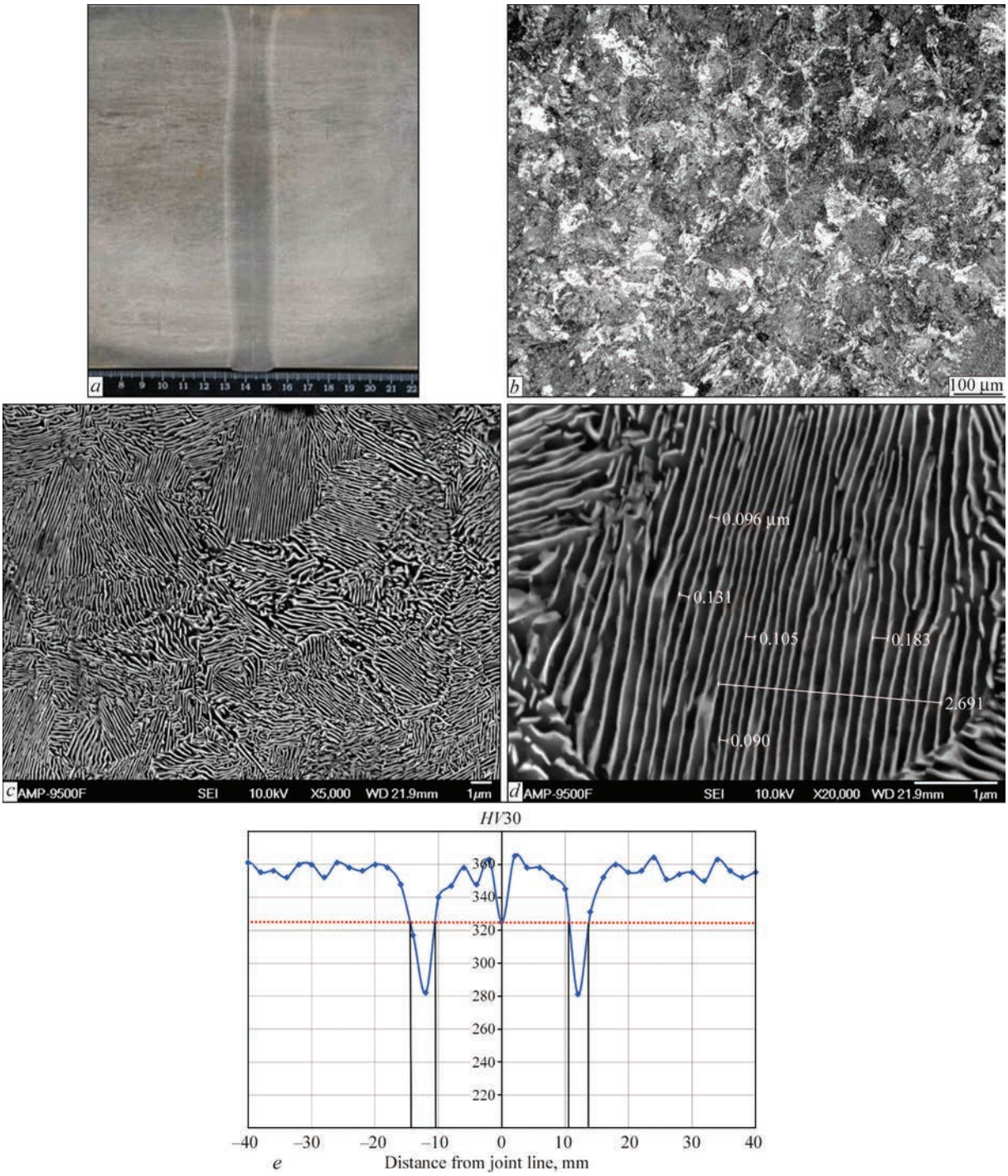

Figure 14. Macrosection (*a*), microstructure ×100 (*b*), SEM images, ×5000 (*c*), ×20000 (*d*) and hardness distribution in the R350HT rail welded joint at FBW (*e*), mode 2

implementation of specified thermal cycles to prevent the formation of brittle structural components in the combined joint of 110G13L, 08Kh18N10T and K76F steels and to produce a regulated pearlite structure in the HAZ of K76F rail steel [32].

Using the algorithm for numerical solution of the three-dimensional thermal conductivity equation under initial and boundary conditions corresponding to the actual welding conditions for the specimens, thermal cycles during FBW of K76F steel with the TE from 08Kh18N10T austenitic steel (joint 1) and 110G13L steel with the TE from 08Kh18N10T steel (joint 2) were obtained. The ranges of variation in the basic technological parameters of the FBW process were determined, at which, in the process of flashing rails of K76F, 110G13L, and 08Kh18N10T steels, their uniform heating along the cross-section and length is ensured, sufficient to perform deformation by a specified value during the upsetting.

The influence of the thermal cycle of FBW of the second joint on the structural stability of the metal in the HAZ of the first joint was evaluated using calcu-

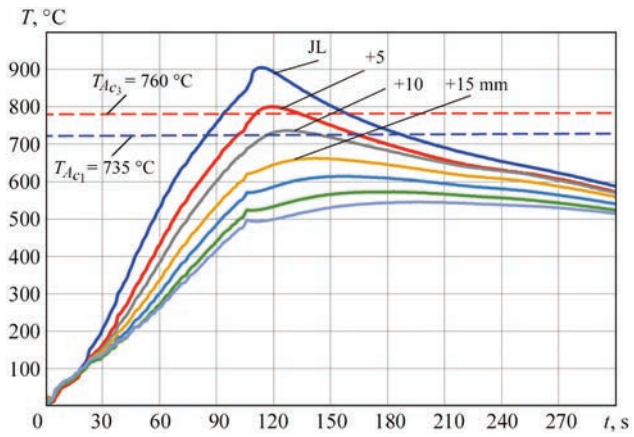

Figure 15. Thermal cycles in the first joint on the side of K76F steel at FBW of the second joint at h_{TE} = 10 mm width (experimental data)

lated and experimental data. It was found that the absence of brittle chromium carbides in the HAZ of both joint of the railroad frog is ensured by implementing the set temperature and time conditions of FBW by pulsating flashing, under which there is no significant diffusion of carbon in the joint zone of K76F and 08Kh18N10T steels, provided that the width of the TE of 08Kh18N10T steel is optimized.

Possible structural changes were evaluated in the metal of the first joint on the side of K76F steel at the TE width of h_{TE} = 10 mm at different distances L from the JL of K76F + 08Kh18N10T steels: L = 0, 5, 10 and 15 mm [33]. In particular, it was found that the thermal cycle of FBW of the second joint at a set value of heat input Q_{fl} can lead to heating of K76F steel in the joint zone of the first butt to a temperature below or above the temperature of structural transformations $T_{A_{c1}}$ = 735 °C, $T_{A_{c3}}$ = 760 °C (Figure 15), depending on the width of the TE of 08Kh18N10T steel.

For a set FBW mode of the second joint, the minimum width of the TE of 08Kh18N10T steel was determined, at which no heating of joint 1 to temperatures $T > T_{A_{c1}}$ occurs and negative structural transformations in joint 1 are excluded. In particular, it was found that for the FBW mode of the second joint with the heat input value Q_{fl} = 14.4 MJ at the TE width $h_{TE} \geq 21$ mm, the first joint is heated to a temperature lower than $T_{A_{c1}}$ = 735 °C, which potentially does not lead to the formation of hardening structures in the joint of K76F+08Kh18N10T steels, and the heating mode corresponds to a short-term "tempering" for K76F steel [33].

Using the improved FBW technology, a pearlite structure of a set dispersion (sorbitic-troostite) is produced in joint 1 on the side of K76F rail steel; welded railroad frogs meet the requirements of acting standards [34].

IMPROVEMENT OF THE QUALITY ASSURANCE SYSTEM FOR FBW OF RAILWAY RAILS

The FBW Department of PWI has developed, put into production, and has been successfully using computerized systems for quality assurance of joints using various pressure welding methods for many years. For FBW of railway rails, a three-level quality assurance system for rail welded joints was developed, which provides for:

- level 1 — development of an effective technology and approval of FBW modes for specific types and grades of railway rails in accordance with the requirements of acting regulatory documents;
- level 2 — in-process control of the basic parameters of the FBW process under actual production conditions, comparison with the established admissible limits of their deviations, issuance of a report (protocols) on the compliance of welded joints with the established requirements;
- level 3 — statistical analysis of rail FBW protocols performed at all FBW machines and submitted to the diagnostic center of the JSC "Ukrainian Railways".

The implementation of level 1 of the quality assurance system is based on the requirements for welded joints of railway rails provided in [11–13, 17]. When developing FBW technology and modes for the existing type and grade of railway rails, as well as a specific rail welding complex, the specialists of the FBW Department use the results of destructive and non-destructive testing, metallographic examinations of rail welded joints produced at PWI testing laboratory certified in accordance with the requirements of DSTU EN ISO/IEC 17025:2019.

In order to implement level 2 of quality assurance, i.e. to ensure stable reproduction of the rail welding process and testing of its basic parameters, a computerized FBW process monitoring and control system was developed, which allows maintaining the optimal flashing mode under actual production conditions largely regardless of operating conditions. The system is based on the use of an industrial computer, controller and appropriate sensors. During welding of each joint, the process parameters can be self-adjusted, which ensures optimization of programs for their variation at all stages of flashing and in general during the welding period. The computerized control system records the basic parameters of the FBW process, determines their admissible deviations from the set values and, in accordance with the established algorithms, assesses the quality of the joints immediately after welding [37].

Statistical analysis of rail welding protocols (level 3) ensures timely detection of systematic deviations of the basic FBW parameters, process optimization and the ability to diagnose the operating rail welding equipment.

The results of calculations are presented in the form of tables, diagrams and histograms and visually represent the progress of the welding process, as well as its dependence on a particular rail welding machine, FBW modes and rail grade. Statistical analysis of rail FBW protocols was successfully implemented in cooperation with the JSC "Ukrainian Railways".

In 2024–2025, remote monitoring for compliance of FBW technology of all welded rail joints with electronic welding reports sent to the Diagnostic Center of the JSC "Ukrainian Railways" from each rail welding machine equipped with a computerized quality control system was established.

PREPARATION OF RECOMMENDATIONS AND AMENDMENTS TO ACTING REGULATORY DOCUMENTS, DEVELOPMENT OF A NEW REVISION OF TECHNICAL SPECIFICATIONS FOR FBW OF RAILWAY RAILS

In 2024, based on the results of research works and contracts, PWI specialists developed recommendations for amending and supplementing the acting technical specifications for welding railway rails [11–13], which were fully taken into account in the new revision of the regulatory documents [36, 37]. An assessment of the results of the joint works is described in a letter from the Director of the CTCR Branch of the JSC "Ukrainian Railways", which states that "as a result of the implementation of the agreements, the technical condition of rail welding machines has been significantly improved to ensure train safety and the sustainable operation of the railway infrastructure under martial law in Ukraine".

UPDATING THE DESIGN OF FBW MACHINES, RENEWAL OF PRODUCTION OF RAIL WELDING COMPLEXES

To meet the needs of the JSC "Ukrainian Railways" and other partners, the problem of renewal of production of rail welding machines developed by PWI is extremely relevant. The successful solution of this problem is inseparably associated with updating the design of mobile and stationary machines for FBW of rails to meet the technical requirements of the customer and the production capabilities of equipment manufacturing companies.

In 2023, the Czech company SaZ s.r.o., in close cooperation with PWI, launched the serial production of double-track WELDERLINER rail welding complexes (Figure 16) equipped with K922-1 mobile machines that implement pulsed FBW technology. This event was preceeded by a significant improvement in the design documentation of the K922-1 machine to meet the manufacturer's technical requirements, design and technological support for the production of rail welding machines, which was carried out by PWI specialists.

The WELDERLINER complexes have successfully passed the comprehensive tests required by the European standard EN 14587-2:2009 for FBW of rails. The K922-1 mobile machine, which is an original development of PWI, is equipped with a modern computerized system for multifactor control of welding parameters, high-speed hydraulic drives, as well as a device for burr removing in the hot state without unclamping the welded rail section to cool the welded joint to a set temperature.

In 2024, PWI developed the design documentation for RW Equipment & Consulting LLC (USA) for the RW1060 mobile rail welding machine, which is an updated version of the K1045 machine for FBW of railway rails in hard-to-reach locations. A batch of K1045 machines was previously produced by the SE "Pressure Welding Engineering Center" (PWEC) of the STC "The E.O. Paton Electric Welding Institute" by order of the Progress Rail Services, USA. The RW1060 machine has an updated design of the current supply circuit, which provides significant advantages in the operation of equipment in subway tunnels, when welding railroad frogs with rails in the railway track. For example, by using unique new design of transformers, including a new approach to the design of current leads, it became possible to reduce the outer width of the opened machine when setting on rails to be welded from 597 mm to 438 mm (in the plane of the head of the rail being welded), which is a critical moment for this type of welding machines. During the production of the RW1060 welding head (Figure 17) at the PWEC, specialists from the Flash Butt Welding Department of PWI provided a design support during the production, and improvements were promptly made to enhance the manufacturability of the machine's components and mechanisms. The main design solutions implemented in the K1045 and RW1060 machines are patented in Ukraine [40–43].

In 2024, PWI launched cooperation with the French Company Yardway Railquip France SAS to provide services on the technology support and maintenance of mobile equipment for FBW of rails. The successful development of cooperation is expected to open up additional opportunities for expanding the use of PWI developments abroad.

In order to renew the production of stationary K1000 rail welding machines to meet the needs of the JSC "Ukrainian Railways", PWI and the Company "Rail Systems" signed a license agreement to grant the right to use the design, manufacturing technology and operation of FBW machines in stationary conditions. In 2024, "Rail Systems" has already gained

Figure 16. Mobile K922-1 machine (*a*), double-track WELDERLINER rail welding complex (*b*, *c*)

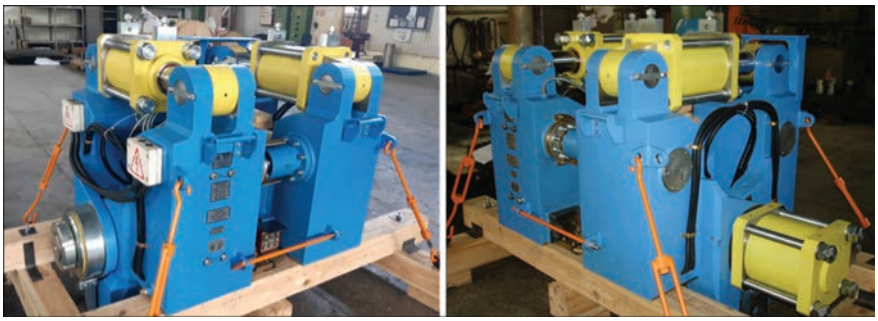

Figure 17. Welding head of the RW1060 machine for FBW of railway rails in hard-to-reach locations

successful experience in overhauling K1000 machines by order of rail welding enterprises of the JSC "Ukrainian Railways".

Long-term cooperation with the Dnieper JSC "Railway Switch Plant" continues to support the technological process of manufacturing railroad frogs, in particular, using the FBW technology for frog cores of high-wear 110G13L steel with rails made of eutectoid grade steel through TE of austenitic chromium-nickel stainless steel. In 2023–2025, PWI successfully performed works on consulting support of the technology for FBW of frogs, audit of the technical condition of the K924M machine, manufacturing of welding circuit elements, development of a set of measures to ensure the specified technical characteristics of the K924M machine and extend its operational life.

Thanks to the joint efforts of the JSC "Ukrainian Railways", PWI and foreign partner companies, critical challenges are being successfully overcome to ensure the operability of the railway infrastructure under martial law in Ukraine and to expand the use of PWI developments abroad.

CONCLUSIONS

1. The critical challenges for ensuring the operability of the railway infrastructure under martial law in Ukraine were analyzed. The suspension of domestic rail production by Azovstal Metallurgical Combine as a result of the occupation has raised the issue of welding used rails and new rails of different grades, from different manufacturers and with various heat treatment modes, in particular a heterogeneous combination. The prob-

lem of extending the service life of existing welding equipment is also relevant.

2. To solve the existing problems, a set of measures was developed to ensure high-quality welding of rails in stationary and field conditions during the repair and construction of continuous welded rails in Ukraine in accordance with the requirements of regulatory documents.

3. Implementation of the developed set of measures in 2022–2025 allowed solving a number of problems related to the FBW of railway rails:

- the causes for non-compliance of some rail welded joints of different grades with the requirements of regulatory documents were identified, recommendations were developed to prevent defects and reliably detect probable defects during non-destructive testing of rail welded joints;
- an audit of the technical condition of rail welding equipment available at the JSC "Ukrainian Railways" was conducted and measures were developed to extend its operational life;
- the technology was improved and the process modes of FBW of heat-strengthened railway rails of converter production were optimized;
- quality assurance systems for joints during FBW of railway rails were optimized;
- designs of mobile rail welding machines were updated, production of equipment for FBW of rails was renewed.

4. Thanks to the joint efforts of PWI of the NAS of Ukraine, structural units of the JSC "Ukrainian Railways", domestic and foreign partner companies, critical challenges are being successfully overcome to ensure the operability of the railway infrastructure under martial law in Ukraine and expand the use of domestic developments abroad.

REFERENCES

1. Paton, B.E., Kostyuk, M.D., Kuchuk-Yatsenko, S.I. et al. (2010) Innovative cluster "Velvet Way" and scientific and technical breakthrough of Ukraine on the world market of construction of high-speed railways. *Nauka ta Innovatsii*, 6(**2**), 69–86 [in Russian].
2. Solano-Alvarez, W., Bhadeshia, H.K.D.H. (2024) Steels for rails. *Progress in Materials Sci*., 146, **December**. DOI: https://doi.org/10.1016/j.pmatsci.2024.101313
3. Ziakhor, I.V., Antipin, E.V., Didkovsky, O.V. et al. (2023) Modern technologies of welding railway rails (Review). *The Paton Welding J*., **8**, 4–16. DOI: https://doi.org/10.37434/tpwj2023.08.01
4. Kuchuk-Yatsenko, S.I. (2018) Technologies and equipment for flash-butt welding of rails: 60 years of continuous innovations. *The Paton Welding J*., **11–12**, 25–40. DOI: https://doi.org/10.15407/tpwj2018.12.03
5. Kuchuk-Yatsenko, S.I. (2019) 60 years of the first in the world mobile machine for flash-butt welding of rails in the field conditions. *The Paton Welding J*., **3**, 2–5. DOI: https://doi.org/10.15407/tpwj2019.03
6. Kuchuk-Yatsenko, S.I., Didkovsky, A.V., Shvets, V.I. et al. (2016) Flash-butt welding of high-strength rails of nowadays production. *The Paton Welding J*., **5–6**, 4–12. DOI: https://doi.org/10.15407/tpwj2016.06.01
7. Rudenko, P.M., Gavrish, V.S., Kuchuk-Yatsenko, S.I. et al. (2017) Influence of flash-butt welding process parameters on strength characteristics of railway rail butts. *The Paton Welding J*., **5–6**, 75–78. DOI: https://doi.org/10.15407/tpwj2017.06.14
8. Kuchuk-Yatsenko, S.I., Milenin, A.S., Velikoivanenko, E.A. et al. (2018) Mathematical modeling of metal heating process in continuous flash-butt welding. *The Paton Welding J*., **10**, 2–8. DOI: https://doi.org/10.15407/tpwj2018.10.01
9. Kuchuk-Yatsenko, S.I., Rudenko, P.M., Gavrish, V.S. (2016) Statistical control of process of flash-butt welding of rails. Two-level control system. *The Paton Welding J*., **5–6**, 13–16. DOI: https://doi.org/10.15407/tpwj2016.06.02
10. Kuchuk-Yatsenko, S.I., Rudenko, P.M., Gavrish, V.S. et al. (2019) System of controlling the process of flash-butt welding of rails under stationary and field conditions to extend the service life and reliability of railway tracks. *Tekh. Diagnost. i Nerazrush. Kontrol,* **2**, 41–50. DOI: http://dx.doi.org/10.15407/tdnk2019.02.07
11. TU UZ 24.1-40075815-085:2019: *Ordinary used rails. Repair and welding. Specifications.*
12. TU UZ 24.1-40075815-109:2020: *Railway rails. Welding of rail butt joints by contact method at enterprises and on the track. Specifications.*
13. TU UZ 24.1-40075815-002:2021: *New welded rails for railways. Specifications.*
14. DSTU 4344:2004: *Ordinary rails for broad gauge railways. General technical requirements.* Ukrainian Research Institute of Metals UkrNDIMet. Kyiv, Derzhspozhyvstandart Ukrainy.
15. DSTU EN 13674-1:2018 (EN 13674-1-2011:2005, IDT): *Railway transport – Track – Rails*. Pt 1: Railway rails Vignole 46 kg/m and above. Kyiv, SE UkrNDNTs.
16. BS EN 13674-1:2011+A1:2017: *Railway applications – Track – Rail*. Pt 1: Vignole railway rails 46 kg/m and above. European Committee for Standardization.
17. DSTU EN 14587-2:2015 (EN 14587-2:2009, IDT): *Railway transport. Track. Butt welding of rails.* Pt 2. New rail classes R220, R260, R260Mn and R350HT with a mobile welding mechanism compared to a stationary mechanism. Kyiv, SE UkrNDNTs.
18. Zadorozhnyuk, O.M., Kapitanchuk, L.M., Smiyan, O.D., Butkova, E.I. (2013) New possibilities to carry out metals science investigations of base metal and welded joints. *Sovrem. Elektrometall.,* **2**, 36–40. DOI: https://patonpublishinghouse.com/rus/journals/sem/2013/02/08
19. Rybkin, V.V. et al. (2013) *Classification and catalog of defects and damage of rails in railways of Ukraine.* TsP-0285. Kyiv, Inpres.
20. (1998) DSTU 3715–1998: *Metals. Types of fracture surfaces (ruptures).* Institute of Casting Problems of the NASU. Kyiv, Derzhstandart Ukrainy.
21. DSTU EN ISO 6520:2015 (EN ISO 6520-1:2007, IDT; ISO 6520-1:2007, IDT) *Welding and allied processes. Classification of geometric imperfections in metallic materials*. Pt 2. Pressure welding.
22. DSTU 7175:2010: *Metals and alloys. Methods of metallographic testing. Terms and definitions of concepts*. Kyiv, Derzhspozhyvstandart Ukrainy.
23. Shvets, V.I., Ziakhor, I.V., Kapitanchuk, L.M. (2023) Features of formation and transformation of oxides in flash-butt welding of K76F rails. *The Paton Welding J*., **7**, 16–24. DOI: https://doi.org/10.37434/tpwj2023.07

24. Babachenko, O., Kononenko, G., Khulin, A. (2018) Investigation of austenite decomposition kinetics in continuous cooling of K76F steel for ordinary rails of broad gauge railways. Fundamental and Applied Problem of Ferrous Metallurgy. *Sbornik IChM*, **32**, 317–327.
25. Kuchuk-Yatsenko, S.I., Shvets, V.I., Didkovsky, A.V. et. al. (2013) Defects of joints of high-strength rails produced using flash-butt welding. *The Paton Welding J*., **9**, 2–8.
26. Mousavizade, M., Farhangi, H. (2010) Characterization of surface defects associated with flash-butt welded pearlitic rails and their contribution to overload and fatigue failures. *Adv. Materials Research*, **83–86**, 1262–1269. DOI: http://dx.doi.org/10.4028/www.scientific.net/AMR.83-86.1262
27. Porcaro, R.R., Faria, G.L., Godefroid, L.B. et al. (2019) Microstructure and mechanical properties of a flash butt welded pearlitic rail. *J. Mater. Process. Tech*., **270**, 20–27. DOI: http://dx.doi.org/10.1016/j.jmatprotec.2019.02.013
28. Micenko, P., Muruganant, M., Huijun, Li, Xu Xiaofeng (2013) *Double dip hardness profiles in rail weld heat-affected zone — Literature and research review report*. CRC Project Report, R3.121, Brisbane, Australia.
29. Weingrill, L., Krutzler, J., Enzinger, N. (2016) Temperature field evolution during flash-butt welding of railway rails. *Mater. Sci. Forum*, **879**, 2088–2093. DOI: https://doi:10.4028/www.scientific.net/MSF.879.2088
30. Micheletto, A., Cookson, J., Pang, Y. et al. (2020) The structural integrity of flash-butt welded premium rail steel — Evaluation of strength, microstructure and defects. Proc. of the Institution of Mechanical Engineers. Pt F. *J. of Rail and Rapid Transit,* 235(**8**), 1006–1012. DOI: https://doi.org/10.1177/0954409720973138
31. Antipin, Ie., Ziakhor, I., Didkovsky, O. et al. (2023) Technology of flash butt welding of heat-strengthened rails. In: *Abstr. of Papers of 13th Inter. Sci.-Pract. Conf. on Complex Assurance of Quality of Technological Processes and Systems. 25–26 May 2023, Chernihiv, Ukraine,* Vol. 2, 91–92 http://ir.stu.cn.ua/123456789/28253
32. Kavunichenko, O.V., Ziakhor, I.V., Shylo, Yu.A. et al. (2024) Thermal cycles and microstructure of the flash butt welded joints of 110G13L and K76F steel rails through 08Xh18N10T steel insert. *The Paton Welding J.*, **3**, 9–14. DOI: https://doi.org/10.37434/tpwj2024.03.02
33. Shylo, Yu.A., Ziakhor, I.V., Kavunichenko, O.V. et al. (2025) Thermal cycles in contact flash butt welding of railway frogs. In: *Abstr. of Papers of 13th Inter. Sci.-Pract. Conf. on Complex Assurance of Quality of Technological Process and Systems. 22–23 May 2025, Chernihiv, Ukraine,* Vol. 2, 89 https://drive.google.com/file/d/1LZk8Efz_0OsYSOPtmLeR8y3PuVnIJeys/view
34. EN 14587-3:2012: *Railway applications – Track – Rail.* Pt 3: Welding in association with crossing construction. European Committee for Standardization.
35. Kuchuk-Yatsenko, S., Rudenko, P., Gavrish, V. et al. (2020) Operational control as a means of the evaluation of quality of welded connections for flash-butt welding of modern high-strength steels, *Nauka ta Innovatsii,* **16**, 72–78. DOI: http://dx.doi.org/10.15407/scin16.02.072
36. TU UZ 24.1-40075815-002:2024: *New welded rails for railways. Technical conditions.* Branch of NDKTI of Railway Transport, JSC Ukrzaliznytsia. Effective date 10.05.2025.
37. TU UZ 24.1-40075815-139:2025: *Old rails. Repair and welding of butt joints in the track and outside the track. Technical conditions*. Branch of NDKTI of Railway Transport, JSC Ukrzaliznytsia. Effective date 10.05.2025.
38. Ziakhor, I.V., Koval, M.Y., Didkovsky, O.V. et al. (2022) *Machine for resistance butt welding of rails.* Pat. of Ukraine on utility model, 151797, Publ. 14.09.2022. https://sis.nipo.gov.ua/uk/search/detail/1705612/
39. Ziakhor, I.V., Koval, M.Y., Didkovsky, O.V. et al. (2022) *Machine for resistance butt welding of rails.* Pat. of Ukraine on invention, 128177, Publ. 24.04.2024. https://sis.nipo.gov.ua/uk/search/detail//1796632/
40. Ziakhor, I.V., Koval, M.Y., Didkovsky, O.V. et al. (2024) *Machine for resistance butt welding of rails.* Pat. of Ukraine on utility model, 156326, Publ. 05.06.2024. https://sis.nipo.gov.ua/uk/search/detail/1803859/
41. Ziakhor, I.V., Koval, M.Y., Didkovsky, O.V. et al. (2024) *Machine for resistance butt welding of rails.* Pat. of Ukraine on utility model, 157480, Publ. 23.10.2024 https://sis.nipo.gov.ua/uk/search/detail/1824287/

ORCID
I.V. Ziakhor: 0000-0001-7780-0688,
Ye.V. Antipin: 0000-0003-3297-5382,
O.V. Didkovskyi: 0000-0001-5268-5599,
A.M. Levchuk: 0000-0002-0361-7394,
P.M. Rudenko: 0000-0002-7770-2145,
Yu.A. Shylo: 0000-0002-6174-5925

CONFLICT OF INTEREST
The Authors declare no conflict of interest

CORRESPONDING AUTHOR
I.V. Ziakhor
E.O. Paton Electric Welding Institute of the NASU
11 Kazymyr Malevych Str., 03150, Kyiv, Ukraine.
E-mail: zyakhor2@ukr.net

SUGGESTED CITATION
I.V. Ziakhor, Ye.V. Antipin, O.V. Didkovskyi, A.M. Levchuk, V.V. Kalyuzhny, V.V. Ozyumenko, P.M. Rudenko, Yu.A. Shylo (2025) Urgent problems of welding railway rails under martial law in Ukraine. *The Paton Welding J*., **8**, 3–18. DOI: https://doi.org/10.37434/tpwj2025.08.01

JOURNAL HOME PAGE
https://patonpublishinghouse.com/eng/journals/tpwj

Received: 16.05.2025
Received in revised form: 25.06.2025
Accepted: 30.07.2025

DOI: https://doi.org/10.37434/tpwj2025.08.02

MIAB WELDING TECHNOLOGY OF PIPES AND PARTS OF AUTOMOTIVE INDUSTRY

V. Kachynskyi[1], **D. Allford**[2], **V. Klymenko**[1]

[1]E.O. Paton Electric Welding Institute of the NASU
11 Kazymyr Malevych Str., 03150, Kyiv, Ukraine
[2]Arc Specialties, USA
1730 Stebbins Drive, Houston, TX 77043-2807, USA

ABSTRACT

The purpose of the research presented in this article is to develop a technology for press magnetically impelled arc butt welding (MIAB welding) using a pulsed increase in welding current and controlled precision allowance of the upset during the formation of joints of pipe steels and parts of the automotive industry. The main attention is paid to reducing energy consumption while ensuring high-quality welded joints. During welding, operational control of the main technological parameters was carried out: welding current, voltage, displacement and force at the moment of upset. To study the processes occurring in the arc gap between the ends of the pipes, high-speed video recording with a resolution of up to 4500 frames/s, as well as oscillography of the welding cycle parameters, was used. The resulting welded joints were tested in accordance with the requirements of international standards for gas and oil pipelines (API, DNV), which allowed assessinging their mechanical characteristics, reliability, and compliance with industrial application requirements.

KEYWORDS: technology of magnetically impelled arc butt welding, radial component induction of the control magnetic field, pulsed welding current, controlled upset allowance, formation of pipe joints

INTRODUCTION

MIAB welding is an innovative process that combines the advantages of heat treatment and mechanical butt welding of steel pipes and tubular parts. Process has found application in various industries due to its high productivity, stability of the quality of welded joints, as well as a high level of mechanization and automation of the technological process. The peculiarity of the automatic mode of MIAB welding is to significantly reduce the influence of the human factor on the quality of joints, which makes it especially effective for the manufacture of structures of critical purpose.

During the research, it was found that the influence of thermal and deformation cycles with the use of pulsed increase in welding current before the upset and the implementation of a controlled upset allowance contributes to the formation of joints with optimal characteristics according to the technical requirements of enterprises.

INDUSTRIAL APPLICATION

The main advantages of the MIAB welding process include high productivity due to the potentially high level of automation, as well as a reduction in the cost of manufacturing welded pipe joints. This process is particularly promising for use in the automotive industry, power plants, boiler production, pipelines for various purposes, oil refining and petrochemical plants, ships and other industries where liquids and gases are transported under high pressure and temperature, and where increased requirements are placed on the reliability and accuracy of welded joints.

Due to the short welding cycle and high reproducibility of the quality of joints, process is an effective solution for mass industrial production. The results of scientific research in the field of MIAB welding have been successfully implemented in practice. In particular, the results of a number of studies have been applied during the construction of pipelines, which confirmed the feasibility and effectiveness of implementing this process in industrial conditions [1–13]. MIAB welding technology and equipments developed at the E.O. Paton Welding Institute (PWI) have found practical use in welding pipelines with a diameter of up to 100 mm.

The MIAB welding is used in the automotive industry to join the drive shafts, cardan shafts, air springs, shock absorber assemblies and brake pipes. Industrial use in the automotive industry has been achieved by the development of technology and industrial equipment for Magnetarc welding by KUKA, Germany and for MIAB welding by PWI, Ukraine [14–16].

RESEARCH PROGRESS

For a comprehensive study of welding in a wide range of standard sizes of steel pipes and tubular parts with a diameter of Ø20–300 mm, K872, MD-205 and MD101 machines were used. Steel grades and their mechanical properties are given in Tables 2 and 4. Welding was performed in machines developed at the PWI. The experimental K-872 machine is shown in Figure 1.

The main technical characteristics of the pilot machines are presented in Table 1.

The K872 and MD205 installations include (Figure 2, *a*): welding machine (*1*), protection (*2*), pumping station (*3*), hydraulic system (*4*), computerized control system (*5*), welding current source (*6*), control panel (*7*), hydraulic hoses (*8*), electric cables (*9*). Figure 2, *b* shows the MD205 industrial installation for welding tubular parts of hydraulic cylinder bodies.

The design of the modernized MD101 machine with a developed hydraulic drive for welding pipes with a diameter of up to Ø60 mm is presented in Figure 3.

To carry out the work, the equipment was modernized in the following areas:

1. The hydraulic systems of the machines were improved with the possibility of a controlled upset with a given allowance.

2. A system for pulsed increase of the welding current before upset was developed.

3. The control program and the system for recording technological parameters of welding were improved to perform the above developments.

The block diagrams of the welding machine after modernization are shown in Figure 4.

To ensure the implementation of the quality control algorithm, the control system was modernized on the basis of an industrial computer. 3 Lincoln Linc 635SA welding rectifiers connected in parallel were used to power the arc. Supercapacitors were also used to create a pulsed increase in current [17].

FUNCTIONING OF THE CONTROL PROGRAM AND RECORDING OF TECHNOLOGICAL WELDING PARAMETERS

Preparation of the machine actuators for the welding process is carried out in the following sequence:

- turning on the control cabinet, starting the control program and recording parameters;
- turning on the pumping station and power source;
- installing pipes in the welding position.

After checking the compliance of the equipment state with the initial conditions for starting the process, the message "System ready" appears in the main window of the control program, indicating the readiness of the hardware for welding.

After pressing the "Welding" button, all remote controls are blocked, except for the "Stop welding" and "Emergency stop" buttons. The pipe welding process occurs automatically without the use of shielding gases.

A welding quality control algorithm has been developed based on the analysis of process parameters, covering three key stages:

1. Heating — the period of formation of the temperature field at the ends of the pipes being welded;

2. Welding current pulse — ensuring a protective environment in the arc gap due to intensive surface renewal;

3. Controlled upset — formation of a joint in the solid phase.

The conclusion about the quality of the produced welded joint with a certain degree of probability is made on the basis of logical rules formed based on the results of research into the technological features of the MIAB welding process.

The developed system for controlling and recording technological parameters of the welding process significantly expands the capabilities of personnel during the operation of welding equipment. It allows changing the settings and algorithms of the equipment's operation without significant resource costs. In addition, the system provides remote monitoring of welding operations at remote sites, as well as quality control without the need for direct intervention in the production process [18].

The program window displays the technological parameters of the welding machine, which are controlled by the system.

It is possible to automatically switch to another welding mode in case of a change in the pipe diameter. During each start of the welding cycle, the system automatically performs the following actions:

- creates a technological process data file;
- forms a welding progress diagram;
- makes appropriate changes to the report file.

These operations are performed regardless of the progress of the welding process and are completed after its completion. Documentation of welding parameters is carried out in automatic mode, which allows:

- assessing the level of deviation of technological parameters from the specified values;
- correcting the parameters if necessary.

STUDYING THE INFLUENCE OF THE MAIN TECHNOLOGICAL PARAMETERS ON THE NATURE OF THE MIAB WELDING PROCESS

Studies of the processes occurring in the arc gap during heating of the pipe ends by an electric arc mov-

Table 1. Basic technical characteristics of machines power consumption, kVA

Machine type	Pipe diameter, mm	Wall thickness, mm	Productivity, joints/h	Upset force, kN	Power consumption, kVA	Weight, kg
MD101	10–61	1–5	120	40	30	230
K872	32–220	3–10	60	280	150	2700
MD205	32–240	3–11	60	350	170	2300

ing at high speed (up to V_a = 130 m/s) were carried out on tubular parts with a diameter of up to Ø200 mm and a wall thickness of up to δ = 10 mm. High-speed video recording was used to monitor the process.

The main parameters of the process — magnetic field induction, welding current and arc voltage — varied within the limits characteristic of the modes adopted for process when welding pipes of the specified type. At the same time, computer record of the specified parameters was carried out.

The studies carried out within the framework of this work were aimed at developing a technology for butt-joining of steel pipes adapted for operation in both field and stationary conditions. Welding was carried out on samples of various steel grades, in particular: X60, X70, X80, St35, 09G2S, JIS STPG410, ASTM A615 Grade 520. The chemical composition of the steels is given in Table 2.

Uniform heating of the surfaces of the pipes being welded is determined by the stability of the arc movement under the influence of an external control magnetic field (CMF). The speed of the arc movement depends on the following factors:

- the magnitude of the welding current;
- CMF induction;
- the gap between the pipe ends;

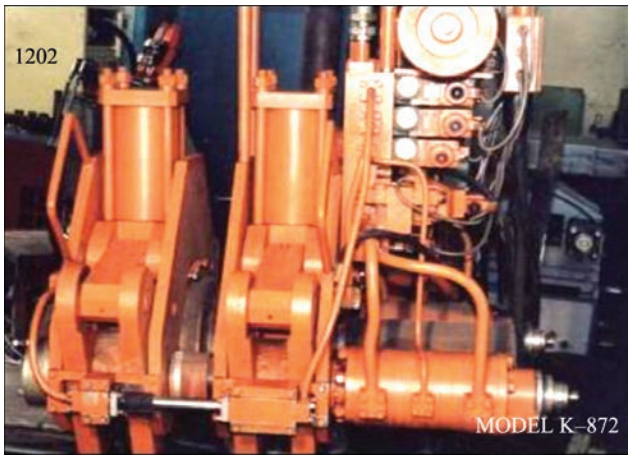

Figure 1. Machine K-872 for experimental studies

- the quality of edge preparation.

The position of the arc at the ends of the welded parts is determined both by the distribution of the control magnetic field induction and the influence of the ferromagnetic masses of the steel pipes on the arc. The results of the studies have shown that when welding steel products, the electric arc after excitation at the outer edges, under the influence of the ferromagnetic masses of the parts and the radial component of the CMF induction, is shifted in the arc gap to the inner region of the ends, Figure 5.

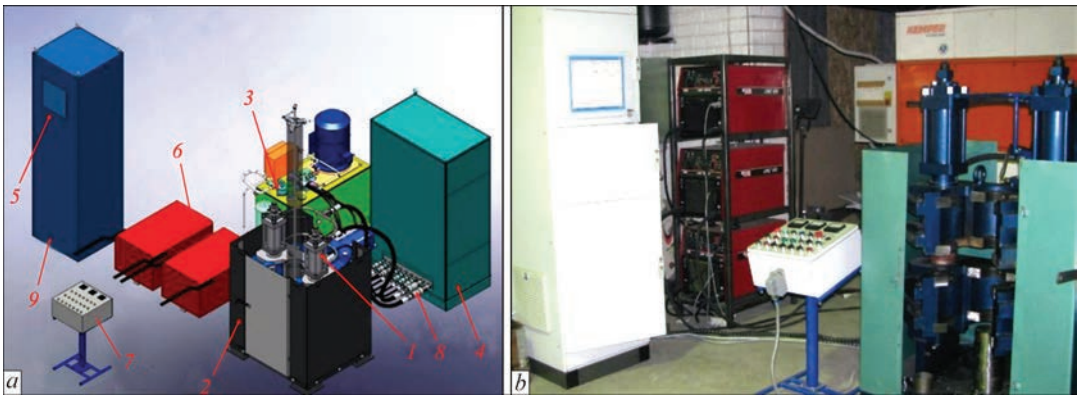

Figure 2. MD205 pipe welding machine, where: *a* — equipment for MIAB; *b* — MD205 machine in production

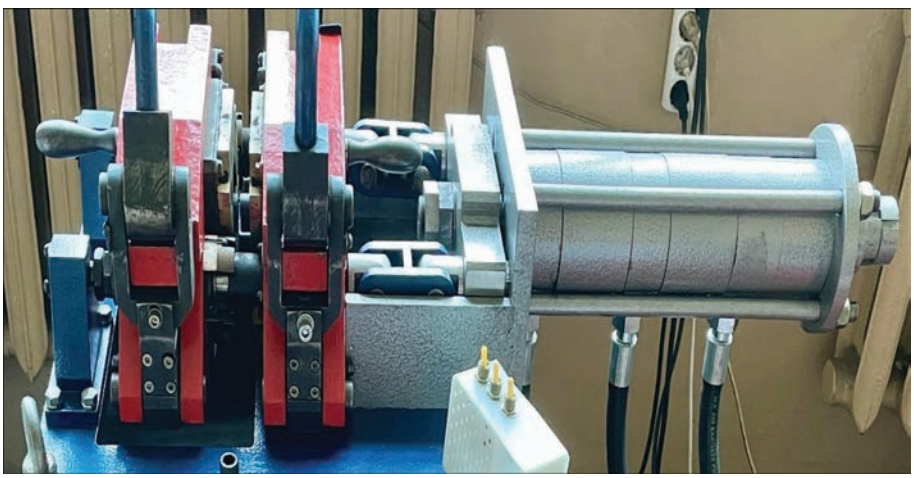

Figure 3. Machine MD-101

Table 2. Chemical composition of steels, %

Type steel	09G2S	St35	API X70	DIN 17100 St52-3	ASTM A615 Grade 520	JIS STPG410	ASTM A106/API5L
C	0.11	0.39	0.030	0.18	0.159	0.25	0.28
Si	0.75	0.35	0.156	0.52	0.172	0.34	0.25
Mn	1.38	0.75	1.45	1.35	1.19	0.9	1.20
P	0.015	0.035	0.004	0.02	0.012	0.024	0.030
S	0.016	0.04	0.004	0.03	0.006	0.033	0.030
Cu	0.05	0.25	0.30	0.28	0.13	-	0.50
Ni	0.05	0.25	0.14	0.24	0.04	0.001	0.50
Cr	0.25	0.25	0.14	0.24	0.04	0.001	0.50
Mo	0.05	–	0.20	–	0.002	–	0.15
Ti	–	–	0.022	–	0.002	–	–
Nb	–	–	0.062	–	0.002	–	–
Al	0.01	–	–	–	0.03	–	–

It was established that the optimal gap for welding pipes with a diameter of Ø150 mm is δ = 1.9±0.2 mm. The results of the studies showed that when the CMF induction is less than B_r = 70 mT, the arc movement is unstable. An insufficient level of induction leads to oscillations of the arc column, especially when the pipes are horizontally placed, which causes local overheating and the formation of molten metal in the lower part of the welding zone. As a result, a crater is formed in the gap between the pipe ends (Figure 6).

Stable arc movement along the pipe ends is achieved when the radial component of the CMP induction is within B_r = 110–180 mT (Figure 7, *a*).

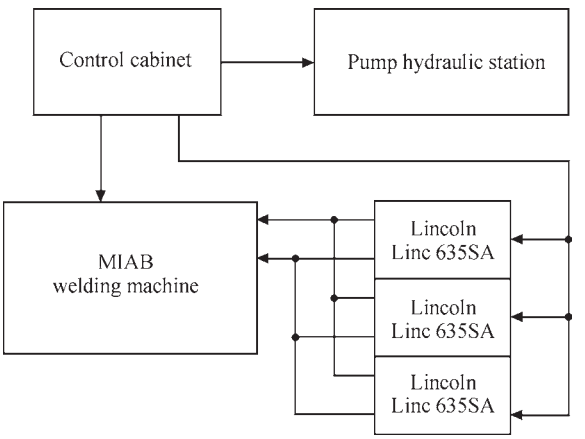

Figure 4. Block diagram of the welding machine

Figure 5. Displacement of the arc to the inner area of the butts

Under such conditions, relatively uniform heating of the ends is ensured, which is a necessary condition for plastic deformation of the material during upset (Figure 7, *b*).

The heating time with other parameters remaining constant is in a narrow range. Its value depends on the current and arc voltage, and a change in one of these parameters affects the change in the other. Excessive heating of the pipe ends can lead to the formation of liquid bridges between the pipes, which disrupts the stable movement of the arc in the gap.

The size of the arc gap largely determines the quality of welded joints. This parameter depends on the requirements for the stability of arc excitation and its stable movement. In the studied range of pipes, the value of the arc gap, as experiments have shown, varies within δ = 1.7–2.1 mm. Figure 8, *a–f* shows photographs illustrating the behavior of the arc in the gap during heating of the ends at different stages of pipe welding.

The welding arc current was I_a = 200–250 A, the arc voltage $U_2 = 25^{\pm 2}$ V. After the arc is excited between the ends, the speed of its movement during heating constantly increases, from V_a = 50 m/s reaching V_a = 240 m/s depending on the diameter of the

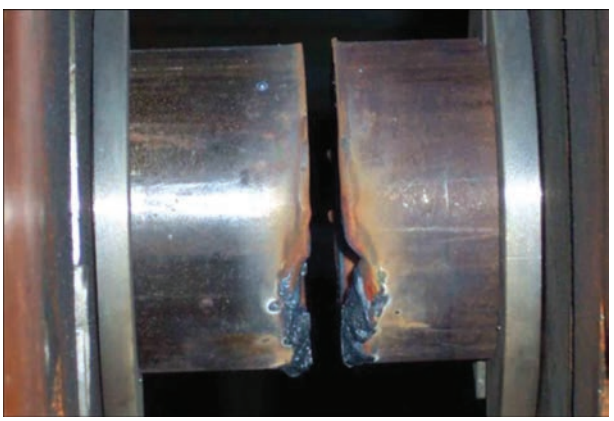

Figure 6. Molten metal crater

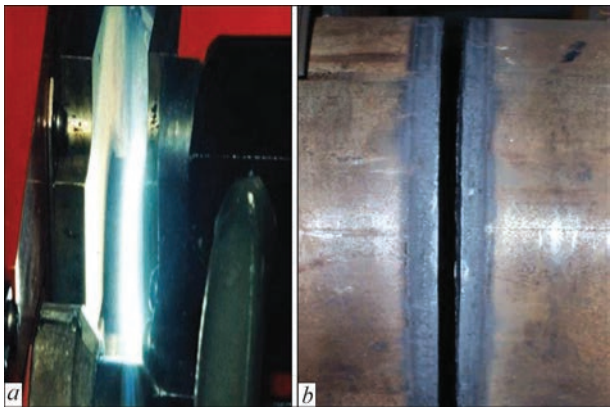

Figure 7. Pipe welding process, where: *a* — MIAB welding; *b* — pipe butts after heating

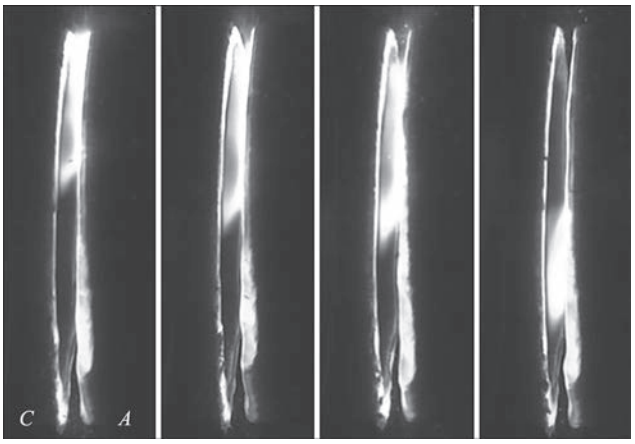

Figure 9. Movement of the cathodic and anodic plasma flow of the arc column

pipes (Figure 8, *a*). As the temperature of the ends increases, the thickness of the melt increases (Figure 8, *b*), which is held on the surface of the ends by surface tension forces. When a certain thickness is reached, the melt, under the influence of forces, rotates the arc along the heated ends (Figure 8, *c*), and begins to move in the same direction. The regulated speed of this movement under certain conditions can reach V_m = 3 m/s. The movement of the melt is due to the action of electrodynamic forces and the gas pressure in the arc gap formed by the arc column. This movement contributes to the stirring of the molten metal layer. Before upseting, the melt layer is evenly distributed along the perimeter of the pipe and the thickness of its butts (Figure 8, *d*).

In the initial period of upset, the gap between the butts decreases, and the arc discharge stops at the time of closing the gap (Figure 8, *e*), a continuous layer of molten metal begins to form between the butts (Figure 8, *f*), which, under the action of the magnetic field (current supply through the ends does not stop), continues to move in circular trajectories. This contributes to the renewal of the melt and the formation of a continuous layer over the entire cross-section of the pipes being welded. At the moment of closing the gap, the melt is squeezed out of the joint, and deformation of the heated metal layers in the solid state occurs [19].

The magnitude and direction of the CMF induction have a great influence on the nature of the shift of the active spots of the welding arc. It was found that in the process of welding under the action of an external magnetic field, the arc speed during heating reaches V_a = 120–140 m/s depending on the diameter of the pipes, while initially the cathode plasma flow of the arc column is displaced relative to the anode (Figure 9). Having reached the anode, the cathode plasma flow of the arc forms a new anode spot. A movement of both the anode and cathode active spots of the arc is observed.

In order to study the nature of changes in the linear velocity of the arc, a series of experiments were conducted on welding pipes Ø121×8 mm, during which

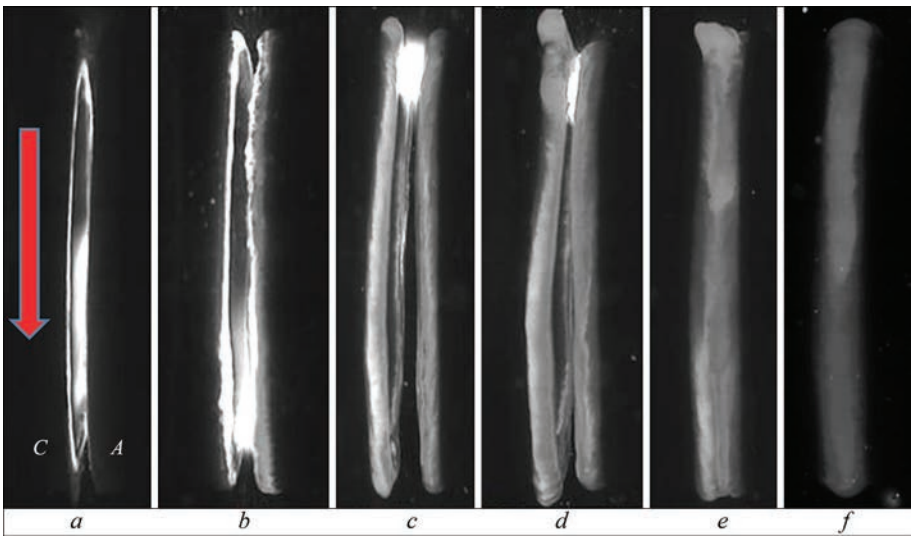

Figure 8. Stages of pipe welding, where: *a* — the beginning of arc movement under the action of the CMF; *b* — the formation of a layer of melt on the ends of the pipes; *c* — the movement of the melt during the heating process; *d* — the renewal of the melt before upset; *e* — the beginning of upset; *f* — the formation of a welded joint

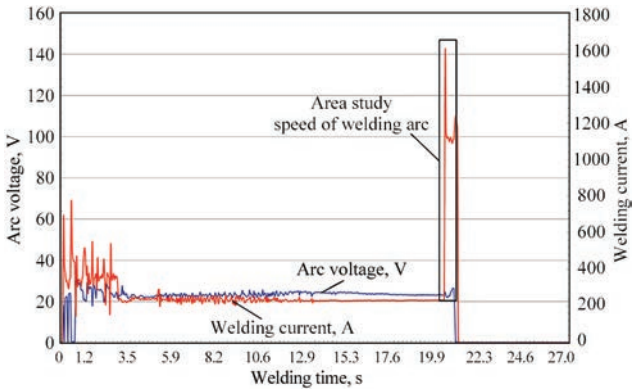

Figure 10. Main parameters of the pipe welding process

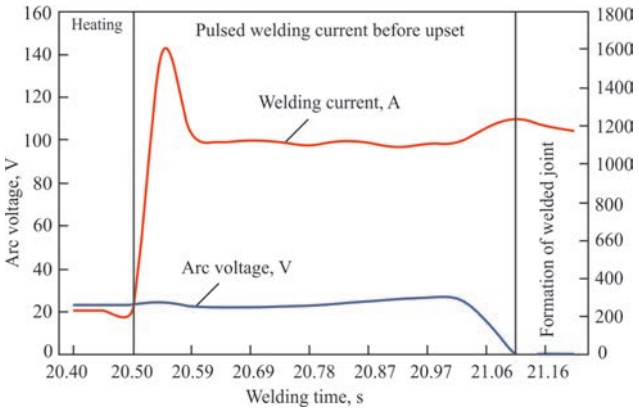

Figure 11. Welding arc current pulse before pipe upset

the technological parameters of the process were varied. In particular, the pulse of the welding current before the upset stage was varied within wide limits. Figure 10 shows a graphic record of changes in the main heating parameters. The rectangle on the graph highlights a section covering the period from the moment of the start of the pulsed increase in the welding current to the start of the upset under current. This section is presented in more detail in Figure 11, which made it possible to analyze the shape of the pulse and the nature of changes in the welding current both before the upset and directly during its execution.

When the welding arc current increases, the arc travel speed sharply accelerates (up to 240 m/s), which leads to intensive renewal of the welding surfaces and creates a protective environment. Experiments have shown that the magnitude of the pulse current before the upset should be higher than the heating current. A relatively uniform layer of liquid metal with a thickness of up to $\delta_{lm} = 0.5$ mm remains on the melted ends, which contributes to the formation of welded joints. The optimal pulse current has been established for each pipe size up to Ø200 mm. Changes in the pulse current by ±5 % from the optimal do not significantly affect the quality of the joints. The duration of the current pulse is within $t = 0.2$–0.6 s. At smaller ($t < 0.2$ s) values of the current pulse duration, the moving arc does not have time to completely renew the layer of molten metal saturated with gases from the end surfaces. In this case, the quality of the welded joints is low. Maintaining an increased current value for more than $t = 0.7$ s leads to increased consumption of heated metal of the pipe ends and a decrease in the quality of the welded joint. The upset is determined by the speed of closing the arc gap between the welded pipe ends and the formation of the welded joint. This ensuring conditions under which the liquid metal layer is preserved on the ends and controlled deformation of the HAZ occurs according to the specified allowance. The time of crystallization of the metal layer on the ends depends on many factors that accompany cooling. For pipes it ranges within $t = 0.01$–0.025 s. Interruptions of the current at the final stages of the heating process before upset lead to oxidation of the ends and crystallization of the liquid layer on the pipe ends.

It was experimentally determined that at upset rates less than $V_{upset} = 40$ mm/s, oxides are observed in weld-

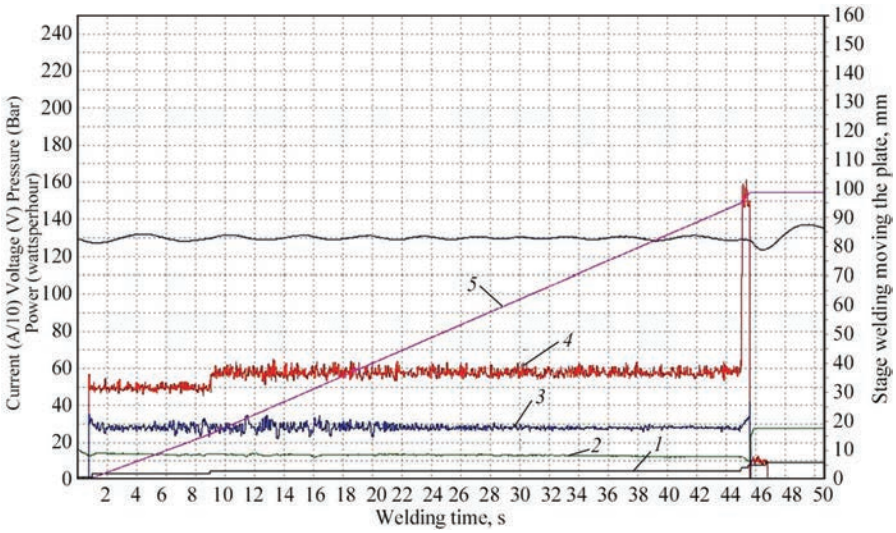

Figure 12. Diagram of the pipe welding process, where: *1* — position of the moving part of the machine; *2* — area of controlled upset; *3* — arc voltage; *4* — welding current; *5* — energy accumulated during the pipe heating process

ed joints, which significantly reduces the ductility of the joints and the strength properties of the joints.

The given scope of work allowed drawing the following conclusions:

Maintaining the setting and electrical parameters of welding within the permissible values leads to producing high-quality welded joints.

Defects along the joint line (oxides and matte spots) up to 2 mm^2 in size belong to defects of the base metal that fall into the joint. As tests have shown, these defects do not affect the qualing of welded joints.

MIAB WELDING TECHNOLOGY WITH PULSED HEATING AND CONTROLLED UPSET FOR FORMING WELDED PIPES JOINT

In the process of welding pipes, for example Ø140×8 mm, the system allows you to get a graphical representation of the process, which makes it possible to visually assessing the progress of the welding process, Figure 12. The welding current can be divided into three stages, and the welding time — into four stages. For welding pipes, the current I1 is used for approximately t_1 = 0.5 s, during which the welding pipes are briefly compressed to a short circuit and the welding rectifier is turned on. t_2 is the time period during which the short-circuited pipe ends are taken to the arc gap, after which an arc is excited between them. At the time stage t_2, the arc begins to rotate in the gap and heat the pipe ends, the arc current I_2 = 490–510 A. At the time stage t_3, the welding current increases to I_3 = 580–600 A, heating of the pipe ends the continues. At time stage t_4, the arc current pulse-like increases to I_4 = 1500 A, the arc accelerates and rotates at a relatively high speed, renewing the surfaces of the heated pipe ends. The welding cycle is completed with a controlled upset with an allowance S = 6.2 mm. The total time of welding of pipes Ø140×8 mm is t = 46 s.

The formation of welded pipe joints in MIAB welding, as in other press butt welding methods, occurs as a result of the joint deformation of the end surfaces of the pipes heated to a ductile state. Uniform heating of the ends is a necessary, but not sufficient condition for the formation of a high-quality joint. One of the key parameters affecting the quality of the joint is the arc rotation speed and the duration of heating. Too low rotation speed leads to an uneven thermal field, the formation of local zones of overheating or, conversely, underheating, which negatively affects the structure of the weld. Optimization of this parameter allows ensuring the stability of the process, uniform temperature distribution along the welding zone and reducing the probability of internal defects. The quality of the

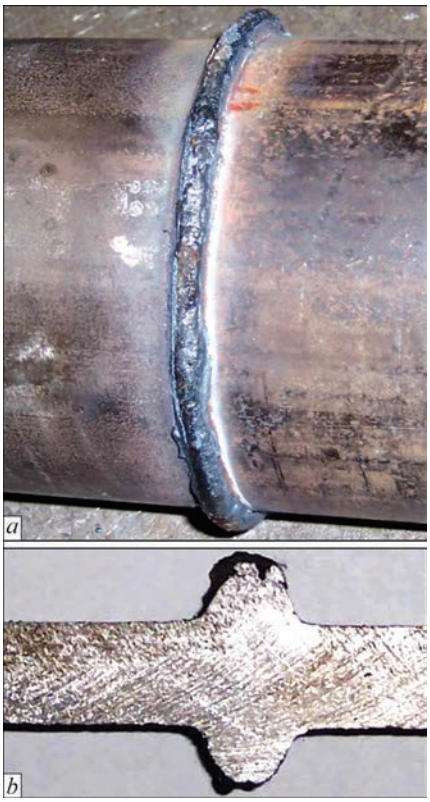

Figure 13. Formation of a welded pipe joint without an upset allowance, where: *a* — welded joint; *b* — cross-section of the welded joint

welded joint can be ensured even without the use of gas shielding, provided that the arc rotation speed at the moment before the upset is sufficient for constant renewal of the melt layer on the entire surface of the ends. This prevents crystallization of the metal in the time intervals between the passage of the arc through

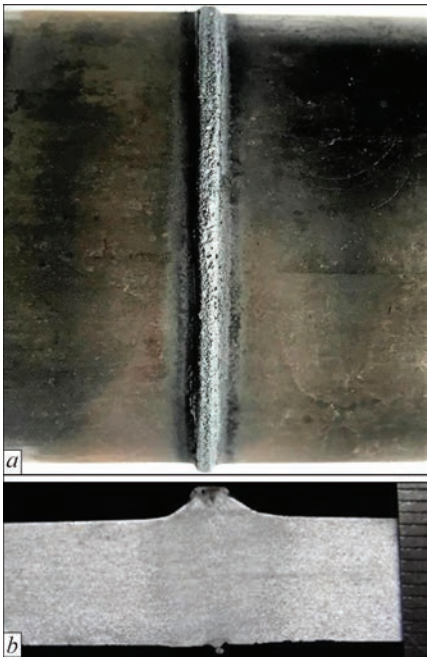

Figure 14. Formation of a welded joint with a controlled upset, where: *a* — welded joint; *b* — cross-section of the welded joint

Table 3. Basic technological parameters for welding

Steel grade	Pipe size, mm	Welding time, s	Upset force, kN	Pipe shortening, mm
09G2S	42/4	14	40.6	3.6
JIS STPG410	60.5/5.5	19	80	4.8
St35	76/16	82	255	12.4
DIN 17100 St52-3	90/5	16	135	4.8
ASTM A615 Grade 520	121/7	27	200	6.7
ASTM A615 Grade 520	121/10	43	278	9.2
API X70	168/7	31	247	6.8
API X70	219/8	38	281	7.7
ASTM A106 API 5L	114.3/6	19	140	5.7
ASTM A106 API 5L	148.3/6	28	171	5.6

Table 4. Mechanical properties of welded pipe joints

Steel grade	Pipe size, mm	σ_t, MPa		KCV_{+20}, J/cm^2		KCV_{-20}, J/cm^2		KCV_{-40}, J/cm^2
		Base metal	Welded joint	Base metal	Welded joint	Base metal	Welded joint	Welded joint
09G2S	42/5	469±10	465±14	56±5	68±10	58±3	69±5	–
JIS STPG410	60/5.5	458±10	456±10	94±4	87±3	96±3	91±4	92±3
St35	89/10	551±14	541±13	60±3	70±19	–	–	–
DIN 17100 St52-3	90/5	498±11	486±7	–	–	–	–	–
API X70	168.6/7.8	551±19	540±8	256±10	189±48	257±9	197±39	–
ASTM A615 Grade520	191/7	651±14	656±22	135±14	119±31	–	–	–
ASTM A106 API 5L	114.3/6	421±14	418±15	–	–	–	–	–
ASTM A106 API 5L	148.3/6	429±12	437±14	–	–	–	–	–

individual sections, which, in turn, contributes to the formation of a uniform and strong joint.

The formation of welded joints of pipes with a diameter of Ø140×8 mm, made without a controlled allowance for upset is shown in Figure 13, *a*. Figure 13, *b* shows a cross-section of the welded joint. The height of the external and internal reinforcement is up to 7 mm, which does not meet the requirements of API standards.

Controlling the pipe upset allowance after welding allows a significant reduction in the height of the welded joint reinforcement from 1.0 to 3 mm, depending on the pipe diameter, Figure 14.

Table 3 presents the main technological parameters for welding pipes with controlled upset.

Mechanical tests of pipe joints were carried out in accordance with the requirements of API [20] and DNV standards. The mechanical properties of welded pipe joints are shown in Table 4.

All joints of the specified pipes welded by the MIAB method without further heat treatment demonstrated impact toughness at test temperatures of +20,

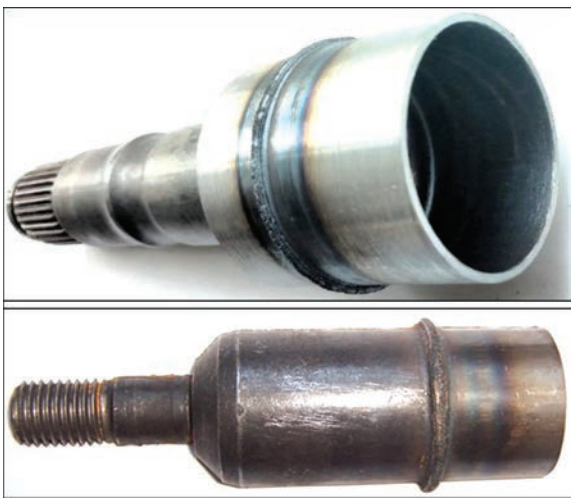

Figure 15. Parts of the automobile assortment

Figure 16. Welding pipes with fittings

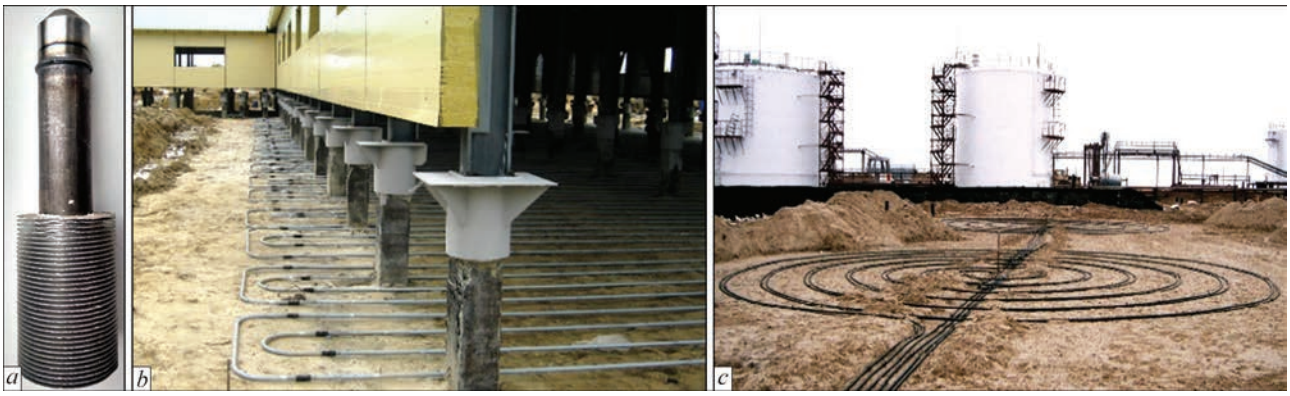

Figure 17. Welding of pipelines for soil thermal stabilization systems, where: *a* — welded joints of the pipe with the bottom; *b* — system for soil thermal stabilization: building foundations; *c* — and oil and gas storage facilities

–20 and –40 °C at a level not lower than 80 % of the corresponding indices of the base metal.

Areas of application developed at PWI, Ukraine, MIAB welding technology & machine:

- automotive industry — welding of automobile shafts for various purposes (Figure 15);
- hydraulic systems of construction machinery — welding of pipes with fittings (Figure 16);
- pipeline construction — welding of pipes for soil thermal stabilization systems (Figure 17).

TECHNICAL ADVANTAGES OF THE MIAB WELDING PROCESS FOR PIPES, PIPELINES AND AUTOMOTIVE INDUSTRIES

The process has a number of important technical advantages:

- relatively short welding time;
- high productivity, especially in mass production;
- no need in welding materials and shielding gases, which reduces the cost of the process and simplifies its organization;
- localized (concentrated) heating of the ends of welded pipes;
- minimal allowances for melting and upset;
- unpretentiousness to the cleanliness of the side and welded surfaces;
- no strict requirements for the accuracy of preliminary preparation of parts;
- insignificant metal spatter during the process;
- the ability to control and record the main technological parameters in real time.

INNOVATIVE SOLUTIONS AND COMPLIANCE WITH STANDARDS

The use of this process allows you to reduce the duration of welding by up to 70 % compared to traditional methods.

The use of technology with pulsed welding current increase and precision upset in MIAB welding installations provides:

- increased energy efficiency of the welding process;
- improved technological quality of welded joints;
- reduced cost of welding equipment;
- reduced peak loads on the electrical mains by 50–70 % compared to traditional methods.

In addition, the MIAB welding process meets the requirements of the API 1104 standard, which is widely used in pipeline welding in many countries around the world. This indicates its compliance with international requirements for the quality, reliability and safety of welded joints.

REFERENCES

1. Ganovski, F.J. (1974) The magnetarc welding process. *Welding and Metal Fabrication*, **6**, 206–213.
2. Johnson, K.I., Carter, A.W., Dinsdale, W.O. et al. (1979) The magnetically impelled arc butt welding of mild steel tubing. *Welding J.*, **59**, 17–27.
3. Takagi, K., Aracida, F. (1982) Magnetically impelled arc butt welding of gas pipeline. *Metal Construction*, **10**, 542–548.
4. Steffen, W. (1982) Pressure welding of pipes with a magnetically displaced arc. *Schweißen. Schneid. Transl.*, **4**, E70–E72.
5. Edson, D.A. (1982) *Magnetically impelled arc faying surfaces welding of thick wall pipes*. IIW IM-726–82.
6. Kachinskiy, V.S., Krivenko, V.G., Ignatenko, V.Yu. (2002) Magnetically impelled arc butt welding of hollow and solid parts. IIW, III-1208–02. *Welding in the World,* 46(**7–8**), 49–56. DOI: https://doi.org/10.1007/BF03263390
7. Leigh, F., Cec, S., Gabriel, S. (2003) *MIAB welding: breakthrough technology for high productivity field welding of pipelines*. APIA National Convention Pipelines — Yesterday, Today and Tomorrow Convened by the Australian Pipeline Industry Association.
8. Norrish, J., Cuiuri, D., Hossain, M. (2005) Modelling and simulation of the magnetically impelled arc butt (MIAB) process for transmission pipeline applications process. In: *Proc. of the Inter. Pipeline Integrity Conf., Sydney, Australia, 7–9 March 2005*.
9. Iordachescu, D., Georgescu, B., Iordachescu, M. et al. (2011) Characteristics of MIAB welding process and joints. *Weld World*, **55**, 25–31.
10. Vendan, S.A., Manoharan, S., Nagamani, C. (2012) MIAB welding of alloy steel pipes in pressure parts: Metallurgical characterization and non-destructive testing. *JMP*, **14**, 82–88.
11. Kachinskiy, V., Hiroshi Imaizumi (2012) Magnetically-impelled arc butt welding for manufacture of hollow parts of mass production. *Welding Technology J. Japan*, **60**, 68–73.

12. Arungalai Vendan, S., Manoharan, S., Buvanashekaran, G., Nagamani, C. (2012) Strength assessingment using destructive testing on MIAB welded alloy steel pipes and subsequent techno-economical evaluation. *JMP*, **14**, 328–335.
13. Arungalai Vendan, S., Mundla, S., Buvanashekaran, G. (2012) Feasibility of magnetically impelled arc butt (MIAB) welding of high-thickness pipes for pressure parts. *Mater. Manuf.*, **27**, 573–579.
14. Hagan, D., Riley, N. (1979) MIAB welding. Pt 2. Fabrication the fiesta rear axle. *Metal Construction*, **12**, 625, 627–629.
15. (1980) Magnetarc: Schweissen mit magnetisch bewegtem Lichtbogen. KUKA, Augsburg. Vesttyskland. *Schweisstechnik*, **11**, 36.
16. Kachinskiy, V.S., Kuchuk-Yatsenko, S.I., Ignatenko, V.Yu. (2010) Magnetically-impelled arc butt welding of automobile parts. *Australasian Welding J.*, **55**, Second Quarter, 40–48.
17. Kachynskyi, V.S., Allford, D., Drachenko, M.P. et al. (2024) Development of the technology of pressure welding with a magnetically impelled arc of small-diameter pipes using supercapacitors. *The Paton Welding J.*, **10**, 3–10. DOI: https://doi.org/10.37434/tpwj2024.10.01
18. Koval, M.P., Kuchuk-Yatsenko, S.I., Kachynskyi, V.S. (2020) System of control, record of parameters and monitoring in the process of press welding of pipes using magnetically-impelled arc. *The Paton Welding J.*, **6**, 36–40. DOI: https://doi.org/10.37434/tpwj2020.06.07
19. Kachinskiy, V.S., Kuchuk-Yatsenko, S.I. (2017) Joint formation in magnetically-impelled arc butt welding of thick-walled pipes from high-strength steels. *The Paton Welding J.*, **8**, 39–45. DOI: https://doi.org/10.15407/tpwj2017.08.06
20. (2013) API Standart 1104: *Welding of pipelines and related facilities*. American Petroleum Institute.

ORCID
V. Kachynskyi: 0000-0001-9695-6434,
V. Klymenko: 0000-0002-8709-5924

CONFLICT OF INTEREST
The Authors declare no conflict of interest

CORRESPONDING AUTHOR
V. Kachynskyi
E.O. Paton Electric Welding Institute of the NASU
11 Kazymyr Malevych Str., 03150, Kyiv, Ukraine.
E-mail: vskweld@gmail.com

SUGGESTED CITATION
V. Kachynskyi, D. Allford, V. Klymenko (2025) MIAB welding technology of pipes and parts of automotive industry. *The Paton Welding J.*, **8**, 19–28. DOI: https://doi.org/10.37434/tpwj2025.08.02

JOURNAL HOME PAGE
https://patonpublishinghouse.com/eng/journals/tpwj

Received: 09.05.2025
Received in revised form: 17.06.2025
Accepted: 22.07.2025

DOI: https://doi.org/10.37434/tpwj2025.08.03

OBTAINING FUNCTIONALLY-GRADED METAL-MATRIX MATERIALS Ti–6Al–4V + WC IN THE PROCESS OF 3D PRINTING BY THE METHOD OF ADDITIVE PLASMA-ARC DEPOSITION

V. Korzhyk[1], **A. Grynyuk**[2], **O. Babych**[2], **O. Berdnikova**[1], **Ye. Illiashenko**[1], **O. Bushma**[1]

[1]E.O. Paton Electric Welding Institute of the NASU
11 Kazymyr Malevych Str., 03150, Kyiv, Ukraine
[2]Scientific-Research Institute of Welding Technologies in Zhenjiang Province
233 Yonghui Road, Xiaoshan District, Hangzhou City, Zhejiang Province, China

ABSTRACT

The possibility of 3D printing by additive plasma-arc surfacing of three-dimensional products from composite functionally-graded metal-matrix materials, in which the matrix is the titanium alloy Ti–6Al–4V and the reinforcing phase is tungsten carbide, has been experimentally confirmed. The technology of additive plasma-arc deposition with simultaneous feeding of powder or filler wire of titanium alloy Ti–6Al–4V Grade 5 and spherical WC powder into the plasma arc allows obtaining three-dimensional samples from functionally-graded metal-matrix materials of the "wall" type, in which the content of tungsten carbide along their height varies from 0 to 50 vol.% with a corresponding change in the hardness index from *HRC* 32 for the lower (deep) layers and up to *HRC* 56–66 and higher towards the surface layers. By selecting plasma spraying modes and energy input, it is possible to change the hardness, microstructure, and microhardness of the matrix of the material of the deposited layers, including the degree of melting of spherical WC powder particles, namely, to preserve their spherical shape with a microhardness of *HV*0.1 = 2172–3796 or to achieve their partial and complete melting. In the case of preserving the spherical shape of WC particles in a matrix of titanium alloy Ti–6Al–4V, the presence of a metallurgical bond between them and this matrix is characteristic. It has been established that the tensile strength of the obtained materials for the case of additive deposition with Ti–6Al–4V filler wire with the addition of WC powder up to 50 vol.% reaches σ_t = 666.8 MPa, which corresponds to 75 % of the tensile strength of the Ti–6Al–4VBT6 Grade 5 alloy of identical chemical composition (annealed sheet), which acts as the matrix of the studied composite material. The impact strength of the samples of wall-type joints with welded layers of the composite material Ti–6Al–4V Grade 5 alloy + WC powder reaches up to 70–80 % of the level of this parameter of the Ti–6Al–4V Grade 5 titanium alloy sheet.

KEYWORDS: 3D printing, additive plasma-arc deposition, titanium alloys, tungsten carbide, functionally-graded materials, structure, mechanical properties

INTRODUCTION

In modern additive manufacturing two approaches are predominantly used to make a finished metal product [1–18]: layer-by-layer selective melting of the powder or direct growing of the part wall from the material in the powder or wire form. The energy of the laser (SLM) or electron beam (EBSM) is used for the processes of selective melting of the powder. Both these processes ensure forming parts according to the dimensions specified in the models. After 3D printing by these methods no machining of the part surface is used in most cases. These processes, however, have a number of disadvantages, namely: limited part dimensions, need to use fine powders (predominantly, 20–63, 20–105 μm) with a high coefficient of sphericity; need to use several times greater amount of the powder than the finished part volume, when growing a part with gradient differences in the mechanical properties at successive application of powders of different chemical composition, their mixing beyond the fusion zone occurs, which causes the need for rejection of the powder, remaining in the unit after printing is over.

Among additive technologies, using the deposition methods, the Wire Direct Energy Deposition/Wire Arc Additive Manufacturuing/3D Metal Printing (DED-W/WAAM/3DMP) or WAAM processes became the most widely accepted. They include the arc processes with application of nonconsumable or consumable electrode, as well as processes with short-circuiting of the arc gap (of Cold Metal Transfer (CMT) type) [19–20]. Particular attention is given to Plasma Metal Deposition (PMD) or additive plasma-arc deposition (APAD), which uses the energy of the plasma arc and has considerable potential, both in terms of realization of wide technological capabilities, and producing new materials during 3D printing [20].

It is necessary to note the following advantages and wider technological capabilities of PMD, compared to WAAM methods [20]:

- broad adjustment of the 3D printing productivity (from 0.02 up to 25 kg/h) and degree of detalization of volumetric elements (from 2.0–2.5 up to 10–20 mm

wide) through realization of the process, both in the mode of microplasma deposition with a low-current plasma arc (at currents of 5–35 A), and at currents of 50–450 A and higher (depending on the power of the welding current power source of plasma deposition unit);

● large range of adjustment of the energy input, heating zone and depth of penetration of the layers previously deposited by APAD, using transferred or non-transferred arc;

● 3D printing at straight and reverse polarity current, alternating current, including realization of the process of cathodic cleaning and destruction of the oxide films, at surfacing of light metal and alloys with high-melting oxide films on their surface;

● 3D printing using from one to four filler wires, including those with current-conducting wire with preheating;

● using solid and composite (flux-cored) wires, powders of light alloys and refractory metals, composite powders and mechanical mixtures of powders of alloys, metal ceramics, carbides, borides, etc., as filler material for 3D printing;

● realization of the process of 3D printing using a filler, which does not move together with the plasmatron during the layer deposition (metal grit, foil, thin metal strips), which is applied alternately after deposition of each layer (process, similar to "lamination" or selective melting);

● possibility of igniting the plasma arc without adding wire or powder, which allows conducting preheating of the base or deposited layers before additive deposition.

THE OBJECTIVE OF THE WORK

is confirmation of the possibility of additive plasma-arc deposition to produce during 3D printing spatial products from functionally-graded metal-matrix materials, where the metal matrix contains reinforcing grains of refractory compounds (carbides, borides, etc.) of a variable composition.

To achieve this objective it is necessary to:

● using additive plasma-arc deposition with simultaneous feeding into the plasma arc of powder or filler wire from titanium alloy Ti–6Al–4V Grade 5 and spherical WC powder, produce composite functionally-graded materials, where the matrix is titanium alloy Ti–6Al–4V, and tungsten carbide is the reinforcing phase of a varying content;

● study the structure of the produced composite materials and the possibility of controlling the degree of melting of spherical particles of tungsten carbide in the titanium alloy matrix;

● determine the main physical and mechanical properties of the produced Ti–6Al–4V+WC composite materials, compared with the characteristics of Ti–6Al–4V matrix alloy.

RESEARCH MATERIALS AND METHODS

Experiments were performed in the equipment developed in cooperation by PWI and RPC PLASER Ltd (Ukraine) [20] (Figure 1, *a*, *b*). In order to conduct the research, 3D products of "wall" type of the dimensions from 8×4 to 8×50 mm were made, using a specially developed all-purpose plasmatron (Figure 1, *c*), which allows realization of the process of additive deposition at simultaneous feeding of one or several powders, or simultaneous feeding of the powder and filler wire [20–23]. The possibility of producing a composite volumetric functionally-graded material of Ti–6Al–4V Grade 5 alloy + WC powder by realization of two technologies of additive plasma-arc deposition by: a) simultaneous feeding of dissimilar powders from two powder dispensers; b) addition of a mechanical mixture of powders from one feeder;

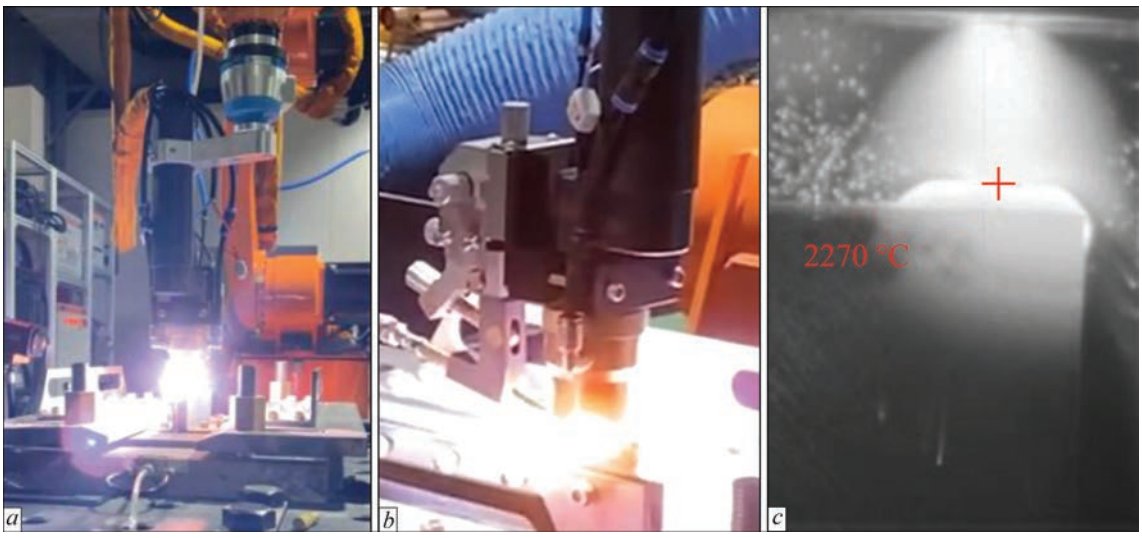

Figure 1. Robotic complex (*a*) and plasmatron (*b*), used to produce 3D samples of "wall" type and the process of plasma-arc deposition (*c*) of a single 2 mm layer during formation of the "wall" from a composite material with simultaneous feed of Ti–6Al–4V wire and spherical WC powder (*c*)

c) simultaneous feeding of a titanium alloy wire and tungsten carbide powder.

At the first stage of investigations plasma deposition was performed using a mixture of Ti–6Al–4V and WC powders. Owing to different density of the powders, the mechanical mixture started separating into individual components in the powder feeder hopper, and it was difficult to predict the presence of a specific amount of powder in the WC deposit.

In order to improve the stability of WC powder supply to the deposited metal, it was decided to either feed the WC and Ti–6Al–4V powder separately from different feeders, or feed the WC in the form of powder, and Ti–6Al–4V alloy in the form of wire. Considering that the coefficient of utilization of the material in the form of wire was higher than a similar coefficient in the powder, it was decided to feed the Ti–6Al–4V alloy in the form of wire. Wire 1.2 mm in diameter from Ti–6Al–4V titanium alloy was used, and the size of spherical particles of tungsten carbide was equal to 50–150 μm. Samples of "wall" type were grown during 3D printing on a substrate from 8 mm Ti–6Al–4V Grade 5 alloy. Deposition was performed on the end face of a sample 8 mm wide and 60 mm long.

Structural characteristics of the produced materials were studied using complex methods, which include measurement of hardness, microhardness, metallographic investigations of the structure, X-ray diffraction analysis and analysis of the chemical composition, using the procedure, described in [24–29]. Rockwell hardness (*HRC*) was measured in Laizhou Weiyi HRS-150S instrument, Vickers microhardness (*HV*) — in VH1102 instrument (USA) at 100 g load. Microstructural studies of the materials were conducted with application of a light microscope Zeiss Axio Imager M2m, and scanning electron microscope SEM-515 (Philips Company, Holland).

To determine the rupture strength of the deposited metal, 4 mm sheets from Ti–6Al–4V alloy were welded on a substrate from Ti–6Al–4V alloy. Sheets 4 mm thick were assembled with a guaranteed gap of 4 mm (Figure 2, *a*), in order to form a weld predominantly from filler material, namely Ti–6Al–4V titanium wire and WC powder. Here, the titanium wire feed rate

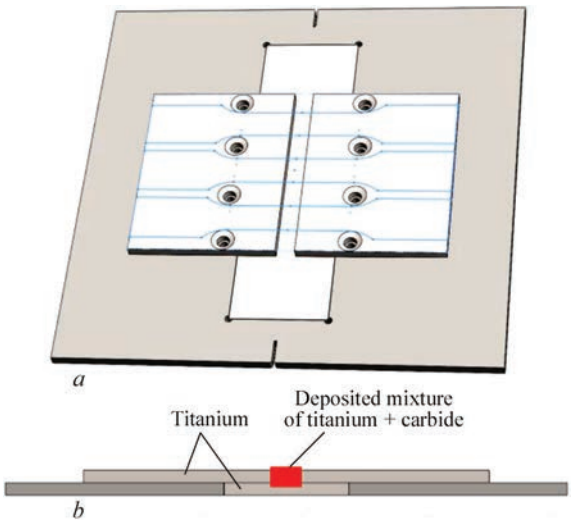

Figure 2. Schemes of sample layout when welding 4 mm sheets to determine the tensile strength of the weld metal

remained unchanged, but the amount of WC powder was changed, to ensure its content in the weld equal to 30 and 50 % of the total weld volume. Mechanical testing for ultimate strength and relative elongation of the studied samples with a deposits was conducted in an electronic universal Instron-5988 system. Size of samples for testing in keeping the standard was 12.5×3.22×128.5 mm, location of rupture was in the deposited material in all the samples. Samples for testing were cut out by spark cutting in the form of "spades" (Figure 2, *a*) with titanium at the edges and a strip of the deposited material in the middle, from material deposited into the gap between the two titanium plates (Figure 2, *b*). This allowed obtaining data on composite 3D samples of Ti–6Al–4V Grade 5 alloy + deposited layer + Ti–6Al–4V Grade 5 alloy.

Impact toughness testing of samples from the produced materials was conducted in Steel Research Nake NI300C system, using the methodology described in [29–32]. Dimensions of the test samples were as follows 10.0×10.0×55.0 mm. In order to measure the impact toughness of samples with a deposits, taking into account the zone of the deposited material fusion with the base, testing was conducted by two variants of the schemes: with application of the "frontal impact" (Figure 3, *a*) and "lateral impact" (Figure 3, *b*) with

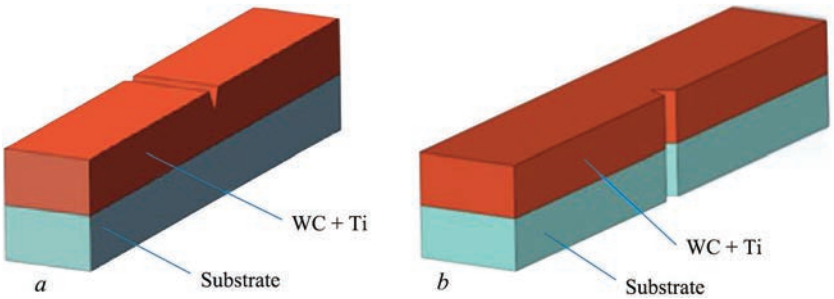

Figure 3. Schematic images of impact testing variants of samples with deposits: *a* — with application of "frontal impact"; *b* — "lateral impact"

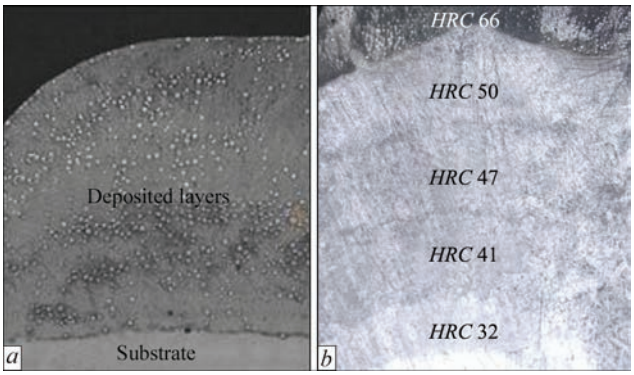

Figure 4. General view of the samples (*a*) and structure of a fragment of a sample (*b*, ×10) of "wall" type from a functionally-graded Ti–6Al–4V + WC material with WC content varying by sample height

a 2 mm deep notch. Test samples of 10 mm height were cut out, of which 5 mm are the substrate and 5 mm is the deposited layer. This allowed deriving data on two-layer samples of substrate + deposited layer, namely of Ti–6Al–4V alloy Grade 5 + deposited layer composite material.

INVESTIGATION RESULTS

The process of formation of a single layer 2 mm thick when manufacturing a 3D product of "wall" type with simultaneous feeding of Ti–6Al–4V wire and tungsten carbide is shown in Figure 1, *c*. Results of technological investigations enabled producing 3D products from Ti–6Al–4V + WC composite materials with adjustment of tungsten carbide content (Figure 4, *a*).

It is confirmed that the developed technology allows producing 3D multilayer material of gradient type and varying the content of tungsten carbide from 0 up to 50 % and, accordingly, the hardness by volume (height) from *HRC* 32 for the lower (deep-lying) layers from Ti–6Al–4V titanium alloy up to *HRC* 56–66 and higher towards the surface layers (Figure 4, *b*).

No pores or other defects were found in the material of the deposited layers of the produced samples. The fusion lines of the deposited layers are homogeneous (Figure 5, *a*). The line of fusion with the titanium substrate, on which samples of "wall" type were grown, is also homogeneous (Figure 5, *b*). For spherical WC particles with microhardness *HV*0.1 = 2172–3796, located in the matrix from Ti–6Al–4V titanium alloy, presence of a metallurgical bond with the matrix is characteristic, at their relatively uniform distribution in the material of this matrix (Figure 5, *c*, *d*).

Selection of plasma deposition modes and energy input allows varying the hardness, microstructure and microhardness of the matrix material of the deposited layers, including the degree of melting of spherical WC powder particles, namely reach their partial (Figure 6, *a*, *b*) or complete (Figure 6, *c*) melting.

So, for instance, partial melting of the carbide phase can be achieved along the WC/matrix interfac-

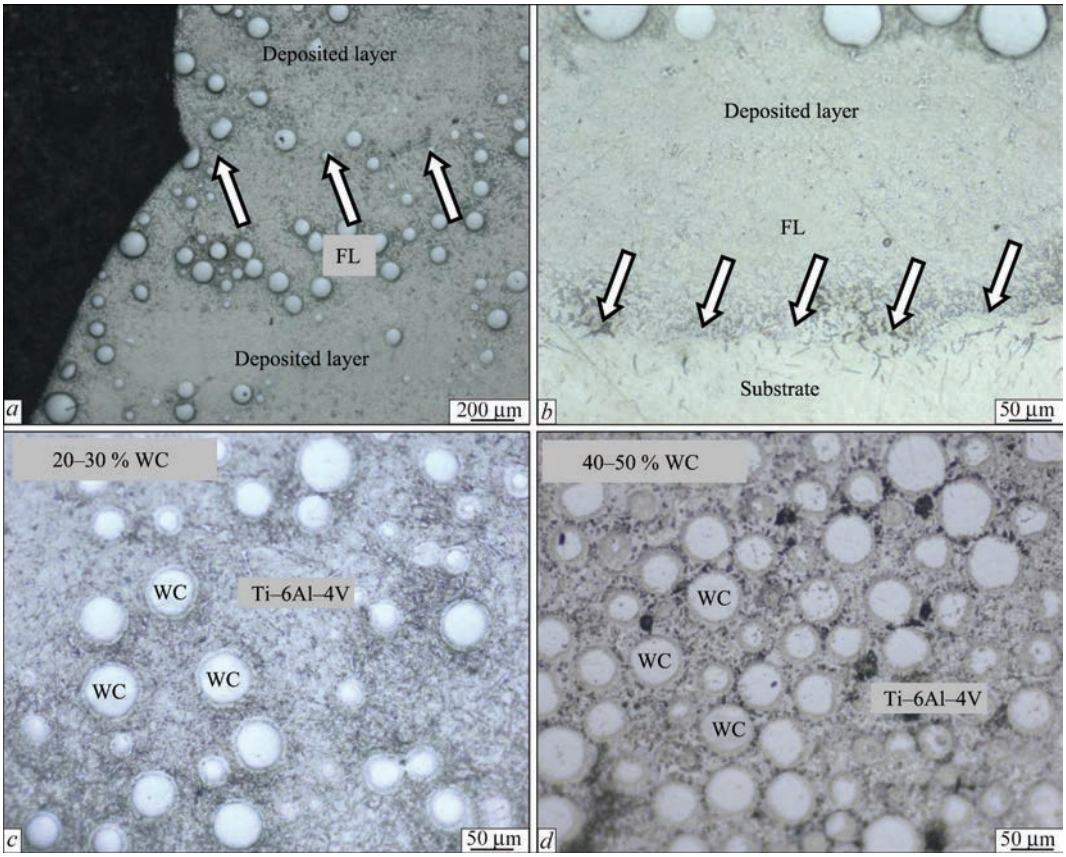

Figure 5. Microstructure of fragments of deposited layers in a sample of "wall" type from functionally-graded Ti–6Al–4V + WC material: *a*, *b* — fusion lines (FL); *c*, *d* — deposited layers with WC content varying by height (*a*, ×50; *c*–*e*, ×200)

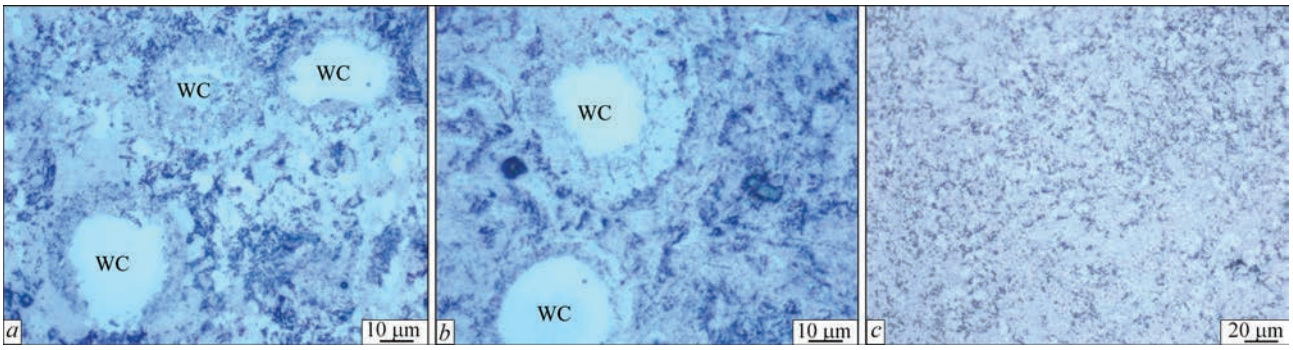

Figure 6. Microstructure of the material of Ti–6Al–4V + WC deposits

Table 1. Mechanical and structural parameters of the deposited layers: *n* is the number of the deposited layers; δ is the total thickness of the deposit; *HRC* is the maximal hardness from the deposit surface; *HV* is the cross-sectional microhardness; V_p is the maximal content of WC particles in the deposit material; σ_t is the rupture strength

No.	Deposited material type	*n*	δ, mm	*HRC*	*HV*0,1		V_p, %	σ_t, MPa
					Lower layer	Upper layer		
1	Ti–6Al–4V + WC powders	2	3.1	61	317.2–346.5	373.3–468.7	30	586.4
2		2	3.6	58	348.4–360.2	377.3–380.0	25	605.4
3	Ti–6Al–4V wire + WC powder	6	15	53	410.7–550.5	465.2–1187.4	40	611.4
4		2	8	66	479.4–859.0	706.0–1055.8	50	666.8
5		1	3.4	54.6	321.4–473.0	–	30	584.5
6		2	6.7	55.2	346.2–408.9	400.6–541.9	30	641.8

es in the deposited layers (Figure 6, *a*, *b*). In this case, the WC particles have already lost their spherical shape, and an interlayer enriched in tungsten and carbon is observed around them, where a new structure with a component of a stoichiometric composition of (W, Ti) C_x forms. Some WC particles have almost melted, but their initial WC particle/matrix interfaces are still observed (Figure 6, *a*). Some particles have dissolved completely. Their structure corresponds to that of the molten interlayers along the WC particle/matrix interfaces in the deposited layers (Figure 6, *c*).

For a more detailed analysis of physical and mechanical properties of the produced materials, several types of samples made by additive deposition using powder or wire from Ti–6Al–4V alloy with addition of WC powder during additive deposition we studied (Table 1).

Detailed analysis of the chemical composition of the deposit material confirmed the presence of WC powder solution (Table 2, Figure 7, *a*, local analysis Nos 1–6) in Ti–6Al–4V "matrix" and W content of up to 55 % (Table 2, Figure 7, *a*, *b*, fragments Nos 7, 8). It can be assumed that formation of exactly the dispersed particles of the carbide phases is observed in the volume of the deposited layer "matrix" (Figure 7, *b*).

X-ray phase analysis of the deposited layer material revealed the presence of the following phases: (α + β) — Ti; WC and WC + W_2C. It can be assumed that formation of W_2C carbide leads to additional strengthening of the deposit "matrix" material.

Mechanical rupture testing showed that the maximal values of σ_t = 641.8 and σ_t = 666.8 MPa are characteristic for samples Nos 6 and 4 (rupture point is the deposited material), with WC content of up to 30 and 50 %, respectively, which were produced by additive deposition, using Ti–6Al–4V filler wire with addition of WC powder (Table 1). Such strength values of the composite 3D samples of Ti–6Al–4V Grade 5 alloy + deposited layer + Ti–6Al–4V Grade 5 alloy correspond to 72–75 % of the ultimate strength of Ti–6Al–4VBT6 Grade 5 alloy (annealed sheet), identical in its chemical composition to the studied titanium alloy, acting as the matrix of the studied composite material [33–36]. In the deposited layers of sample No. 4 the volume fraction (V_p) of WC particles in the lower layer is equal to 50 %. The microstructure of the deposit upper layer is homogeneous with the microhardness of *HV* = 706.0–1055.8. In the upper zone of the deposit second layer WC particles are present in a small quantity. The lower layer microhardness is equal to *HV* = 479.4–859.0. Thus, at transition to from the lower layer into the upper one, *HV* increases by 30 % on average. The deposited material microstruc-

Table 2. Results of elemental analysis (wt.%) of the deposit material of sample No. 6 (Ti–6Al–4V wire + WC powder)

No.	1	2	3	4	5	6	7	8
Ti	23.7–21.3	37.1–39.4	53.4–68.9	43.5–79.2	44.7–59.1	50.9–70.7	57.8–68.3	44.9–51.3
W	76.4–78.7	60.6–62.9	31.1–46.6	20.8–56.5	40.9–55.3	29.3–49.5	31.7–42.23	48.7–55.1

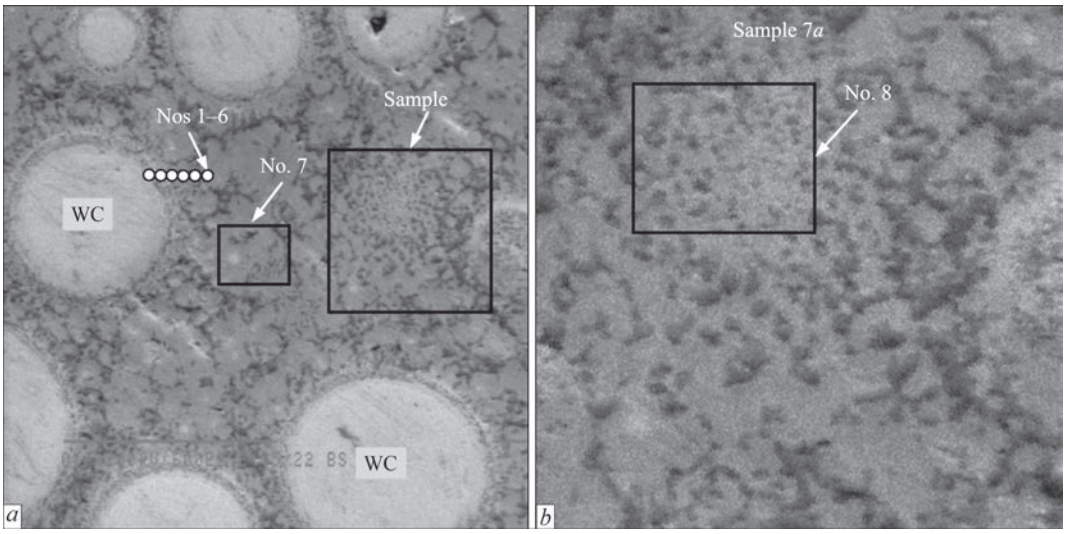

Figure 7. Material microstructure of the deposit of sample No. 6 (VT6 wire + WC powder), *a*×600; *b* — 10 times magnification of the fragment in Figure 7, *a*

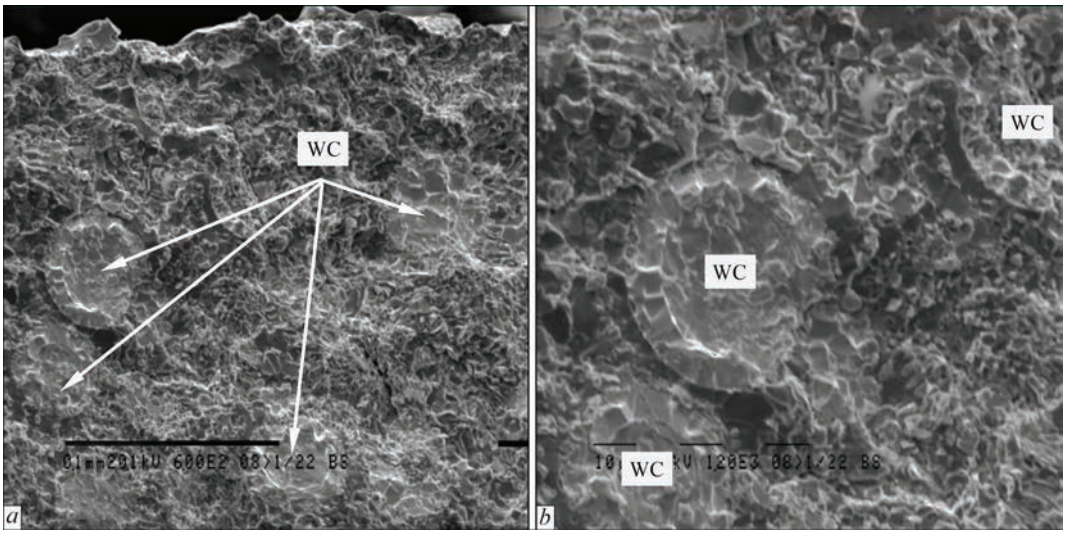

Figure 8. Fractograms of fracture surface of the deposit material of sample No. 6 (VT6 wire + WC powder) (*a*, ×600; *b*, ×1200)

ture in the two-layer sample No. 6 is characterized by 30 % volume fraction of WC particles at their even distribution in the first and second layers and gradient-free microhardness level (Table 1).

As a result of impact toughness tests of samples of "wall" type joints with deposited layers of Ti–6Al–4V Grade 5 alloy + WC powder composite material the following was established: this value is equal to 10.75–17.375 J/cm^2 for the studied samples with the content of tungsten carbide particles with the volume fraction of V_p = 30 % in the deposit material "matrix". The impact toughness value of Ti–6Al–4VBT6 Grade 5 alloy, used as the substrate for growing a wall from Ti–6Al–4V + WC material, is in the range of 19.5–21 J/cm^2. Thus, the 3D samples (10 mm in height, of which 5 mm is the substrate and 5 mm is the deposited layer) of different types of Ti–6Al–4V + WC composite material, produced by additive plasma deposition, are characterized by the overall impact toughness level, which can reach 70–80 % of that of this parameter for sheet Ti–6Al–4V Grade 5 the titanium alloy.

Fractographic studies of the fracture surface of the deposit material (BT6 wire+WC powder) revealed the following. Unmelted WC particles are characterized by brittle fracture (Figure 8).

The fracture mode of the deposit "matrix" material is predominantly mixed quasibrittle, with facet size of 3–8 μm and tough component with dispersed pits of 1–3 μm size. Such structural features of the microrelief of fracture surface of the deposit "matrix" are indicative of a set of high strength and toughness properties of the deposit material.

CONCLUSIONS

1. It was confirmed that the technology of plasma-arc additive deposition with simultaneous feeding of powder or filler wire of Ti–6Al–4V titanium alloy and spherical WC powder into the plasma arc allows producing 3D samples from functionally-graded met-

al-matrix materials, where the matrix is the titanium alloy with WC reinforcing phase. Such a technology realizes the possibility of varying the tungsten carbide content from 0 to 50 vol.% by the volume (sample height) and accordingly, change the hardness from *HRC* 32 for the lower (deep-lying) layers to *HRC* 56–66 and higher towards the surface layers.

2. Obtained materials are characterized by a defectfree structure, and the fusion lines of the deposited layers are homogeneous. By selecting the plasma deposition modes and energy input it is possible to change the hardness, microstructure and microhardness of the matrix of the deposited layer material, including the degree of melting of spherical WC powder particles, namely, preserve their spherical shape with microhardness *HV*0.1 = 2172–3796, or reach their partial or complete melting. In the case of preservation of the spherical shape of WC particles, present in the matrix from Ti–6Al–4V titanium alloy, a characteristic feature is preservation of the metallurgical bond with this matrix.

3. It was established that the ultimate strength of the produced materials reaches the value σ_t = 641.8–666.8 MPa (rupture location is in the deposited material), when testing the composite samples of the type of Ti–6Al–4V Grade 5 alloy+deposited layer + Ti–6Al–4V Grade 5 alloy for the case of additive deposition of Ti–6Al–4V filler wire with addition of WC powder up to 50 vol.%. This corresponds to 72–75 % of the ultimate strength of Ti–6Al–4VBT6 Grade 5 alloy (annealed sheet) of identical chemical composition, acting as the matrix of the deposited composite material. Impact toughness values of the composite material of Ti–6Al–4V Grade 5 alloy+deposited layer 10 mm in height, of which 5 mm is the substrate, and 5 mm is the deposited layer with 30 % volume fraction of WC particles in the "matrix" of the deposit material reaches up to 70–80 % of the level of this parameters for the sheet titanium alloy Ti–6Al–4V Grade 5.

REFERENCES

1. Zafar, F., Emadinia, O., Conceição, J. et al. (2023) A review on direct laser deposition of Inconel 625 and Inconel 625-based composites challenges and prospects. *Metals*, **13**, 787. DOI: https://doi.org/10.3390/met13040787
2. Preis, J., Wang, Z., Howard, J. et al. (2024) Effect of laser power and deposition sequence on microstructure of GRCop42 – Inconel 625 joints fabricated using laser directed energy deposition. *Materials and Design*, **241**, 112944. DOI: https://doi.org/10.1016/j.matdes.2024.112944
3. Zhukov, V., Grigorenko, G., Shapovalov V. (2016) Additive manufacturing of metal components (Review). *The Paton Welding J.*, **5–6**, 137–142. DOI: https:/doi.org/10.15407/tpwj2016.06.24
4. Su, G., Shi, Y. Li, G. et al. (2023) Improving the deposition efficiency and mechanical properties of additive manufactured Inconel 625 through hot wire laser metal deposition. *J. of Materials Processing Technology*, **322**, 118175. DOI: https://doi.org/10.1016/j.jmatprotec.2023.118175
5. Danielewski, H., Radek, N., Orman, L. et al. (2023) Laser metal deposition of Inconel 625 alloy — Comparison of powder and filler wire methods. *Materials Research Proceedings*, **34**, 154–160. DOI: https://doi.org/10.21741/9781644902691-19
6. Gu, Y., Xu, Y., Shi, Y. et al. (2022) Corrosion resistance of 316 stainless steel in a simulated pressurized water reactor improved by laser cladding with chromium. *Surface and Coatings Technology*, **441**, 128534. DOI: https://doi.org/10.1016/j.surfcoat.2022.128534
7. Ahn, D. (2021) Directed energy deposition (DED) process: State of the Art. *Int. J. of Precis. Eng. and Manuf.-Green Tech.*, **8**, 703–742. DOI: https://doi.org/10.1007/s40684-020-00302-7
8. Svetlizky, D., Das, M., Zheng, B. et al. (2021) Directed energy deposition (DED) additive manufacturing: Physical characteristics, defects, challenges and applications. *Materials Today*, **49**, 271–295. DOI: https://doi.org/10.1016/j.mattod.2021.03.020
9. King, W., Anderson, A., Ferencz, R. et al. (2015) Laser powder bed fusion additive manufacturing of metals; physics, computational, and materials challenges. *Applied Physics Reviews*, **2**, 041304. DOI: https://doi.org/10.1063/1.4937809
10. Hassila C., Paschalidou, M., Harlin, P. et al. (2022) Potential of nitrogen atomized alloy 625 in the powder bed fusion laser beam process. *Materials and Design*, **221**, 110928. DOI: https://doi.org/10.1016/j.matdes.2022.110928
11. Rehman, A., Karakas, B., Mahmood, M. et al. (2023) Additive manufacturing of Inconel-625: From powder production to bulk samples printing. *Rapid Prototyping J.*, 23(**9**), 1788–1799. DOI: https://doi.org/10.1108/RPJ-11-2022-0373
12. Chen, G., Zhao, S., Tan, P. et al. (2018) A comparative study of Ti–6Al–4V powders for additive manufacturing by gas atomization, plasma rotating electrode process and plasma atomization. *Powder Technology*, **333**, 38–46. DOI: https://doi.org/10.1016/j.powtec.2018.04.013
13. Yurtukan, E., Unal, R. (2022) Theoretical and experimental investigation of Ti alloy powder production using low-power plasma torches. *Transact. of Nonferrous Metals Society of China*, **32**, 175–191. DOI: https://doi.org/10.1016/S1003-6326(21)65786-2
14. Prokopov, V., Fialko, N., Sherenkovskaya, G. et al. (1993) Effect of the coating porosity on the processes of heat transfer under, gas-thermal atomization. *Powder Metall. Met. Ceram.*, **32**, 118–121. DOI: https://doi.org/10.1007/BF00560034
15. Yin, Z., Yu, D., Zhang, Q. et al. (2021) Experimental and numerical analysis of a reverse-polarity plasma torch for plasma atomization. *Plasma Chem. Plasma Process.*, **41**, 1471–1495. DOI: https://doi.org/10.1007/s11090-021-10181-8
16. Bobzina, K., Ernsta, F., Richardta, K. et al. (2008) Thermal spraying of cylinder bores wi-–4443. DOI: https://doi.org/10.1016/j.surfcoat.2008.04.023
17. Fan, H., Kovacevic, R. (2004)A unified model of transport phenomena in gas metal arc welding including electrode, arc plasma and molten pool. *J. Phys. D: Appl. Phys.*, **37**, 2531–2544. DOI: https://doi.org/10.1088/0022-3727/37/18/009
18. Sun, P., Fang, Z., Zhang, Y., Xia, Y. (2017) Review of the methods for the production of spherical Ti and Ti alloy powder. *JOM*, **69**, 1853–1860. DOI: https://doi.org/10.1007/s11837-017-2513-5
19. Korzhyk, V., Khaskin, V., Grynyuk, A. et al. (2021) Comparing features in metallurgical interaction when applying different techniques of arc and plasma surfacing of steel wire on titanium. *Eastern-European J. of Enterprise Technolo-*

gies, 112(**12**), 6–17. DOI: https://doi.org/10.15587/1729-4061.2021.238634
20. Korzhyk, V.M., Grynyuk, A.A., Khaskin, V.Yu. et al. (2023) Khuan Plasma-arc technologies of additive surfacing (3D printing) of spatial metal products: application experience and new opportunities. *The Paton Welding J*., **11**, 3–20. DOI: https://doi.org/10.37434/tpwj2023.11.01
21. Korzhik, V. (1992) Theoretical analysis of the conditions required for rendering metallic alloys amorphous during gas-thermal spraying. III. Transformations in the amorphous layer during the growth process of the coating. *Powder Metall. Met. Ceram*., 31(**11**), 943–948. DOI: https://doi.org/10.1007/BF00797621
22. Fialko, N., Prokopov, V., Meranova, N. et al. (1993) Thermal physics of gas thermal coatings formation processes. State of investigations. *Fizika i Khimiya Obrabotki Materialov*, **4**, 83–93.
23. Fialko, N., Prokopov, V., Meranova, N. et al. (1994) Temperature conditions of particle-substrate systems in a gas thermal deposition process. *Fizika i Khimiya Obrabotki Materialov*, **2**, 59–67.
24. Jing, H., Yu, Shi, Gang, Zh. et al. (2022) Minimizing defects and controlling the morphology of laser welded aluminium alloys using power modulation-based laser beam oscillation. *J. Manufacturing Processes*, **83**, 49–59. DOI: https://doi.org/10.1016/j.jmapro.2022.08.031
25. Fialko, N., Dinzhos, R., Sherenkovskii, J. (2021) Establishing patterns in the effect of temperature regime when manufacturing nanocomposites on their heat-conducting properties. *Eastern-European J. of Enterprise Technologies*, 4(**5–112**), 21–26. DOI: https://doi.org/10.15587/1729-4061.2021.236915
26. Li, X., Cui, L., Shonkwiler, S. et al. (2023) Automatic characterization of spherical metal powders by microscope image analysis: a parallel computing approach. *J. Iron Steel Res*., **30**, 2293–2300. DOI: https://doi.org/10.1007/s42243-022-00907-z
27. Appa Rao, G., Srinivas, M., Sarma, D. (2006) Effect of oxygen content of powder on microstructure and mechanical properties of hot isotatically pressed superalloy Inconel 718. *Materials Sci. and Eng. A*, 435(**3**), 84–99. DOI: https://doi.org/10.1016/j.msea.2006.07.053
28. Liu, Y., Zhang, S., Zhang, L. et al. (2024) Effects of oxygen content on microstructure and creep property of powder metallurgy superalloy. *Crystals*, 14(**4**), 358. DOI: https://doi.org/10.3390/cryst14040358
29. Kvasnytskyi, V., Korzhyk, V., Kvasnytskyi, V. et al. (2020). Designing brazing filler metal for heat-resistant alloys based on NI3AL intermetallide. *Eastern-European J. of Enterprise Technologies*, 12(**6**), 6–19. DOI: https://doi.org/10.15587/1729-4061.2020.217819
30. Skorokhod, A., Sviridova, I., Korzhik, V. (1994) Structural and mechanical properties of polyethylene terephthalate coatings as affected by mechanical pretreatment of powder in the course of preparation. *Mekhanika Kompozitnykh Materialov*, 30(**4**), 455–463.
31. Gu, Y., Zhang, W., Xu, Y. et al. (2022) Stress-assisted corrosion behaviour of Hastelloy N in FLiNaK molten salt environment. *NPJ Mater. Degrad*., **6**, 90. DOI: https://doi.org/10.1038/s41529-022-00300-x
32. Mao, D., Xie, Y., Meng, X. et al. (2024) Strength-ductility materials by engineering a coherent interface at incoherent precipitates *Materials Horizons*, 11(**14**), 3408–3419. DOI: https://doi.org/10.21203/rs.3.rs-3436553/v1
33. Ren, X.P., Li, H.Q., Guo H. et al. (2021) A comparative study on mechanical properties of Ti–6Al–4V alloy processed by additive manufacturing vs. traditional processing. *Materials Sci. and Eng.: A*, 817(**10**), 141384. DOI: https://doi.org/10.1016/j.msea.2021.141384
34. Mulay, R.P., Moore, J.A., Florando, J.N. et al. (2016) Microstructure and mechanical properties of Ti–6Al–4V: Mill-annealed versus direct metal laser melted alloys. *Materials Sci. and Eng*., 666(**1**), 43–47. DOI: https://doi.org/10.1016/j.msea.2016.04.012
35. Gargi Roya, Raj Narayan Hajraa, Woo Hyeok Kima et al. (2024) Microstructural evolution and mechanical properties of Ti–6Al–4V alloy through selective laser melting: Comprehensive study on the effect of hot isostatic pressing (HIP). *J. of Powder Materials*, 31(**1**), 1–7. DOI: https://doi.org/10.4150/KPMI.2024.31.1.1
36. Gupta, R.K., Anil Kumar, V., Christy Mathew, G. Sudarshan Rao (2016) Strain hardening of Titanium alloy Ti–6Al–4V sheets with prior heat treatment and cold working. *Materials Sc. and Eng*., **662**, 537–550. DOI: https://doi.org/10.1016/j.msea.2016.03.094

ORCID
V. Korzhyk: 0000-0001-9106-8593,
A. Grynyuk: 0000-0002-6088-7980,
O. Babych: 0000-0001-5633-5721,
O. Berdnikova: 0000-0001-9754-9478,
Ye. Illiashenko: 0000-0001-9876-0320,
O. Bushma: 0009-0005-6611-4507

CONFLICT OF INTEREST
The Authors declare no conflict of interest

CORRESPONDING AUTHOR
V. Korzhyk
E.O. Paton Electric Welding Institute of the NASU
11 Kazymyr Malevych Str., 03150, Kyiv, Ukraine.
E-mail: vnkorzhyk@gmail.com

SUGGESTED CITATION
V. Korzhyk, A. Grynyuk, O. Babych, O. Berdnikova, Ye. Illiashenko, O. Bushma (2025) Obtaining functionally-graded metal-matrix materials Ti–6Al–4V + WC in the process of 3D printing by the method of additive plasma-arc deposition. *The Paton Welding J*., **8**, 29–36.
DOI: https://doi.org/10.37434/tpwj2025.08.03

JOURNAL HOME PAGE
https://patonpublishinghouse.com/eng/journals/tpwj

Received: 13.05.2025
Received in revised form: 18.06.2025
Accepted: 07.08.2025

DOI: https://doi.org/10.37434/tpwj2025.08.04

ELECTRODYNAMIC TREATMENT FOR THE CONTROL OF RESIDUAL STRESSES IN WELDED JOINTS MADE OF LIGHT, HEAT-RESISTANT ALLOYS AND AUSTENITIC STEEL

L.M. Lobanov, M.O. Pashchyn, O.L. Mikhodui, O.M. Tymoshenko

E.O. Paton Electric Welding Institute of the NASU
11 Kazymyr Malevych Str., 03150, Kyiv, Ukraine

ABSTRACT

The technology of electrodynamic treatment (EDT) of experimental specimens of thin-sheet butt welded joints made of Al-, Ni- and Ti-based alloys and austenitic steel was developed and implemented. Specialized assembly tooling was designed, which was used for automatic TIG welding of experimental specimens. The effect of EDT on the residual stress states of welded joint specimens was studied using the electron speckle interferometry method. It was found that EDT is an effective mechanism for the control of the residual stress states of welded joints made of Al and Ti alloys and austenitic steel. It is shown that in order to increase the effectiveness of EDT of Ni-based alloys, it is necessary to use higher values of electrodynamic effect power in further studies. It is also advisable to use a new treatment method based on magnetic pulsed effects on nonferromagnetic materials to optimize the residual stress states of welded joints made of Ni-based alloys.

KEYWORDS: Al-, Ni-, Ti-based alloys, austenitic steel, electrodynamic treatment, transport structures, welded joints, electron speckle interferometry, residual stress states, mechanical characteristics, chemical composition, treatment effectiveness, residual stress control

INTRODUCTION. RELEVANCE AND AIM OF THE STUDY

In the modern engineering practice of manufacturing thin-sheet welded transport structures, the traditional problem of extending their service life is associated with the need in optimizing the residual stress-strain states of welded joints. Tensile residual welding stresses (RWS) have a negative impact on the aero- and hydrodynamic characteristics, assembly accuracy, corrosion resistance and durability of products made of metal materials (MM), such as structural steels, aluminium, titanium, nickel-based alloys [1].

At present, new MM are used, which are an alternative to those traditionally used in the domestic production of transport structures. Thus, the problem of minimising the level of tensile RWS in welded joints made of new MM is relevant.

Electrophysical methods based on the use of pulsed electromagnetic fields of various lengths and configurations are challenging to control the stress states [2–12].

One of the electrophysical methods for the control of RWS is electrodynamic treatment (EDT) of welded joints, which proved its effectiveness in aircraft and shipbuilding [13–15]. The RWS relaxation during EDT occurs due to the electroplastic effect based on the synergy caused by the combined action of such components as pulsed current and dynamic load on the welded joint metal. The EDT, which can be used in manual and automatic modes, is adapted for the use in the process and after welding, including as part of automated (robotic) complexes [16, 17]. The EDT provides optimal positioning of the working tool — the electrode device (ED) — relative to the weld, the ability to treat welds of large structures in different spatial positions.

THE AIM OF THE STUDY

is to investigate the effectiveness of EDT application for the control of RWS in welded joints produced of MM, which are perspective for manufacturing of welded thin-sheet transport structures.

MECHANICAL CHARACTERISTICS OF MM

Four grades of MM were studied, which are used in the modern production of welded structures and belong to the class of "well-welded" ones. MM specimens were used in the form of sheets with overall dimensions of 500×200 mm and a thicknesses δ = 1.0 and 3.0 mm. MM No. 1 is an Al-based alloy, further MM1 (Al). MM1 (Al) is used in the manufacture of shells, panels, fuel tanks, framework and saturation of transport hull structures. The chemical composition of MM1 (Al) is shown in Table 1.

MM No. 2 is a Ti-based alloy, further MM2 (Ti). MM2 (Ti) is used in the manufacture of framework, saturation, pipelines and hulls of transport structures.

Table 1. Chemical composition of MM1 (Al) alloy plates

Mg, %	Mn, %	Fe, %	Si, %	Al
2.29	0.3	0.2	0.11	Other

Table 2. Chemical composition of MM2 (Ti) titanium alloy plates

C, %	Si, %	Fe, %	N, %	H, %	O, %	Ti
0.0074	0.005	0.046	0.0079	0.0011	0.16	Other

Table 3. Chemical composition of high-temperature MM3 (Ni)alloy

C, %	S, %	P, %	Si, %	Mn, %	Cr, %	Ti, %	W, %	Fe, %	Al, %	Mo, %	Ni
0.055	0.0023	0.0019	0.13	0.28	24.44	0.43	14.37	0.075	0.25	0.75	Other

Table 4. Chemical composition of MM4 steel (Fe–Cr–Ni)

C, %	S, %	P, %	Si, %	Mn, %	Cr, %	Ni, %	Mo, %	W, %	Nb, %	V, %	Fe
0.069	0.0047	0.005	0.27	0.4	14.55	5.39	0.89	0.86	0.15	0.18	Other

Table 5. Basic mechanical characteristics of MM specimens δ = 1 and 3 mm

No.	Grade of MMs	δ, mm	Mechanical characteristics of MM		
			$\sigma_{0.2}$, MPa	σ_t, MPa	δ_y, %
1	MM1 (Al)	1.0	229.9/206.9	271.4	11.0/13.0
2		3.0	228.1	270.7	10.3
3	MM2 (Ti)	1.0	281.1	431.5	35.2
4		3.0	275.0	430.7	34.5
5	MM3 (Ni)	1.0	438.9	858.2	57.3
6		3.0	438.0	847.5	49.7
7	MM4 (Fe–Cr–Ni)	1.0	935.7	956.3	11.2
8		3.0	930.3	946.6	11.2

The chemical composition of MM2 (Ti) alloy is shown in Table 2.

MM No. 3 is a high-temperature Ni-based alloy, further MM3 (Ni). MM3 (Ni) is used for pipelines and load-bearing elements and parts of gas equipment operating at high temperatures. The chemical composition of MM3 (Ni) alloy is shown in Table 3.

MM No. 4 is a structural austenitic steel based on Fe–Cr–Ni, further MM4 (Fe–Cr–Ni), which is corrosion-resistant and is used for pipeline parts and load-bearing elements operating in aggressive environments. The chemical composition of MM4 (Fe–Cr–Ni) steel is shown in Table 4.

Mechanical tests of plane MM specimens for uniaxial tension were conducted. The preparation and fracture of the specimens were carried out in accordance with GOST 21631–76, GOST 11701–84, and GOST 1497–84, according to which the MM specimens were cut out from the sheet along the rolled product, and the mechanical characteristics of each type of MM were evaluated by four specimens. The geometric characteristics of the specimens are shown in Figure 1.

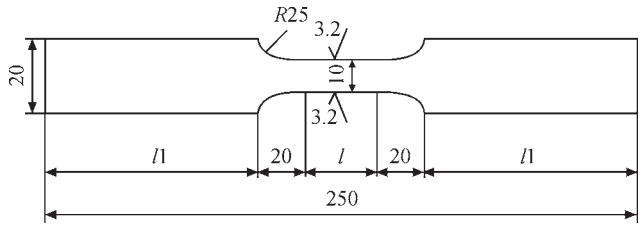

Figure 1. Appearance of specimens for uniaxial tensile tests, where l = 50 mm and $l1$ = 80 mm for grades 5A02 and TA2, l = 40 mm and $l1$ = 90 mm for grades GH3044 and S-06

A visual evaluation of the fracture pattern of the specimens of the four experimental MM was carried out, the results of which are shown in Figure 2, where the specimens δ = 1 mm are shown in Figures 1 and 2 from the top, δ = 3 mm — 3 and 4 from the top.

From the data shown in Figure 2, it can be seen that the specimens of MM1 (Al) alloy were fractured by the expressed shear and tear mechanisms, respectively (Figure 2, *a*), almost without the formation of a "contraction". The specimens of MM2 (Ti) alloy were fractured with the formation of a "contraction" mainly by the tear mechanism (Figure 2, *b*). In this case, small "shear lips" are formed along the edges of the fracture zone. The specimens of MM4 (Fe–Cr–Ni) steel (Figure 2, *c*) and MM3 (Ni) alloy (Figure 2, *d*) were fractured by the expressed shear and tear mechanisms, respectively.

The main mechanical characteristics of MM fracture as a result of static tension are given in Table 5.

The results of the chemical composition data of the aluminium MM1 (Al) alloy (Table 1) indicate that it is close to the AMg2H alloy, and the value of σ_t — to the AMg6 alloy. Titanium MM2 (Ti) alloy and nickel MM3 (Ni) alloy are characterized by high values of δ_y (lines 3–6), that creates prerequisites for the relaxation of RWS in the experimental MM as a result of electrodynamic effects and determines their prospects for the application

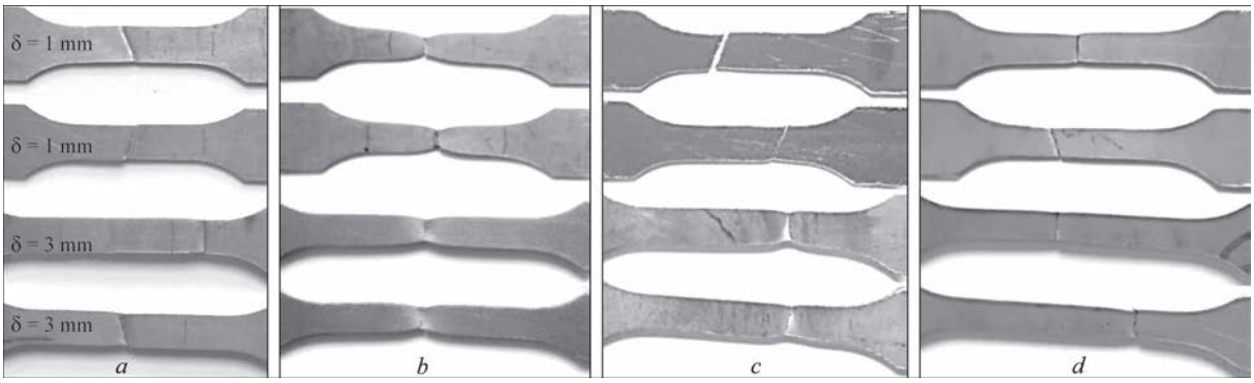

Figure 2. Appearance of fractured specimens δ = 1 and 3 mm: *a* — MM1 alloy (Al); *b* — MM2 alloy (Ti); *c* — MM4 steel (Fe–Cr–Ni); *d* — MM3 alloy (Ni)

Table 6. TIG modes — welding of MM plates δ = 1 and 3 mm

No.	Material	Arc voltage U_a, V	Arc current I_a, A	Welding speed v_w, mm/s	Electrode diameter d_e, mm	Arc gap L_a, mm
1	MM1 (Al)	12.8(13.5)	120(140)	5.0	2.4	2.0
2	MM2 (Ti)	10.2(11.3)	110(130)			1.5
3	MM4 (Fe–Cr–Ni)	11.6(11.9)	140(160)	5.5		
4	MM3 (Ni)	11.0(11.4)	140(160)			
Note. The first value of U_a, I_a — for δ = 1 mm, other — for δ = 3 mm.						

of EDT to them. MM4 (Fe–Cr–Ni) steel is characterized by rather high values of $\sigma_{0.2}$ (lines 7–8).

The formation of RWS in MM butt joint specimens was carried out using TIG welding in Ar. TIG process modes for different grades of MM are presented in Table 6.

As specimens of welded joints, MM plates with dimensions of 500×200 mm and δ = 1 and 3 mm were used, cut out along the rolled product similarly to the specimens for mechanical tests. The TIG process was carried out in a specialized assembly and welding bench (Figure 3), which provided Ar blowing to the welding zone and the cooling weld at laminar gas flow from the torch nozzle at a rate of 12 l/min. The design of the assembly bench provided blowing of the gas environment in the weld root zone due to cavities in the forming lining, through which gas circulated at a flow rate of 2 l/min (Figure 3, *a*). The TIG torch was equipped with a boot-shaped casing that isolated the cooling weld metal from atmospheric oxygen by blowing the outer surface of the welded joint with argon at a flow rate of 10 l/min (Figure 3, *b*). Based on the data in Table 6, a series of welded joint specimens made of MM was produced.

RWS of the specimens were measured by electron speckle-interferometry [18]. The method was selected due to the need to preserve the integrity of the specimen after recording its initial stress state. The specimens with the initial RWS distribution were subjected to EDT, and then the stresses were evaluated again. The effectiveness of EDT was determined by comparing the peak tensile RWS values and their distributions in the central cross-section of the specimens before and after the treatment. The longitudinal (along the weld) σ_x RWS component of the studied MM was evaluated, which has the greatest impact on the service life of welded structures [1].

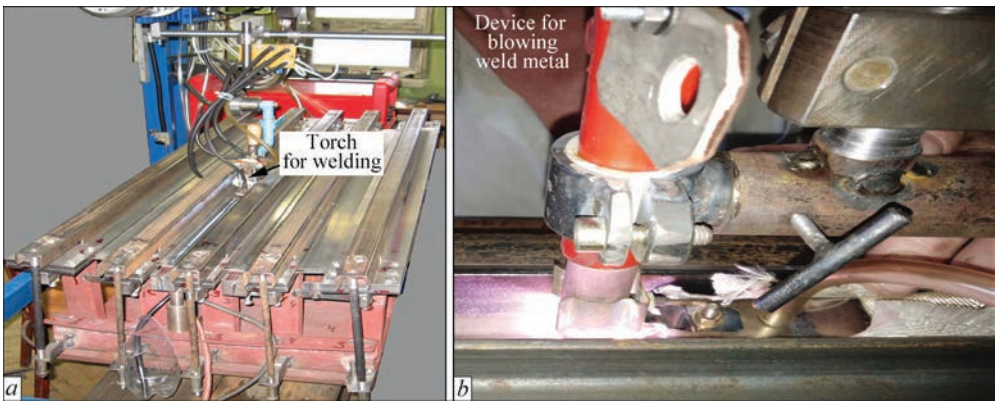

Figure 3. Appearance of the complex for TIG welding of MM: *a* — bench for assembly and welding of specimens; *b* — TIG process using blowing of the outer surface of the cooling weld metal (for TA2 alloy)

EDT PROCESS FOR WELDED JOINTS OF MM

To perform EDT, a hardware complex consisting of a power source and an electrode device (ED) was used. It was previously used for the treatment of aircraft structures [13, 14]. Before EDT, the welded joint specimens were fixed on a rigid base. EDT was performed in a "one direction" with the ED held manually, and the distance between the EDT zones ("EDT pitch") was set in the range of 5–10 mm. The treatment was applied to the outer surface of the weld centre and/or base metal along the fusion lines on both sides of the weld. The areas of the metal surface were treated, where the initial (before EDT) values of tensile σ_x were maximum (where the negative effect of RWS on the mechanical characteristics of the joint is maximum). The EDT conditions and modes for MM specimens are given in Table 7, where the values of the charging voltage and current U_{ch}^{I}, dynamic (impact) U_{ch}^{P} of EDT components and the time period of their action, respectively t_I and t_P.

RESULTS OF EDT ON RWS OF MM SPECIMENS AND THEIR DISCUSSION

The distribution of the RWS σ_x component in the central cross-section of the MM1 (Al) alloy specimen $\delta = 1.0$ mm before and after EDT under the conditions given in Table 7 (line 1) is shown in Figure 4. It can be seen that the treatment has a positive effect on the distribution of σ_x along the fusion lines ($Y = -10$ and 10 mm), where the tensile σ_x values after EDT decrease from 205 to 155 MPa.

The distribution of σ_x RWS in the MM1 (Al) alloy specimen $\delta = 3$ mm before and after EDT under the conditions given in Table 7 (line 2) is shown in Figure 5. It can be seen that after EDT, the initial tensile RWS $\sigma_x = 180$ MPa in the centre of the weld ($Y = 0$) are transformed into compression $\sigma_x = -15$ MPa, and in the base metal along the fusion line ($Y = -5$ and 5 mm), the tensile σ_x values also significantly decrease.

Distribution of the RWS σ_x component in the austenitic MM4 (Fe–Cr–Ni) steel specimen $\delta = 1$ mm before and after EDT under the conditions given in Table 7 (line 3) is shown in Figure 6.

From Figure 6, it can be seen that in the centre of the weld ($Y = 0$), the initial (before EDT) σ_x are compressive, and their values reach –111 MPa. This can be explained by the peculiarity of the structure formation mechanism during the formation of RWS in austenitic steels at rapid cooling of the weld metal. If the structural transformations of the weld metal during cooling occur at low temperatures, its contraction is replaced by a sharp expansion, and the resulting tensile stresses decrease and transfer to compression [19]. The conditions for rapid cooling of the metal were realized during welding of the experimental specimens in the assembly bench (Figure 3, *a*), where inert gas was used to blow the weld. At the same time, in the areas of the base metal near the fusion lines ($Y = -10$ and $Y = 10$ mm), the initial tensile σ_x have the values of 560 and 723 MPa, which after EDT under the conditions of Table 7 (line 3) decrease to 131 and 0 MPa, respectively. At the same time, EDT of the base metal near the fusion line ($Y = -10$ and $Y = 10$ mm) contributes to a decrease in compressive stresses from $\sigma_x = -111$ to –35 MPa in the centre of the weld ($Y = 0$). This can be explained by the redistribution of RWS in the active zone of the welded joint, which is initiated by the relaxation of σ_x near the fusion line.

The EDT of the metal of the MM4 (Fe–Cr–Ni) welded joint specimen $\delta = 3$ mm was performed under the conditions of Table 7 (line 4), taking into account the results obtained for the specimen $\delta = 1$ mm regarding the reduction of compressive stresses in the centre of the weld initiated by the treatment of the fusion lines. EDT was performed along the weld centre and fusion lines. The distribution of RWS σ_x of S-06 steel $\delta = 3$ mm before and after EDT is shown in Figure 7.

From the data in Figure 7, it can be seen that EDT has a positive effect on the distribution of σ_x in the centre of the weld ($Y = 0$). In this zone, the compressive σ_x values grow from –100 to –250 MPa as a result of the EDT. At the same time, EDT also optimizes the distribution of σ_x along the weld metal fusion line ($Y = 10$ and $Y = -10$ mm), where tensile stresses are reduced from 400 to 0–67 MPa. In the areas ($Y = 5$ mm and $Y = -5$ mm), the RWS after EDT transform from tensile to compressive — from 220 to –100 MPa.

The distribution of the σ_x RWS component in the welded joint specimen of MM2 (Ti) alloy $\delta = 1$ mm before and after EDT of the weld metal under the con-

Table 7. Modes and conditions for performing EDT of specimens of welded joints made of MM

№	MM	δ, mm	t_I, μs	t_P, μs	U_{ch}^{P}, V	U_{ch}^{I}, V	Terms of execution of the EDT of MM
1	MM1 (Al)	1.0	275	325	150	300	Along the fusion line (AFL)
2		3.0			300	500	Along the weld centre (AWC)
3	MM4 (Fe–Cr–Ni)	1.0			200	500	AFL
4		3.0			300	500	AFL + AWC
5	MM2 (Ti)	1.0			200	300	AFL
6		3.0			250	500	AWC
7	MM3 (Ni)	1.0			250	300	AWC
8		3.0			300	500	AWC

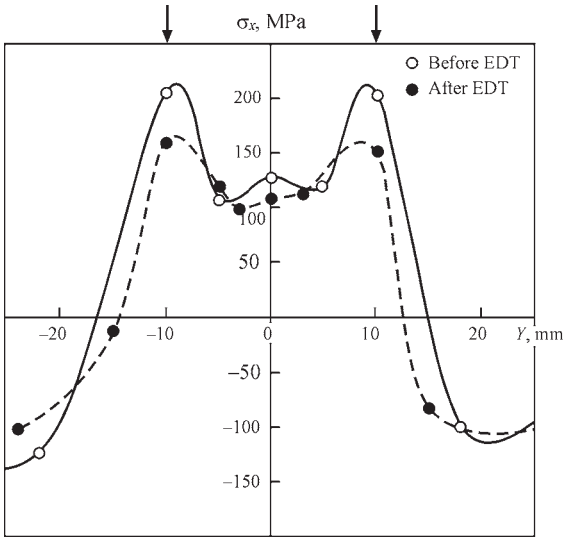

Figure 4. Distribution of the RWS σ_x component in the central cross-section of the MM1 (Al) alloy welded joint specimen δ = 1 mm before and after EDT, where arrows indicate the EDT zones, as in Figures 5–11

ditions of Table 7 (line 5) is shown in Figure 8. It can be seen that EDT reduces the RWS in the centre of the weld (Y = 0) and near the fusion lines (Y = 8 mm and Y = –8 mm), where the values of tensile σ_x after EDT decrease from 200 to 150 MPa and from 270 to 180 MPa, respectively.

The distribution of the RWS σ_x component in the welded joint specimen of MM2 (Ti) alloy δ = 3 mm before and after EDT under the conditions of Table 7 (line 6) of the weld metal is shown in Figure 9. It can be seen that EDT helps to optimize the distribution of RWS in the centre of the weld (Y = 0), where the tensile σ_x after EDT decrease from 200 to 70 MPa. It should be noted that the effect of EDT also extends to σ_x along the fusion line (Y = –8 and Y = 8 mm), where tensile σ_x decrease from 225–240 to 175–180 MPa, respectively.

The distribution of RWS σ_x in the welded joint specimen of nickel MM3 (Ni) alloy δ = 1 mm before

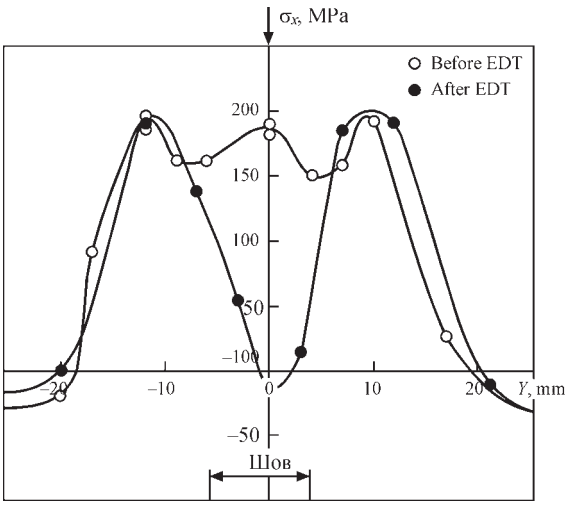

Figure 5. Distribution of the RWS σ_x component in the central cross-section of the MM1 (Al) alloy welded joint specimen δ = 3 mm before and after EDT

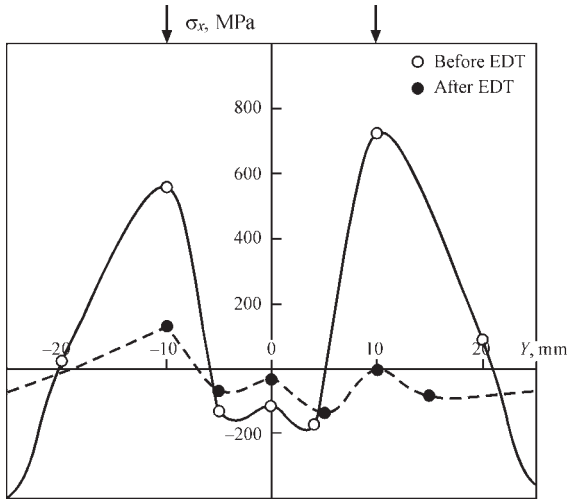

Figure 6. Distribution of the RWS σ_x component in the cross-section of the welded joint specimen made of MM4 (Fe–Cr–Ni) steel δ = 1 mm before and after EDT

and after EDT under the conditions of Table 7 (line 7) is shown in Figure 10, from which it can be concluded that treatment has a significantly lower effect on the distribution of RWS compared to the previous results shown in Figures 4–9. Thus, in the centre of the weld (Y = 0), after EDT, the tensile σ_x decrease from 295 to 263 MPa, and along the fusion lines (Y = –5 and Y = 5 mm) — from 310 to 280 MPa.

The distribution of RWS σ_x in the specimen of MM3 (Ni) alloy δ = 3 mm before and after EDT under the conditions of Table 7 (line 8) is shown in Figure 11. As a result of the studies, it was found that EDT generally has a positive effect on the distribution of RWS in the centre of the weld (Y = 0), where the tensile σ_x after EDT decrease from 305 to 261 MPa.

The summarizing results of evaluating the impact of EDT effectiveness on the control of the RWS σ_x component in the specimens of welded joints made of MM δ = 1 and 3 mm is presented in Table 8. From

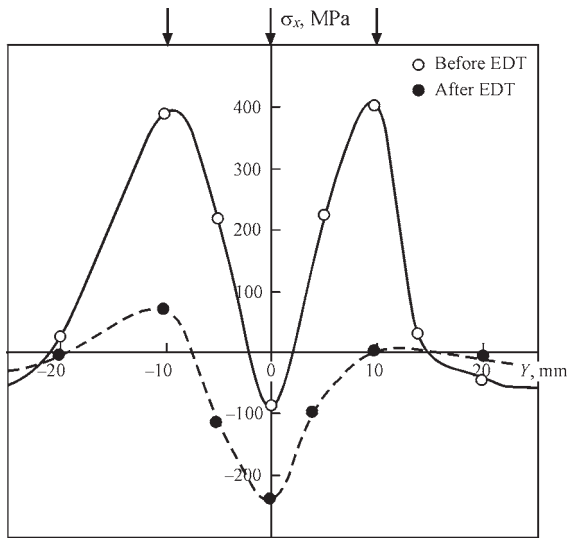

Figure 7. Distribution of RWS σ_x in the cross-section of the welded joint specimen made of MM4 (Fe–Cr–Ni) steel δ = 3 mm before and after EDT

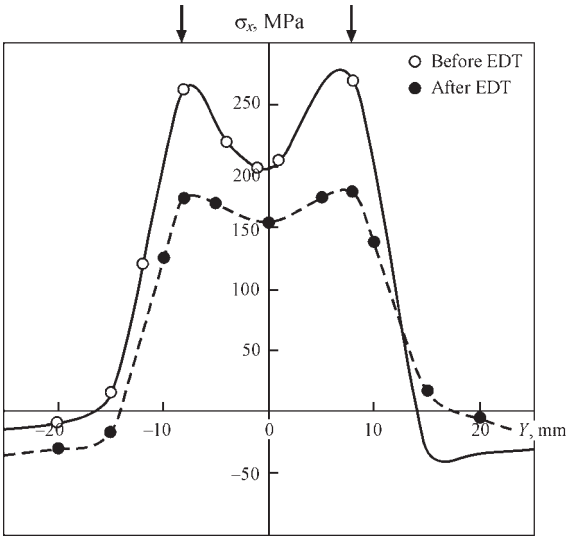

Figure 8. Distribution of the RWS σ_x component in the cross-section of the welded joint specimen of MM2 (Ti) titanium alloy δ = 1 mm before and after EDT

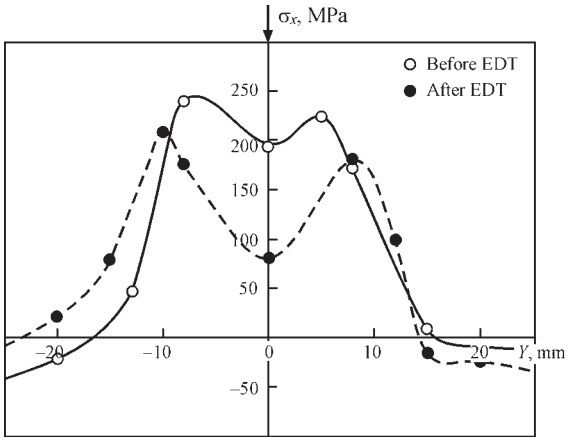

Figure 9. Distribution of the RWS σ_x component in the cross-section of the welded joint specimen of MM2 (Ti) titanium alloy δ = 3 mm before and after EDT

Table 8. EDT effectiveness of welded joints specimens made of MM

No.	MM grade	δ, mm	$\sigma_{x1}{}^*/\sigma_{x2}$, MPa	$(\sigma_{x1} - \sigma_{x2})/\sigma_{x1}$, %
1	MM1 (Al)	1.0	205/150	30
2		3.0	180/–15	>100
3	MM2 (Ti)	1.0	270/180	35
4		3.0	200/70	65
5	MM4 (Fe–Cr–Ni)	1.0	723/0	100
6		3.0	400/0	100
7	MM3 (Ni)	1.0	295/263	11
8		3.0	305/261	15

*σ_{x1} — maximum values of tensile RWS σ_x before EDT; σ_{x2} — after EDT.

the mentioned results, it can be concluded that EDT is an effective mechanism for the control of the residual stress-strain states of welded joints made of Al and Ti alloys with a thickness of 3 mm (lines 2 and 4, respectively) and austenitic steel (lines 5 and 6). At the same time, optimization of EDT modes within the framework

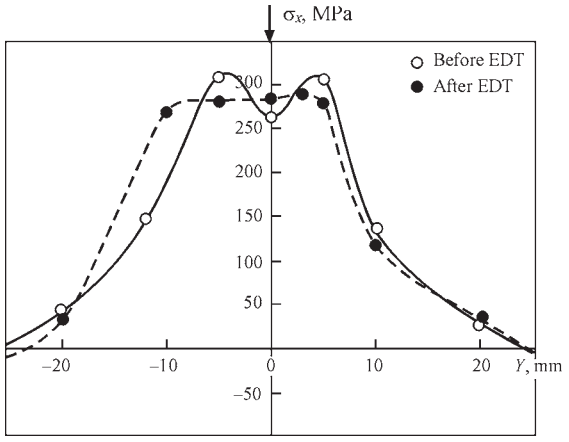

Figure 10. Distribution of the RWS σ_x component in the cross-section of welded joint specimen of nickel MM3 (Ni) alloy δ = 1 mm before and after EDT

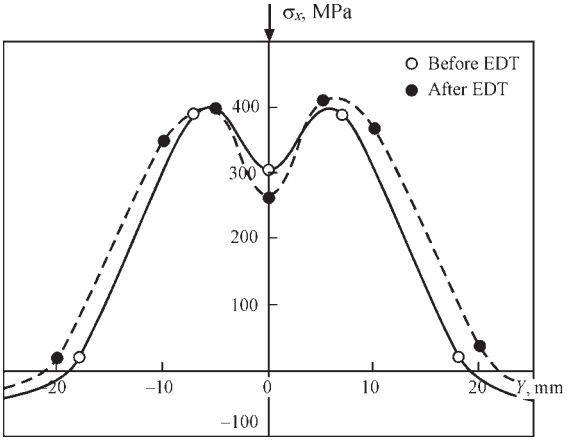

Figure 11. Distribution of the RWS σ_x component in the cross-section of welded joint specimen of MM3 (Ni) alloy δ = 3 mm before and after EDT

of additional studies will increase the effectiveness of the electrodynamic effect for the treatment of welded joints of smaller thicknesses from the supplied materials (with respect to the results presented in lines 1 and 3).

At the same time, the results presented in lines 7 and 8 show that in order to increase the effectiveness of EDT of MM3 (Ni) alloy, it is necessary to use higher values of electrodynamic effect within further studies. It is also advisable to use a new method for the treatment of welded joints made of MM3 (Ni) alloy, based on magnetically pulsed effects on the RWS of welded joints made of non-ferromagnetic MM [2, 3].

Based on the conducted studies, it should be noted that the use of EDT contributes to a reduction in the tensile RWS of thin-sheet welded joints made of the studied MM.

CONCLUSIONS

1. The technology for electrodynamic treatment (EDT) of experimental specimens of thin-sheet butt welded joints made of Al-, Ni- and Ti-based alloys and austenitic steel was developed and implemented.

2. The effect of EDT on the longitudinal σ_x component of residual welding stresses (RWS) of the test specimens was studied using electron speckle interferometry.

3. It was found that EDT provides complete elimination of tensile RWS in welded joints made of Al-based alloy and austenitic steel and reduction in RWS to 65 % from the initial level in Ti-based alloy.

4. It was found that EDT provides a slight decrease in tensile RWS (up to 15 % of the initial level) in welded joints made of Ni-based alloy.

5. Based on the research results, it was found that in order to increase the efficiency of EDT of Ni-based alloy, higher values of electrodynamic action energy or the use of a pulsed magnetic field treatment method are required.

REFERENCES

1. Masubuchi, K. (1980) *Analysis of welded structures*. Oxford, Pergamon Press.
2. Razmyshlyaev, A.D., Ageeva, M.V. (2018) On mechanism of weld metal structure refinement in arc welding under action of magnetic fields (Review). *The Paton Welding J.*, **3**, 25–28. DOI: https://doi.org/10.15407/tpwj2018.03.05
3. Dubodelov, V.I., Goryuk, M.S. (2018) Application of electromagnetic fields and hydrodynamic phenomena to intensify the action on metallic systems: World and Ukrainian experience. In: *Science of Materials: Achievements and Prospects.* Vol. 2, Kyiv, Akademperiodyka, 24–50.
4. Volkogon, V.M., Avramchuk, S.K., Strilets, E.V. (2005) Formation of strengthening coatings under action of powerful electric discharge. In: *Proc. of 5th Int. Sci.-Techn. Conf. on Surface Engineering and Renovation of Products. 21–24 May 2005, Yalta*, 48–51.
5. Conrad, H., Sprecher, A. (1989) *The electroplastic effect in metals*. Ed. by F.R.N. Nabarro. Elsevier Sci. Publs B.V., Dislocations in Solids, 500–529.
6. Baranov, Yu.V., Troitsky, O.A., Avramov, Yu.S. (2001) *Physical principles of electric pulse and electric plastic treatments and new materials.* Moscow, MGIU.
7. Stepanov, G.V., Babutsky, A.I., Mameev, I.A. (2004) Nonstationary stress-strain state in long rod due to the pulse of high density electric current. *Problemy Prochnosti,* **4**, 60–67.
8. Gu, S., Kobayashi, D., Yan et al. (2024) Achieving stress relief in martensitic stainless steel via high-density pulsed electric current treatment. *Metallurgical and Materials Transact. A: Physical Metallurgy and Materials Sci*., 55(**10**), 3859–3868. DOI: https://doi.org/10.1007/s11661-024-07522-5
9. Zhang, X., Xiang, S., Yi, K., Guo, J. (2022) Controlling the residual stress in metallic solids by pulsed electric current. *Acta Metallurgica Sin*. 58(**5**), 581–598, DOI: https://doi.org/10.11900/0412.1961.2021.00367
10. Lobanov, L.M., Pashchin, N.A., Yashchuk, V.A., Mikhodui, O.L. (2015) Effect of electrodynamic treatment on the fracture resistance of the AMg6 aluminum alloy under cyclic loading. *Strength of Materials*, **47**, 447–453. DOI: https://doi.org/10.1007/s11223-015-9676-5
11. Liu, C., Wang, M., Peng, H. et al. (2024) Pulse electric current induced interfacial ductile phase on improving the mechanical properties of the Au20Sn/Cu solder joints. *J. of Materials Sci.: Materials in Electronics*, 35(**18**), 1210. DOI: https://doi.org/10.1007/s10854-024-13002-8
12. Strizhalo, V.A., Novogrudsky, L.S., Vorobiov, E.V. (2008) *Strength of materials at cryogenic temperatures taking into account the action of electromagnetic fields.* Kyiv, IPS.
13. Pashchin, N.A., Zarutsky, A.V. (2016) Influence of electrodynamic treatment of material on fatigue life of specimens with holes. In: *Proc. of Int. Sci.-Techn. Conf. on Problems of Manufacturing and Life Cycle Assurance of Aviation Technique. Kharkiv, 20–21 April 2016* [in Russian].
14. Lobanov, L.M., Pashchin, N.A., Cherkashin, A.V. et al. (2012) Repair welding of intermediate cases of aircraft engines from high-temperature magnesium alloy ML10 with application of electrodynamic treatment. *The Paton Welding J*., **11**, 28–32.
15. Lobanov, L.M., Pashchin, N.A., Loginov, V.P. et al. (2010) Repair of ship hull structures of aluminium alloy AMg6 using electrodynamic treatment. *The Paton Welding J*., **9**, 31–32.
16. Lobanov, L.M., Korzhyk, V.M., Pashchyn, M.O. et al. (2022) Deformation-free TiG welding of AMg6 alloy with application of electrodynamic treatment of weld metal. *The Paton Welding J*., **8**, 3–8. DOI: https://doi.org/10.37434/tpwj2022.08.01
17. Lobanov, L.M., Pashchyn, M.O., Mikhodui, O.L. et al. (2022) Stress-strain state of welded joints of AMg6 alloy after electrodynamic treatment during welding. *Strength of Materials*, 54(**6**), 983–996. DOI: https://doi.org/10.1007/s11223-023-00474-y
18. Lobanov, L.M., Pivtorak, V.A., Savitsky, V.V., Tkachuk, G.I. (2006) Procedure for determination of residual stresses in welded joints and structural elements using electron speckle-interferometry. *The Paton Welding J*., **1**, 24–29.
19. Vinokurov, V.A. (1968) *Welding strains and stresses.* Moscow, Mashinostroenie.

ORCID

L.M. Lobanov: 0000-0001-9296-2335,
M.O. Pashchyn: 0000-0002-2201-5137,
O.L. Mikhodui: 0000-0001-6660-7540

CONFLICT OF INTEREST

The Authors declare no conflict of interest

CORRESPONDING AUTHOR

O.L. Mikhodui
E.O. Paton Electric Welding Institute of the NASU
11 Kazymyr Malevych Str., 03150, Kyiv, Ukraine.
E-mail: olha.mikhodui@gmail.com

SUGGESTED CITATION

L.M. Lobanov, M.O. Pashchyn, O.L. Mikhodui, O.M. Tymoshenko (2025) Electrodynamic treatment for the control of residual stresses in welded joints made of light, heat-resistant alloys and austenitic steel. *The Paton Welding J*., **8**, 37–43.
DOI: https://doi.org/10.37434/tpwj2025.08.04

JOURNAL HOME PAGE

https://patonpublishinghouse.com/eng/journals/tpwj

Received: 15.04.2025
Received in revised form: 19.06.2025
Accepted: 05.08.2025

DOI: https://doi.org/10.37434/tpwj2025.08.05

MODEL OF THE ANODE BOUNDARY LAYER IN WELDING ARCS

I.V. Krivtsun[1], A.I. Momot[1,2], I.B. Denysenko[1,3], U. Reisgen[4], O. Mokrov[4], R. Sharma[4]

[1]E.O. Paton Electric Welding Institute of the NASU
11 Kazymyr Malevych Str., 03150, Kyiv, Ukraine,
[2]Taras Shevchenko National University of Kyiv
64/13 Volodymyrs'ka Str., 01601, Kyiv, Ukraine,
[3]V.N. Karazin Kharkiv National University
4 Svobody Sq., 61022, Kharkiv, Ukraine
[4]Welding and Joining Institute, RWTH Aachen University
49 Pontstrasse, 52062, Germany

ABSTRACT

A one-dimensional model of the anode boundary layer in atmospheric pressure electric arcs with refractory cathode and evaporating anode is proposed for two modes of the anode metal evaporation: diffusive and convective. The corresponding systems of differential and algebraic equations are formulated to compute the spatial distributions of the number densities and diffusive flux densities of electrons, ions, and atoms; the electron temperature and the heavy particle (atoms and ions) temperature; and the electric potential in the plasma of the anode layer. Additionally, the model allows to calculate the heat flux introduced by the arc into the anode. The boundary conditions for the differential equations of this model at the boundaries of the anode layer with the arc column plasma and the space-charge sheath are formulated. An approach for determining the plasma parameters at these boundaries is also proposed for each evaporation mode.

KEYWORDS: anode boundary layer, welding arc, modelling, evaporating anode, metal vapor, diffusive evaporation, convective evaporation

INTRODUCTION

An important feature of welding arcs is the multi-component nature of arc plasma, which is associated with the presence, along with shielding gas particles, of the atoms and ions of metal vapor entering the arc due to evaporation of electrode material or the metal being welded [1–3]. Under TIG/PTA, and hybrid (TIG/PTA + laser) welding conditions, the main source of vapor in the arc is the metal being welded (anode of the arc) [4–6], since evaporation of the material of a refractory cathode operating in a thermionic mode is negligible.

At the same time, even a small amount of evaporated anode metal in the arc plasma of inert (shielding/plasma-forming) gas significantly affects its ionization composition, thermodynamic, transport, and optical properties. This leads to significant changes in thermal, electrical and gas-dynamic characteristics of the arc column plasma and of the anode boundary layer during TIG welding compared to the atmospheric pressure arc discharge with refractory (tungsten) cathode and non-evaporating, e.g. water-cooled anode [7–8].

In TIG/PTA, and hybrid (TIG/PTA + laser) welding, the temperature on the weld pool surface changes in the range from the melting temperature of the metal being welded to the boiling temperature and higher, for example, due to local heating of this surface by focused laser beam under hybrid welding conditions. In this temperature range, metal evaporation from the anode surface may occur both in the diffusive mode and in the convective one [9]. In the diffusive mode of evaporation, which is realized when the vapor pressure of the anode metal is less than the ambient plasma pressure, the evaporated metal particles diffuse into the arc plasma and it becomes multi-component (containing atoms and ions of the shielding/plasma-forming gas and of the anode metal). In the convective mode, the metal vapor pressure is greater than the ambient pressure. Hence, vapor expansion occurs from the anode surface, which displaces the shielding/plasma-forming gas, and the near-anode plasma becomes one-component (containing only atoms and ions of the anode metal).

For both considered evaporation modes, the influence of the anode metal evaporation on the welding arc plasma characteristics, as well as its effect on the metal being welded, is largely determined by the processes occurring in the anode boundary layer. Thus, studying the anode layer of the atmospheric pressure electric arc in the conditions of metal evaporation from the anode surface is an important step toward a deeper understanding of TIG/PTA and hybrid (TIG/PTA + laser) welding and toward a further improvement of the corresponding technologies.

Due to the small dimensions, high temperatures, rapid dynamics, and the difficulty of direct observation, experimental studies of anode phenomena are significantly complicated. Therefore, theoretical investigation and numerical modeling are effective tools for studying and analyzing the physical processes occurring in the anode boundary layer of welding arcs.

Note that the characteristic thickness of the anode layer L_a is usually much less than the size of the weld pool surface. Hence, the variations of plasma parameters inside the anode layer ($0 \le x \le L_a$) perpendicularly to the anode surface are much more rapid than the changes along this surface. It allows us to use the one-dimensional model of the anode boundary layer of arc plasma. We will consider the anode layer outside the region of spatial charge (sheath) ($0 \le x \le L_D$) (see Figure 1), which is formed near the surface of the anode and has a characteristic size of the order of Debye length $L_D \sim 10^{-7}$–10^{-8} m [10–11]. That is, in our model, the plasma of the anode layer is quasi-neutral, but ionization and thermally non-equilibrium (the temperature of electrons is not equal to that of heavy particles $T_e \neq T_h$). In addition, since the electron temperature of the near-anode plasma commonly does not exceed 12 kK [12], we will assume that it is singly ionized (containing only single-charged ions). In the convective mode of the anode metal evaporation, inside the anode boundary layer, the Knudsen layer for evaporated atoms can be distinguished $0 \le x \le L_K$, the thickness of which is of the order of the atom-atom mean free path, which for copper plasma of atmospheric pressure is $\sim 10^{-6}$ m [10]. In the arc column ($x \ge L_a$), the arc plasma is considered to be in ionization and thermal equilibrium.

MAIN EQUATIONS OF ANODE BOUNDARY LAYER MODEL

At first, we introduce main equations describing singly ionized multi-component (metal-gas) plasma, which is not in thermal and ionization equilibrium. The continuity equations are [13]

$$\nabla\left(n_\alpha u + J_\alpha\right) = \omega_\alpha, \tag{1}$$

where α = *e*, *im*, *ig*, *am*, *ag* (for electrons, metal and gas ions and atoms, respectively). Here $\nabla = \frac{d}{dx}$; n_α is the number density of species α; $u = \frac{1}{\rho}\sum_\alpha \rho_\alpha u_\alpha$ is the mass-average plasma velocity, where $\rho_\alpha = m_\alpha n_\alpha$ and u_α are the mass density and average velocity of the α-th plasma component; m_α is the mass of the corresponding particle; $\rho = \sum_\alpha \rho_\alpha$ is the mass density of whole plasma; $J_\alpha = n_\alpha \upsilon_\alpha$ is the diffusive flux density of α component, where υ_α is its diffusive velocity; ω_α is the term describing the variation of the number density of particles of α-kind due to ionization and recombination.

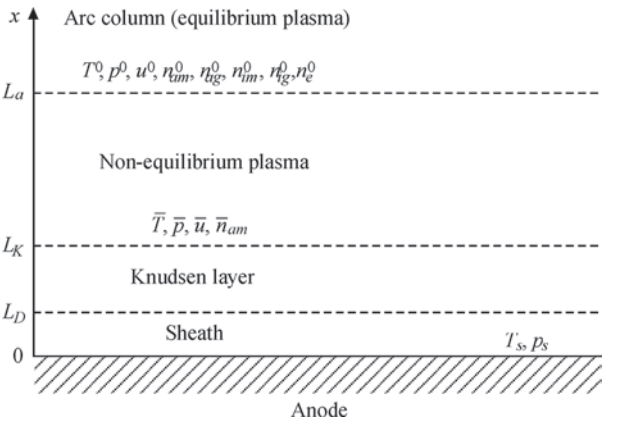

Figure 1. Scheme of the anode boundary layer

In high pressure discharges, the ionization is mainly driven by collisions between electrons and atoms and the dominant recombination mechanism is three-body recombination with an electron as the third body [14]. In this case, the production rates ω_α are written as

$$\begin{aligned} \omega_{im} &= -\omega_{am} = k_{im} n_e n_{am} - k_{rm} n_e^2 n_{im}, \\ \omega_{ig} &= -\omega_{ag} = k_{ig} n_e n_{ag} - k_{rg} n_e^2 n_{ig}, \\ \omega_e &= \omega_{im} + \omega_{ig}, \end{aligned} \tag{2}$$

where $k_{im,g}$ are the ionization rate constants of metal and gas atoms, respectively, and $k_{rm,g}$ are the corresponding recombination rate constants of ions.

The momentum equations are [13]

$$\begin{aligned} &\rho_\alpha u \nabla u + \nabla p_\alpha + z_\alpha e n_\alpha \nabla\varphi = \\ &= \sum_\beta \nu_{\alpha\beta} \mu_{\alpha\beta} n_\alpha n_\beta (\upsilon_\beta - \upsilon_\alpha) - R_\alpha^T. \end{aligned} \tag{3}$$

Here, $p_\alpha = n_\alpha k T_\alpha$ is the partial pressure of the α-th plasma component, where *k* is the Boltzmann constant and T_α is the temperature; z_α is the charge number ($z_e = -1$, $z_{im,ig} = 1$, $z_{am,ag} = 0$); *e* is the elementary charge; φ is the electrostatic potential; $\nu_{\alpha\beta}$ and $m_{\alpha\beta} = m_\alpha m_\beta/(m_\alpha + m_\beta)$ are the collision frequency and reduced mass of α and β species; R_α^T is thermal diffusion force related to the gradient of electron temperature:

$$R_\alpha^T = C_\alpha^{(e)} n_\alpha k \nabla T_e, \quad \sum C_\alpha^{(e)} n_\alpha = 0. \tag{4}$$

Note that the thermal diffusion effect due to the heavy particles' temperature gradient is neglected in equations (4) [15].

The energy equations are [13]

$$\begin{aligned} &\frac{3}{2} u \nabla p_\alpha + \frac{5}{2} p_\alpha \nabla u + m_\alpha J_\alpha u \nabla u + \nabla q_\alpha + z_\alpha e J_\alpha \nabla\varphi = \\ &= -\sum_\beta 3k \nu_{\alpha\beta} \frac{\mu_{\alpha\beta}}{m_\alpha + m_\beta} n_\alpha n_\beta (T_\alpha - T_\beta) - \delta_{\alpha e} w_e, \end{aligned} \tag{5}$$

where δ_{ae} is the Kronecker delta.

The heat fluxes q_α in equations (5) are assumed to be caused by the heat conduction and convection

$$q_\alpha = h_\alpha + \frac{5}{2} J_\alpha k T_\alpha . \tag{6}$$

Here for heavy particles ($\alpha \neq e$) the conductive heat fluxes h_α can be defined without taking into account the effect inverse to the thermal diffusion [15].

$$h_\alpha = -\lambda_\alpha \nabla T_\alpha , \tag{7}$$

where λ_α is the thermal conductivity coefficient of heavy particles species α. For electrons, both mechanisms (heat conduction and thermal diffusion) are taken into account, and the electron heat flux h_e is given by [15]:

$$h_e = -\lambda_e \nabla T_e + k T_e n_e \sum_\beta A_\beta^{(e)} (\upsilon_e - \upsilon_\beta), \tag{8}$$

where λ_e is the electron thermal conductivity; $A_\beta^{(e)}$ are the kinetic coefficients.

The value w_e in equation (5) for electrons describes the energy losses of the electron component of the plasma due to atom ionization and radiation:

$$w_e = U_{im} \omega_{im} + U_{ig} \omega_{ig} + w_{rad} , \tag{9}$$

where U_{im} and U_{ig} are the ionization potentials of the metal and gas atoms, respectively; w_{rad} is the power loss of electrons due to radiation.

The energy equations (5) can be written using the above assumption that the temperatures of all heavy particles are equal: $T_\alpha = T_h (\alpha \neq e)$, but differs from the electron temperature $T_e \neq T_h$ (two-temperature plasma model). In this case, the energy equation for electrons takes the form (neglecting the term with $m_e J_e u \nabla u$ [13] and taking into account the electron continuity equation):

$$\begin{aligned} &\left(n_e u + J_e\right) \frac{5}{2} k \nabla T_e - u \nabla (n_e k T_e) + \nabla h_e - e J_e \nabla \varphi = \\ &= -\kappa_{eh} n_e k (T_e - T_h) - \left(U_{im} + \frac{5}{2} k T_e \right) \omega_{im} - \\ &- \left(U_{ig} + \frac{5}{2} k T_e \right) \omega_{ig} - w_{rad} , \end{aligned} \tag{10}$$

where

$$\kappa_{eh} = 3 \sum_{\beta \neq e} \nu_{e\beta} \frac{m_e}{m_\beta} n_\beta . \tag{11}$$

Summing up equations (5) for plasma heavy particles, the energy equation for heavy particles can be written as:

$$\begin{aligned} &\sum_{\beta \neq e} \left\{ (n_\beta u + J_\beta) \frac{5}{2} k \nabla T_h - u \nabla (n_\beta k T_h) + \right. \\ &\left. + m_\beta J_\beta u \nabla u + z_\beta e J_\beta \nabla \varphi \right\} + \\ &+ \nabla h_h = \kappa_{eh} n_e k (T_e - T_h). \end{aligned} \tag{12}$$

Here

$$h_h = -\lambda_h \nabla T_h , \tag{13}$$

where $\lambda_h = \sum_{\beta \neq e} \lambda_\beta$ is the thermal conductivity of plasma heavy particles.

DIFFUSIVE EVAPORATION OF ANODE METAL

We consider a multi-component singly-ionized plasma of the anode boundary layer of an atmospheric pressure argon arc with a metal anode evaporating in the diffusive mode. The composition of such plasma is described by the number densities: n_e, n_{ig}, n_{im}, n_{ag}, n_{am}. The plasma in the anode layer (beyond the sheath) is quasi-neutral:

$$n_e = n_{ig} + n_{im} \tag{14}$$

and it is assumed to be two-temperature ($T_e \neq T_h$).

Taking into account that atoms and ions of inert gas do not accumulate on the anode metal surface and assuming the total flux of heavy metallic particles (nuclei) from this surface G_m to be approximately equal to zero [16], we can write (relative to the anode surface):

$$\begin{aligned} (n_{ag} + n_{ig}) u + J_{ag} + J_{ig} = 0, \\ (n_{am} + n_{im}) u + J_{am} + J_{im} = G_m \approx 0. \end{aligned} \tag{15}$$

In this case, up to terms of order $m_e / m_{g,m} \ll 1$, where $m_{g,m} = m_{ag,m} \approx m_{ig,m}$, the mass-average plasma velocity $u \approx 0$ and one can consider that plasma in the anode layer is stationary as a whole. As a result, equations (15) yield:

$$J_{ag} = -J_{ig} , \quad J_{am} = -J_{im} . \tag{16}$$

From the expression for the electric current in the plasma $j_0 = e(J_{ig} + J_{im}) - e J_e$ we have:

$$J_e = J_{ig} + J_{im} - j_0 / e . \tag{17}$$

Thus, instead of five continuity equations (1) for diffusive fluxes J_e, J_{ig}, J_{im}, J_{ag}, J_{am}, only two equations can be solved for J_{ig} and J_{im}:

$$\nabla J_{ig} = \omega_{ig} , \quad \nabla J_{im} = \omega_{im} . \tag{18}$$

Other diffusive fluxes are defined with Eqs (16) and (17).

Since the mass-averaged velocity of the near-anode plasma is assumed to be zero in the diffusive mode, then the pressure in the anode layer is constant (equal to atmospheric one). Using equation (14) we obtain

$$p_{atm} = n_{ag}kT_h + n_{ig}k(T_e + T_h) + \\ + n_{am}kT_h + n_{im}k(T_e + T_h). \quad (19)$$

Taking into account that $G_m \approx 0$, let us assume that the metal vapor in the anode layer is saturated and its partial pressure equals the metal vapor saturation pressure p_s at the corresponding surface temperature of the anode T_s, i.e. if $p_s(T_s) \le p_{atm}$, then $T_s \le T_B$, where T_B is the boiling temperature of the anode metal:

$$n_{am}kT_h + n_{im}k(T_e + T_h) = p_s(T_s). \quad (20)$$

Using Eqs (19) and (20), we can express n_{ag} and n_{am} in terms of n_{ig} and n_{im}, obtained as a result of solving equations (18):

$$n_{ag} = \frac{p_{atm} - p_s(T_s)}{kT_h} - n_{ig}\left(1 + \frac{T_e}{T_h}\right), \\ n_{am} = \frac{p_s(T_s)}{kT_h} - n_{im}\left(1 + \frac{T_e}{T_h}\right). \quad (21)$$

If $T_s = T_B$, then $p_s = p_{atm}$ and $n_{ag} = n_{ig} = 0$.

Further we consider the momentum equations (3) for plasma components (under the condition that $u = 0$). Adding the momentum equations for different charged plasma particles (electrons, metal ions and gas ions) to each other using Eqs (16), (17) and accounting for quasi-neutrality condition (14), we get from Eq. (3) that

$$-k(T_e + T_h)\left(\nabla n_{im} + \nabla n_{ig}\right) - \\ -\left(\tilde{C}_{im}^{(e)} n_{im} + \tilde{C}_{ig}^{(e)} n_{ig}\right)k\nabla T_e - \\ -\left(n_{im} + n_{ig}\right)k\nabla T_h + \\ + \alpha_{im}J_{im} + \alpha_{ig}J_{ig} + \alpha_j \frac{j_0}{e} = 0, \quad (22)$$

where

$$\alpha_{im} = -\nu_{eam}\mu_{em}(n_{im} + n_{am} + n_{ig}) - \\ -\nu_{eag}\mu_{eg}n_{ag} - \nu_{imam}\mu_{mm}(n_{im} + n_{am}) - \\ -\nu_{imag}\mu_{mg}n_{ag} - \nu_{igam}\mu_{gm}n_{ig}, \\ \alpha_{ig} = -\nu_{eam}\mu_{em}n_{am} - \nu_{eag}\mu_{eg}(n_{ig} + n_{ag} + n_{im}) - \\ -\nu_{igam}\mu_{gm}n_{am} - \nu_{igag}\mu_{gg}(n_{ig} + n_{ag}) - \nu_{imag}\mu_{mg}n_{im}, \\ \alpha_j = \nu_{eam}\mu_{em}n_{am} + \nu_{eag}\mu_{eg}n_{ag}, \\ \tilde{C}_{im}^{(e)} = 1 + C_e^{(e)} + C_{im}^{(e)}, \quad \tilde{C}_{ig}^{(e)} = 1 + C_e^{(e)} + C_{ig}^{(e)}. \quad (23)$$

As a second equation of the system, we will use the momentum equation (3) for metal atoms. Using the relations $\nabla(n_{ag}kT_h) = -\nabla[n_{ig}k(T_e + T_h)]$ and $\nabla(n_{am}kT_h) = -\nabla[n_{im}k(T_e + T_h)]$ following from Eqs (21), we get

$$k\left(T_e + T_h\right)\nabla n_{im} - \left(C_{am}^{(e)}\frac{p_s}{kT_h} - \tilde{C}_{am}^{(e)}n_{im}\right)k\nabla T_e + \\ + n_{im}k\nabla T_h + \beta_{im}J_{im} + \beta_{ig}J_{ig} + \beta_j\frac{j_0}{e} = 0, \quad (24)$$

where

$$\beta_{im} = \nu_{ame}\mu_{em}(n_{im} + n_{am} + n_{ig}) + \\ + \nu_{amim}\mu_{mm}(n_{im} + n_{am}) + \\ + \nu_{amig}\mu_{mg}n_{ig} + \nu_{amag}\mu_{mg}n_{ag}, \\ \beta_{ig} = \nu_{ame}\mu_{em}n_{am} + \\ + \nu_{amig}\mu_{mg}n_{am} - \nu_{amag}\mu_{mg}n_{am}, \\ \beta_j = -\nu_{eam}\mu_{em}n_{am}, \\ \tilde{C}_{am}^{(e)} = 1 + C_{am}^{(e)}\left(1 + T_e/T_h\right). \quad (25)$$

From Eqs (22) and (24) we can find the expressions for J_{im} and J_{ig} for the two continuity equations (18)

$$J_{im} = \frac{1}{\Delta}\{k(T_e + T_h)\times \\ \times\left[(\beta_{ig} + \alpha_{ig})\nabla n_{im} + \beta_{ig}\nabla n_{ig}\right] + \\ + \left[\beta_{ig}\left(\tilde{C}_{im}^{(e)}n_{im} + \tilde{C}_{ig}^{(e)}n_{ig}\right) - \right. \\ \left. -\alpha_{ig}\left(C_{am}^{(e)}\frac{p_s}{kT_h} - \tilde{C}_{am}^{(e)}n_{im}\right)\right]k\nabla T_e + \\ + \left[(\beta_{ig} + \alpha_{ig})n_{im} + \beta_{ig}n_{ig}\right]k\nabla T_h - \\ -(\beta_{ig}\alpha_j - \alpha_{ig}\beta_j)\frac{j_0}{e}\}; \quad (26)$$

$$J_{ig} = -\frac{1}{\Delta}\{k(T_e + T_h)\times \\ \times\left[\left(\beta_{im} + \alpha_{im}\right)\nabla n_{im} + \beta_{im}\nabla n_{ig}\right] + \\ + \left[\beta_{im}\left(\tilde{C}_{im}^{(e)}n_{im} + \tilde{C}_{ig}^{(e)}n_{ig}\right) - \right. \\ \left. -\alpha_{im}\left(C_{am}^{(e)}\frac{p_s}{kT_h} - \tilde{C}_{am}^{(e)}n_{im}\right)\right]k\nabla T_e + \\ + \left[(\beta_{im} + \alpha_{im})n_{im} + \beta_{im}n_{ig}\right]k\nabla T_h - \\ -\left[\beta_{im}\alpha_j - \alpha_{im}\beta_j\right]\frac{j_0}{e}\}. \quad (27)$$

Here

$$\Delta = \alpha_{im}\beta_{ig} - \alpha_{ig}\beta_{im}. \quad (28)$$

Using the momentum equation (3) for electrons, the expression for determining $\nabla\varphi$ can be written as:

$$\nabla\varphi = \frac{1}{en_e}\left\{kT_e\nabla n_e + \left(1 + C_e^{(e)}\right)n_e k\nabla T_e - \right.$$
$$\left. -\delta_{im}J_{im} - \delta_{ig}J_{ig} - \delta_j\frac{j_0}{e}\right\}, \quad (29)$$

where

$$\delta_{im} = \nu_{eim}\mu_{em}n_{ig} - \nu_{eam}\mu_{em}(n_{im} + n_{am} + n_{ig}) -$$
$$-\nu_{eig}\mu_{eg}n_{ig} - \nu_{eag}\mu_{eg}n_{ag},$$
$$\delta_{ig} = -\nu_{eim}\mu_{em}n_{im} - \nu_{eam}\mu_{em}n_{am} +$$
$$+\nu_{eig}\mu_{eg}n_{im} - \nu_{eag}\mu_{eg}(n_{ig} + n_{ag} + n_{im}), \quad (30)$$
$$\delta_j = \nu_{eim}\mu_{em}n_{im} + \nu_{eam}\mu_{em}n_{am} +$$
$$+\nu_{eig}\mu_{eg}n_{ig} + \nu_{eag}\mu_{eg}n_{ag}.$$

The energy equation for heavy particles, which follows from Eq. (12) with $u = 0$, is

$$\nabla h_h = -e\left(J_{im} + J_{ig}\right)\nabla\varphi + \kappa_{eh}n_e k(T_e - T_h). \quad (31)$$

The energy equation for electrons, which follows from Eq. (10) with $u = 0$, is

$$\nabla\left(\frac{5}{2}kT_eJ_e + h_e\right) = eJ_e\nabla\varphi - \kappa_{eh}n_e k(T_e - T_h) -$$
$$-U_{im}\omega_{im} - U_{ig}\omega_{ig} - w_{rad}, \quad (32)$$

where $J_e = (J_{ig} + J_{im}) - j_0/e$.

Further, we consider the boundary conditions for four Eqs (18), (31) and (32). At the boundary between the anode layer and arc column ($x = L_a$), plasma is assumed to be spatially homogeneous and in both thermal and ionization equilibrium at a temperature T^0 and pressure p_{atm}. The position of the boundary $x = L_a$ is determined from the conditions $\nabla T_e\big|_{L_a} = \nabla T_h\big|_{L_a} = 0$ and $\nabla n_{im}\big|_{L_a} = \nabla n_{ig}\big|_{L_a} = 0$. The boundary conditions for corresponding equations can be written as:

$$T_e\big|_{L_a} = T_h\big|_{L_a} = T^0, \quad (33)$$

$$n_{im}\big|_{L_a} = n_{im}^0, \quad n_{ig}\big|_{L_a} = n_{ig}^0, \quad (34)$$

where n_{im}^0, n_{ig}^0 are determined from the following system of equations consisting of two Saha equations, quasi-neutrality condition and Eqs (21) for equilibrium plasma

$$\frac{n_e^0 n_{im}^0}{n_{am}^0} = S_m(T^0), \quad \frac{n_e^0 n_{ig}^0}{n_{ag}^0} = S_g(T^0),$$
$$n_e^0 = n_{im}^0 + n_{ig}^0, \quad n_{am}^0 = \frac{p_s(T_s)}{kT^0} - 2n_{im}^0, \quad (35)$$
$$n_{ag}^0 = \frac{p_{atm} - p_s(T_s)}{kT^0} - 2n_{ig}^0.$$

Here

$$S_\alpha(T^0) = \left(\frac{2\pi m_e kT^0}{h^2}\right)^{3/2}\frac{2\theta_{i\alpha}}{\theta_{a\alpha}}\exp\left(-\frac{eU_{i\alpha}}{kT^0}\right), \quad (36)$$

where h is the Planck constant; $\theta_{i\alpha} = (2L_{i\alpha} + 1)(2S_{i\alpha} + 1)$ and $\theta_{a\alpha} = (2L_{a\alpha} + 1)(2S_{a\alpha} + 1)$ are the partition functions (statistical weights) of the ion and the atom; $L_{i\alpha,a\alpha}$ and $S_{i\alpha,a\alpha}$ denote the total orbital and spin quantum number, respectively.

The system of equations (35) is a system of nonlinear algebraic equations for five unknowns n_e^0, n_{im}^0, n_{ig}^0, n_{am}^0, n_{ag}^0. The equation for determining T^0 can be written as follows. Since the plasma for $x \geq L_a$ is equilibrium and homogeneous, the energy equations (31) and (32) take the form:

$$-e(J_{im} + J_{ig})\nabla\varphi + \kappa_{eh}n_e k(T_e - T_h) = 0,$$
$$eJ_e\nabla\varphi - \kappa_{eh}n_e k(T_e - T_h) - w_{\text{rad}} = 0. \quad (37)$$

Adding these equations to each other, and accounting for the facts that $e(J_{im} + J_{ig} - J_e) = j_0$ and $j_0 = -\sigma_0\nabla\varphi$, we obtain

$$\frac{j_0^2}{\sigma_0(T^0)} = w_{\text{rad}}(T^0), \quad (38)$$

where $\sigma_0(T_0)$, $w_{rad}(T^0)$ are the electrical conductivity and the power loss due to radiation for a two-component plasma at atmospheric pressure and equilibrium temperature T^0.

In a homogeneous plasma Eqs (26), (27) and (29) take the form

$$J_{im} = -\frac{1}{\Delta}\left[\beta_{ig}\alpha_j - \alpha_{ig}\beta_j\right]\frac{j_0}{e},$$
$$J_{ig} = \frac{1}{\Delta}\left[\beta_{im}\alpha_j - \alpha_{im}\beta_j\right]\frac{j_0}{e}, \quad (39)$$
$$\nabla\varphi = -\frac{1}{en_e}\left[\delta_{im}J_{im} + \delta_{ig}J_{ig} + \delta_j\frac{j_0}{e}\right].$$

It follows (using $j_0 = -\sigma_0\nabla\varphi$):

$$\sigma_0 = \frac{w_1}{-w_2 + w_3 + w_4}, \quad (40)$$

where $w_1 = e^2 n_e^0(\alpha_{im}\beta_{ig} - \alpha_{ig}\beta_{im})$; $w_2 = \delta_{im}(\beta_{ig}\alpha_j - \alpha_{ig}\beta_j)$; $w_3 = \delta_{ig}(\beta_{im}\alpha_j - \alpha_{im}\beta_j)$; $w_4 = \delta_j(\alpha_{im}\beta_{ig} - \alpha_{ig}\beta_{im})$.

Let us now consider the boundary conditions at $x = L_D$, i.e., at the boundary between the quasi-neutral plasma and the space-charge sheath, which at the atmospheric pressure of the near-anode plasma can be considered as collisionless both for electrons and ions [17]. Since the plasma is assumed to be station-

ary near the anode surface ($u = 0$) the temperature of the heavy particles is taken to be equal to the anode surface temperature

$$T_h\big|_{L_D} = T_s. \tag{41}$$

And the boundary condition for the electron temperature at the sheath edge can be written in the form [18]:

$$\left(h_e + \frac{5}{2}kT_eJ_e\right)\Big|_{L_D} = \left(2kT_e + e\varphi_{sh}\right)J_e\big|_{L_D}, \tag{42}$$

where h_e is defined by Eq. (8); φ_{sh} is the plasma potential at the boundary between the quasi-neutral plasma and the space-charge sheath (electric potential of the anode surface is assumed to be equal to zero). The electron diffusive flux density at this boundary is:

$$J_e\big|_{L_D} = -\frac{n_e\upsilon_{Te}}{4}\exp\left(-\frac{e\varphi_{sh}}{kT_e}\right), \quad \upsilon_{Te} = \sqrt{\frac{8kT_e}{\pi m_e}}. \tag{43}$$

Since the sheath is assumed to be collisionless for ions, then ion drift velocities at the boundary $x = L_D$ can be defined as [19, p. 183]:

$$u_{im}\big|_{L_D} = -\upsilon_{Bm}, \quad u_{ig}\big|_{L_D} = -\upsilon_{Bg}, \tag{44}$$

where

$$\upsilon_{Bm} = \sqrt{\frac{k(T_e+T_h)}{m_{im}}}, \quad \upsilon_{Bg} = \sqrt{\frac{k(T_e+T_h)}{m_{ig}}} \tag{45}$$

are the Bohm velocities for metal and gas ions. Thus,

$$J_{im}\big|_{L_D} = -n_{im}\upsilon_{Bm}, \quad J_{ig}\big|_{L_D} = -n_{ig}\upsilon_{Bg}. \tag{46}$$

Hence, Eqs (44)–(46) completely define the boundary conditions at $x = L_D$ for differential equations (18).

Using the condition $j_0 = e(J_{ig} + J_{im}) - eJ_e$ and Eqs (43), (46) we can find

$$\varphi_{sh} = -\frac{kT_e}{e}\ln\frac{4}{\upsilon_{Te}}\left(\frac{j_0}{en_e} + \frac{n_{im}\upsilon_{Bm} + n_{ig}\upsilon_{Bg}}{n_e}\right). \tag{47}$$

It should be noted here that the values of n_e, n_{im}, n_{ig}, T_e, T_h in expressions (43)–(47) are taken at $x = L_D$.

The numerical solution of the system of equations (18), (31) and (32) together with the corresponding boundary conditions allows us to determine the following characteristics of the plasma at the anode layer boundary with the space-charge sheath: n_{im}, n_{ig}, T_e, T_h, as well as the gradients of these quantities at this boundary. The quasi-neutrality condition (14) and relations (21) allow us to find n_e, n_{am} and n_{ag}, while relations (43)–(47) yield the values of J_{im}, J_{ig}, J_e, φ_{sh} at the sheath edge.

This enables computation of the heat flux introduced by the arc into the anode metal, taking into account its evaporation in the diffusive mode. This heat flux can be represented as:

$$q_a = \sum_{k=1}^{6} q_{ak}, \quad (q_{ak} > 0), \tag{48}$$

where

$$q_{a1} = \lambda_e\nabla T_e\big|_{L_D}, \qquad q_{a2} = \lambda_h\nabla T_h\big|_{L_D} \tag{49}$$

are the heat fluxes caused by heat conduction of electrons and heavy particles;

$$q_{a3} = -\left[\left(\frac{5}{2}kT_e - e\varphi_{sh}\right)J_e\big|_{L_D} + kT_e\sum_{\beta\neq e}A_\beta^{(e)}\left(J_e\big|_{L_D} - \frac{n_e}{n_\beta}J_\beta\big|_{L_D}\right)\right] \tag{50}$$

is the electron heat flux caused by convection, where the term $e\varphi_{sh}J_e\big|_{L_D}$ in the right-hand side of the expression (50) describes electron energy loss in the sheath electric field;

$$q_{a4} = -\left[\left(\frac{m_m\upsilon_{Bm}^2}{2} + e\varphi_{sh}\right)J_{im}\big|_{L_D} + \left(\frac{m_g\upsilon_{Bg}^2}{2} + e\varphi_{sh}\right)J_{ig}\big|_{L_D}\right] \tag{51}$$

is the heat flux caused by initial kinetic energy of ions on the sheath edge and their additional acceleration in the electric field of the sheath;

$$q_{a5} = -\left(U_{im}J_{im}\big|_{L_D} + U_{ig}J_{ig}\big|_{L_D}\right), \quad q_{a6} = \frac{j_0}{e}A_f \tag{52}$$

are the heat fluxes caused by the recombination of ions and absorption of electrons at the anode surface, where A_f is the electron work function of the anode metal. Since $J_e\big|_{L_D}$, $J_{im}\big|_{L_D}$, $J_{ig}\big|_{L_D}$ are negative, the minus sign was added in the expressions for q_{a3}, q_{a4}, q_{a5} to ensure that these heat flux components are positive.

CONVECTIVE MODE OF ANODE METAL EVAPORATION

Under the conditions of convective evaporation of an anode metal, the plasma in the anode boundary layer is one-component (contains only metal ions and atoms) and moves at a mass-average velocity u from the surface of the anode. In this case, the quasi-neutrality condition takes the form

$$n_e = n_{im}, \tag{53}$$

Taking into account that $m_eJ_e + m_m(J_{im} + J_{am}) = 0$ [13], up to terms of order $m_e/m_m << 1$ we have

$$J_{im} + J_{am} \approx 0. \tag{54}$$

Then the energy equations for heavy particles (12) and (10) electrons yield

$$\begin{aligned}\left(n_{im}+n_{am}\right)u\nabla\frac{5}{2}kT_h - u\nabla\left[\left(n_{im}+n_{am}\right)kT_h\right] = \\ = -\nabla h_h - eJ_{im}\nabla\varphi + \kappa_{eh}n_{im}k\left(T_e - T_h\right),\end{aligned} \tag{55}$$

$$\begin{aligned}\left(n_{im}u + J_e\right)\nabla\frac{5}{2}kT_e - u\nabla\left(n_{im}kT_e\right) = \\ = -\nabla h_e + eJ_e\nabla\varphi - \kappa_{eh}n_{im}k\left(T_e - T_h\right) - \\ -\left(U_{im} + \frac{5}{2}kT_e\right)\omega_{im} - w_{rad},\end{aligned} \tag{56}$$

where $J_e = J_{im} - j_0/e$.

In the convective mode of the anode metal evaporation we have to solve only one of the continuity equations (1), namely for metal ions

$$\nabla\left(n_{im}u + J_{im}\right) = \omega_{im} = k_{im}n_{im}n_{am} - k_{rm}n_{im}^3. \tag{57}$$

The expression for ion flux density and the expression for determining the electrical potential of a one-component plasma take the form [20]

$$\begin{aligned}J_{im} = \frac{1}{\gamma_e + \gamma_i}\times \\ \times\left\{-k\left(T_e + T_h\right)\frac{n_{am}}{n_{im}+n_{am}}\nabla n_{im} + kT_h\frac{n_{im}}{n_{im}+n_{am}}\nabla n_{am} - \right. \\ \left. -\left(\frac{n_{am}}{n_{im}+n_{am}} + C_e^{(e)} + C_i^{(e)}\right)n_{im}k\nabla T_e + \left(\zeta_e + \zeta_i\right)\frac{j_0}{e}\right\},\end{aligned} \tag{58}$$

$$\begin{aligned}\nabla\varphi = \frac{1}{n_{im}e(\gamma_i + \gamma_e)}\left\{\left[\left(\gamma_e\frac{n_{im}}{n_{im}+n_{am}} + \gamma_i\right)kT_e - \right.\right. \\ \left. -\gamma_e\frac{n_{am}}{n_{im}+n_{am}}kT_h\right]\nabla n_{im} + \gamma_e\frac{n_{im}}{n_{im}+n_{am}}kT_h\nabla n_{am} + \\ +\left[\gamma_e\left(\frac{n_{im}}{n_{im}+n_{am}} - C_i^{(e)}\right) + \gamma_e\left(1 + C_e^{(e)}\right)\right]\times \\ \left.\times n_{im}k\nabla T_e + \left(\gamma_e\zeta_i - \gamma_i\zeta_e\right)\frac{j_0}{e}\right\},\end{aligned} \tag{59}$$

where

$$\begin{aligned}\gamma_e = \nu_{eam}\mu_{em}\left(n_{im}+n_{am}\right), \\ \gamma_i = \nu_{imam}\mu_{mm}\left(n_{im}+n_{am}\right), \\ \zeta_e = \nu_{eim}\mu_{em}n_{im} + \nu_{eam}\mu_{em}n_{am}, \\ \zeta_i = -\nu_{eim}\mu_{em}n_{im}.\end{aligned} \tag{60}$$

Thus, Eqs (55), (56) and (57) present a system of three differential equations of the second order with respect to three unknown functions $T_h(x)$, $T_e(x)$ and $n_{im}(x)$. If we put in these equations $u = 0$, then they become equations for non-convective one-component plasma, which can be found in [10]. The system of Eqs (55), (56) and (57) also includes the parameters $n_{am}(x)$ and $u(x)$, which can be found from the conservation equations for the total particle flux and momentum flux

$$\begin{aligned}\rho(x)u(x) = \text{const} = C_1, \\ p(x) + \rho(x)u(x)^2 = \text{const} = C_2,\end{aligned} \tag{61}$$

where $\rho(x) = m_m(n_{im} + n_{am})$ is the density of the plasma (here it is taken into account that $m_e << m_m$, $m_m = m_{am} \approx m_{im}$), $p(x) = n_{im}k(T_e + T_h) + n_{am}kT_h$ is the pressure.

Further, we will formulate the boundary conditions for a system of differential equations (55), (56) and (57). First, we will consider the boundary conditions at the boundary of the anode layer with the arc column ($x = L_a$), where plasma is considered to be both in ionization and thermal equilibrium ($T^0 = T_e = T_h$), as well as homogeneous.

According to Ref. [9], we will assume that pressure p^0 and velocity u^0 are related by the Rankine–Hugoniot conditions for a shock wave that moves through an external unperturbed gas under conditions of convective evaporation

$$u^0 = \frac{p^0 - p_{atm}}{\sqrt{\frac{\rho_{ext}}{2}\left[p^0(\gamma+1) + p_{atm}(\gamma-1)\right]}}, \tag{62}$$

where p_{atm} is the atmospheric pressure (pressure in the external gas — argon); ρ_{ext} is the density of the external gas for $p = p_{atm}$ and $T_{ext} = 300$ K, $\gamma = 5/3$ is the adiabatic index for a monatomic gas.

To find the composition of plasma at $x = L_a$, we can use the system of equations consisting of Saha equation while taking into account the quasi-neutrality condition, and the partial pressures law for equilibrium plasma

$$\frac{\left(n_{im}^0\right)^2}{n_{am}^0} = S_m(T^0), \quad n_{am}^0 = \frac{p^0}{kT^0} - 2n_{im}^0. \tag{63}$$

The equation for T^0 is Eq. (38)

$$\frac{j_0^2}{\sigma(T^0, p^0)} = w_{rad}(T^0, p^0), \tag{64}$$

where

$$\sigma(T^0, p^0) = e^2 n_i^0\frac{\gamma_e + \gamma_i}{\gamma_i\zeta_e - \gamma_e\zeta_i}. \tag{65}$$

Thus, the plasma parameters n_{am}^0, n_{im}^0, T^0, p^0, u^0 at the boundary $x = L_a$ are determined from the equations (62), (63) and (64), which must be supplemented by

one of the equations (61). Therefore, it is necessary to define one of the constants C_1, C_2.

Next, we need to find the boundary conditions at the other boundary of the anode layer, namely at the boundary with the spatial charge layer $x = L_D$. At low velocity of convective motion of the metallic plasma from the anode surface, compared to the speed of sound, the parameters of the plasma atomic component (density, velocity and temperature) almost do not change within the Knudsen layer [21, 22], so these parameters can be determined for $x = L_K$. The values at this boundary are marked by a dash on top. Since the plasma here is weakly ionized $\overline{n}_{im} \ll \overline{n}_{am}$ [11], ions and electrons do not affect the formation of the Knudsen layer for atoms and the approach to its description proposed in the [9] can be used.

$$\frac{\overline{n}_{am}}{n_s} = \sqrt{\frac{T_s}{\overline{T}_h}}\left[\left(\xi^2 + \frac{1}{2}\right)e^{\xi^2}\,\mathrm{erfc}(\xi) - \frac{\xi}{\sqrt{\pi}}\right] + \\ + \frac{1}{2}\frac{T_s}{\overline{T}_h}\left[1 - \sqrt{\pi}\xi e^{\xi^2}\,\mathrm{erfc}(\xi)\right], \tag{66}$$

$$\frac{\overline{T}_h}{T_s} = \left[\sqrt{1 + \pi\frac{\xi^2}{64}} - \sqrt{\pi}\frac{\xi}{8}\right]^2, \tag{67}$$

where $\overline{n}_{am}$, $\overline{T}_h$ and $\overline{u} = \xi\sqrt{2k\overline{T}_h / m_m}$ are the number density, temperature and velocity of metal atoms at the boundary of the Knudsen layer; n_s is the number density of saturated vapor atoms at the surface temperature of the anode metal T_s.

The conservation equations (61) can be written as

$$\overline{n}_{am}\overline{u} = (n^0_{im} + n^0_{am})u^0, \\ \overline{n}_{am}k\overline{T}_h + m_m\overline{n}_{am}\overline{u}^2 = p^0 + m_m(n^0_{im} + n^0_{am})(u^0)^2. \tag{68}$$

Thus, to determine the six parameters, n^0_{am}, n^0_{im}, T^0, p^0, u^0, $\overline{u}$ we have six equations, respectively: (62), (63), (64), (68). The external parameters are j_0 and T_s. Thus, the boundary conditions for Eqs (55), (56) and (57) at $x = L_a$ have the form

$$T_h\big|_{L_a} = T_e\big|_{L_a} = T^0, \quad n_{im}\big|_{L_a} = n^0_{im}. \tag{69}$$

The temperature of heavy particles at $x = L_K$ is equals to

$$T_h\big|_{L_K} = \overline{T}_h. \tag{70}$$

As stated above, the condition (70) set at $x = L_K$, remains valid at $x = L_D$ and can be used as a boundary condition for Eq. (55).

The boundary condition for Eq. (56) at the boundary of the spatial charge (sheath) is determined by expressions (42) and (43).

Taking into account that in the convective mode of the anode metal evaporation $\overline{u} \neq 0$ and the near-anode plasma pressure $\overline{p} > p_{atm}$ (ion-atom collisions in the sheath become essential), the ion drift velocities at the boundary $x = L_D$ can be defined as [20]

$$u_{im}\big|_{L_D} = \overline{u} + \left.\frac{J_{im}}{n_{im}}\right|_{L_D} = -\overline{\upsilon}_{Bm}. \tag{71}$$

Here $\overline{\upsilon}_{Bm} = \dfrac{\upsilon_{Bm}}{\sqrt{1 + \pi L_D / 2l_{im}}}$ [23], where υ_{Bm} is the Bohm velocity for metal ions (45), l_{im} is the ion-atom mean free path in the sheath. And finally, the boundary condition for Eq. (57) is given by

$$J_{im}\big|_{L_D} = -n_{im}(\overline{u} + \overline{\upsilon}_{Bm}). \tag{72}$$

The value of the potential at the sheath edge takes the form

$$\varphi_{sh} = -\frac{kT_e}{e}\ln\frac{4}{\upsilon_{Te}}\left(\frac{j_0}{en_{im}} + \frac{\upsilon_{Bm}}{\sqrt{1 + \pi L_D / 2\lambda_{im}}} + \overline{u}\right). \tag{73}$$

The numerical solution of the system of equations (55)–(57) together with the corresponding boundary conditions allows determining the heat flux to the anode, which is evaporated in the convective mode. This heat flux can be represented as (48), where q_{a1}, q_{a2}, q_{a3},q_{a6} are given by (49), (50), (52) and

$$q_{a4} = -\left(\frac{m_m\overline{\upsilon}^2_{Bm}}{2} + e\varphi_{sh}\right)J_{im}\big|_{L_D}, \\ q_{a5} = -U_{im}\,J_{im}\big|_{L_D}. \tag{74}$$

Under the conditions of convective evaporation of the anode metal in the energy balance of the anode surface the energy losses of this surface due to evaporation should be taken into account

$$q_{ev} = -\overline{n}_{am}\overline{u}\lambda, \tag{75}$$

where λ is the work function of metal atoms (heat of vaporization per atom).

PLASMA PARAMETERS AT THE ANODE LAYER BOUNDARIES

In this section, some values of plasma parameters, as a function of T_s, $T^0(j_0)$, will be calculated for the three variants of the anode metal: iron, copper and aluminum, the outer (shielding/plasma-forming) gas being argon. The transition from the diffusive to the convective evaporation mode will also be considered.

As mentioned above, the transition from the diffusive to the convective evaporation mode of the anode metal is determined by the surface temperature of the

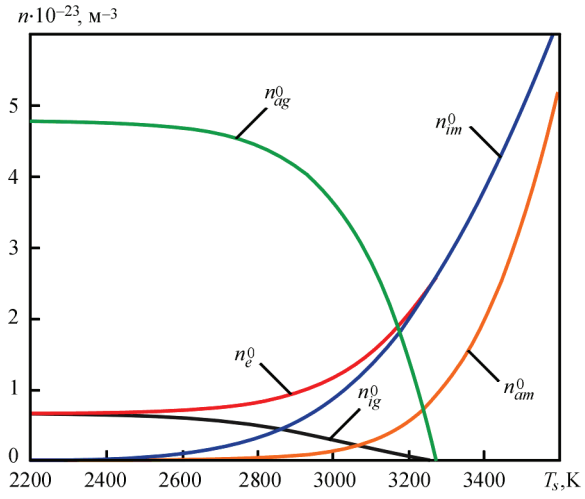

Figure 2. Number density of gas (Ar) atoms n_{ag}^0 (green line) and ions n_{ig}^0 (black line), electrons n_e^0 (red line), iron ions n_{im}^0 (blue line) and atoms n_{am}^0 (orange line) at the anode boundary layer edge vs. the temperature of the anode surface T_s for $T^0 = 12$ kK

anode T_s and the ambient gas pressure p_{ext}. For external pressure equal to the atmospheric one ($p_{ext} = p_{atm}$), the diffusive evaporation mode is realized for $T_s \le T_b$, and convective mode is realized for $T_s > T_b$, where T_b is the boiling point of the anode metal.

In the diffusive mode, the plasma of the anode boundary layer is multicomponent; in addition to particles of shielding/plasma-forming gas, it contains particles of the anode metal. The parameters of this multicomponent equilibrium plasma are defined by Eqs (35). The pressure of saturated vapor p_s, which enters the Eqs (35) is given by the Clapeyron–Clausius law

$$p_s = p_{atm} \exp\left[\frac{\lambda}{k}\left(\frac{1}{T_b} - \frac{1}{T_s}\right)\right]. \qquad (76)$$

Thus, we have a system of five equations (35) for five unknowns $n_{am}^0, n_{ag}^0, n_{im}^0, n_{ig}^0, n_e^0$.

For the convective evaporation mode, the equations for determining the parameters of the plasma at the boundary between the anode layer and the arc column are (62), (63), (64) and (65). Note, that the temperature of the plasma at this boundary T^0 is uniquely determined by the current density j_0 through equations (38) or (64), thus, T^0 can be used as the external parameter in subsequent calculations.

Calculations were performed for the atmospheric pressure argon arc with an iron, copper and aluminum anode under the condition of diffusive and convective evaporation of the metal from the anode surface. The boiling point of Fe was taken equal to $T_b = 3273$ K, the heat of vaporization was taken as 354 kJ/mol [24]. The first ionization potential is equal to 7.9025 eV, the ground states of the iron atom and ion are $^5D_4$ and $^6D_{9/2}$ [25], then $\theta_a = 25$ and $\theta_i = 30$. For Cu anode, $T_b = 2868$ K, the heat of vaporization is 305 kJ/mol, the first ionization potential is 7.726 eV [26]. The ground states of the copper atom and ion are: $^2S_{1/2}$ and $^1S_0$ [25] ($\theta_a = 2$ and $\theta_i = 1$). For Al we have $T_b = 2743$ K, the heat of vaporization is 284 kJ/mol, the first ionization potential is 5.986 eV [26]. The ground states of the aluminum atom and ion are $^2D_{1/2}$ and $^1S_0$ [25] ($\theta_a = 9$ and $\theta_i = 1$).

Figure 2 shows the results of calculations for the iron anode. As can be seen from this figure, when the surface temperature reaches the boiling point of iron T_b, the number density of gas (Ar) atoms and ions decreases to zero and the plasma becomes one-component (contains only Fe atoms and ions), i.e. there is a transition to the convective evaporation mode. In the diffusive mode, both gas and metal ions are present in the plasma, and in the convective mode only metal ions are present, the number density of which is equal to the number density of electrons (the blue and red

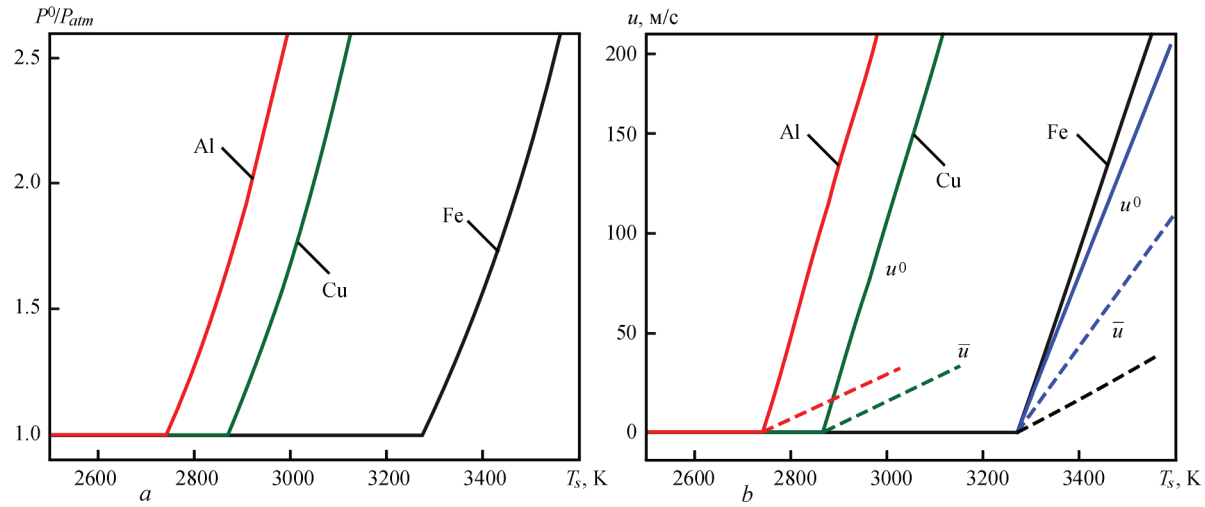

Figure 3. Plasma pressure p^0/p_{atm} (*a*), metal vapor velocity u^0 at the boundary between the anode layer and the arc column (solid lines) and velocity $\bar{u}$ at the boundary of the Knudsen layer (dashed lines) (*b*) vs. the surface temperature of the anode T_s for various anode metals: iron (black lines), copper (green lines) and aluminum (red lines), $T^0 = 12$ kK. Blue lines correspond to the iron anode and $T^0 = 6$ kK

lines in Figure 2 coincide for $T_s > T_b$). As the surface temperature increases, the number density of metal atoms in the plasma becomes higher. For other anode metals, the qualitative behavior of number density dependencies on surface temperature remains the same.

In the convective mode (see Figure 3), the velocity of the metal vapor u^0 becomes greater than zero and the pressure in the arc plasma p^0 becomes higher than the atmospheric pressure; both of these values increase with increasing T_s. The velocity of the metal vapor at the boundary of the Knudsen layer $\overline{a}$ is less than u^0. The velocities u^0 and $\overline{u}$ depend on T_s linearly. As a result of the approximation, we get the following:

$$\text{(Fe, } T_b = 3.273 \text{ kK)}\ u^0(T^0, T_s) = a(T^0)(T_s\,[\text{kK}] - T_b),$$
$$a(T^0) = 514.2 + 17.15T^0\ [\text{kK}];$$
$$\overline{u}\ (T^0, T_s) = \overline{a}\ (T^0)(T_s\,[\text{kK}] - T_b),$$
$$\overline{a}\ (T^0) = 673 - 65.22T^0\ [\text{kK}] + 1.66(T^0\ [\text{kK}])^2;$$
$$\text{(Cu, } T_b = 2.868 \text{ kK)}\ u^0(T^0, T_s) = a(T^0)(T_s\,[\text{kK}] - T_b),$$
$$a(T^0) = 567.7 + 20.52T^0\ [\text{kK}];$$
$$\overline{u}\ (T^0, T_s) = \overline{a}\ (T^0)(T_s\,[\text{kK}] - T_b),$$
$$\overline{a}\ (T^0) = 714.3 - 77.31T^0\ [\text{kK}] + 2.28(T^0\ [\text{kK}])^2;$$
$$\text{(Al, } T_b = 2.743 \text{ kK)}\ u^0(T^0, T_s) = a(T^0)(T_s\,[\text{kK}] - T_b),$$
$$a(T^0) = 577.7 + 38.18T^0\ [\text{kK}] - 1.28(T^0\ [\text{kK}])^2;$$
$$\overline{u}\ (T^0, T_s) = \overline{a}\ (T^0)(T_s\,[\text{kK}] - T_b),$$
$$\overline{a}\ (T^0) = 859.8 - 106.9T^0\ [\text{kK}] + 3.75(T^0\ [\text{kK}])^2.$$

As can be seen from the approximation formulas, as well as from the comparison of the black (Fe, T^0 = 12 kK) and blue (Fe, T^0 = 6 kK) lines in Figure 3, *b*, with increasing T^0, $\overline{u}$ decreases, and u^0 on the contrary increases. The calculations also showed that in the selected range of T_s, $\overline{p} \approx p^0$.

RESULTS AND CONCLUSIONS

A one-dimensional model of the anode boundary layer in welding arcs under TIG/PTA, and hybrid (TIG/PTA + laser) welding conditions (atmospheric pressure inert gas electric arc with refractory cathode and evaporating anode) is formulated for two modes of the anode metal evaporation: the diffusive and convective mode. The model consists of a system of the differential and algebraic equations for calculating the spatial distributions of the number densities of electrons, ions and atoms, their diffusive flux densities, electron temperature, heavy particle (atoms and ions) temperature and electric potential in the plasma of the anode layer. The model also allows calculating the heat flux introduced by the arc into the anode. The boundary conditions for the differential equations of this model at the boundaries of the anode layer with the arc column and the space-charge sheath are determined. An approach is proposed for calculating the near-anode plasma parameters at these boundaries, both in the case of the diffusive evaporation mode of the anode metal and in the convective mode.

For three different anode metals (Fe, Cu, Al), the dependencies of the number densities of plasma particles, pressure and velocity of ionized metal vapor at the anode layer boundaries on the surface temperature of the anode T_s (in the range of 2200 K $\le T_s \le T_b$ + 300 K) are calculated for both diffusive and convective modes of evaporation at fixed value of the arc column plasma temperature T^0 (in the range of 6 kK $\le T^0 \le$ 12 kK).

For the atmospheric pressure argon arc with a refractory cathode and evaporating anode under the condition of its diffusive evaporation ($T_s \le T_b$) the near-anode plasma is multicomponent (Ar + Me). Its mass-average velocity is negligible (up to the diffusive flux of the metal heavy particles G_m [16]). The plasma pressure is equal to the atmospheric pressure, and as the anode surface temperature increases, the number densities of metal atoms and ions in the near-anode plasma also increase. It should be noted that, as it follows from Eq. (76), at $T_s \le T_b \Big/ \left(1 + 4.605\frac{kT_b}{\lambda}\right)$ the fraction of the metal particles in the near-anode plasma is less than 1 % and it can be considered as one-component argon plasma.

It is shown that in the convective mode of the anode metal evaporation ($T_s > T_b$) the velocities u^0 and $-$ linearly depend on T_s, and also depend on the temperature of the arc column T^0. The pressure at the boundary of the Knudsen layer $\overline{p}$ is almost equal to the pressure at the boundary with the arc column p^0 under the considered conditions.

ACKNOWLEDGMENT

The work was funded by the German Research Foundation (DFG) under grant RE2755/78-1. The authors would like to express sincere gratitude for the sponsorship and the support.

REFERENCES

1. Murphy, A.B. (2010) The effects of metal vapour in arc welding. *J. of Physics D: Applied Physics*, **43**, 434001, 91–104. DOI: https://doi.org/10.1088/0022-3727/43/43/434001
2. Schnick, M., Fuessel, U., Hertel, M. et al. (2010) Modelling of gas-metal arc welding taking into account metal vapour. *J. of Physics D: Applied Physics*, **43**, 434008. DOI: https://doi.org/10.1088/0022-3727/43/43/434008
3. Hertel, M., Trautmann, M., Jäckel, S., Füssel, U. (2017) The role of metal vapour in gas metal arc welding and methods of combined experimental and numerical process analysis. *Plasma Chemistry and Plasma Processing*, **37**, 531–547. DOI: https://doi.org/10.1007/s11090-017-9790-1
4. Cho, Y.T., Cho, W.I., Na, S.J. (2011) Numerical analysis of hybrid plasma generated by Nd:YAG laser and gas tungsten arc. *Optics & Laser Technology*, **43**, 711–720. https://doi.org/10.1016/j.optlastec.2010.09.013
5. Tanaka, M., Tsujimura, Y., Yamazaki, K. (2012) Dynamic behaviour of metal vapour in arc plasma during TIG welding.

Welding in the World, **56**, 30-36. DOI: https://doi.org/10.1007/BF03321142
6. Mougenot, J., Gonzalez, J.J., Freton, P., Masquère, M. (2013) Plasma-weld pool interaction in tungsten inert-gas configuration. *J. of Physics D: Applied Physics*, **46**, 135206. DOI: https://doi.org/10.1088/0022-3727/46/13/135206
7. Krivtsun, I., Demchenko, V., Krikent, I. et al. (2015) Distributed and integrated characteristics of the near-anode plasma of the welding arc in TIG and hybrid (TIG+CO_2-laser) welding. *Mathematical Modelling of Weld Phenomena*, **11**, 837–874.
8. Krivtsun, I.V. (2018) Anode processes in welding arcs. *The Paton Welding J*, **11–12**, 91—104. DOI: DOI: http://dx.doi.org/10.15407/tpwj2018.11–12.10
9. Knight, C.J. (1979) Theoretical modeling of rapid surface vaporization with back pressure. *AIAA J.*, **17**, 519–523. DOI: https://doi.org/10.2514/3.61164
10. Krivtsun, I.V., Momot, A.I., Denysenko, I.B. et al. (2024) Transport properties and kinetic coefficients of copper thermal plasmas. *Physics of Plasmas*, **31**, 083505. DOI: https://doi.org/10.1063/5.0216753
11. Krivtsun, I.V., Momot, A.I., Antoniv, D.V., Qin, B. (2023) Characteristics of atmospheric pressure Ar-plasma around a spherical particle: Numerical study. *Physics of Plasmas*, **30**, 043513. DOI: https://doi.org/10.1063/5.0141015
12. Heberlein, J., Mentel, J., Pfender, E. (2009) The anode region of electric arcs: a survey. *J. of Physics D: Applied Physics*, **43**, 023001. DOI: https://doi.org/10.1088/0022-3727/43/2/023001
13. Zhdanov, V.M. (2002) *Transport processes in multicomponent plasma*. CRC Press.
14. Almeida, N.A., Benilov, M.S., Naidis, G.V. (2008) Unified modelling of near-cathode plasma layers in high-pressure arc discharges. *J. of Physics D: Applied Physics* **41**, 245201. DOI: https://doi.org/10.1088/0022-3727/41/24/245201
15. Semenov, I.L., Krivtsun, I.V., Reisgen, U. (2016) Numerical study of the anode boundary layer in atmospheric pressure arc discharges. *J. of Physics D: Applied Physics*, **49**, 105204. DOI: https://doi.org/10.1088/0022-3727/49/10/105204
16. Krikent, I.V., Krivtsun, I.V., Demchenko, V.F. (2014) Simulation of electric arc with refractory cathode and evaporating anode, *The Paton Welding J.*, **9**, 17–24. DOI: https://doi.org/10.15407/tpwj2014.09.02
17. Benilov, M.S., Marotta, A. (1995) A model of the cathode region of atmospheric pressure arcs. *J. of Physics D: Applied Physics*, **28**, 1869. DOI: https://doi.org/10.1088/0022-3727/28/9/015
18. Gao, S., Momot, A., Krivtsun, I. et al. (2025) Interaction between a spherical particle and atmospheric pressure current-less argon plasma. *East European J. of Physics*, 388–395. DOI: https://doi.org/10.26565/2312-4334-2025-1-48
19. Lieberman, M.A., Lichtenberg, A.J. (1994) *Principles of plasma discharges and materials processing*. Wiley.
20. Krivtsun, I.V., Momot, A.I., Denysenko, I.B. (2025) Model of the anode layer of an electric arc with an evaporating anode, *Avtomatyche Zvaryuvannya*, **3**, 3–9.
21. Frezzotti, A. (2007) A numerical investigation of the steady evaporation of a polyatomic gas. *European J. of Mechanics-B/Fluids*, **26**, 93–104. DOI: https://doi.org/10.1016/j.euromechflu.2006.03.007
22. Bird, E., Liang, Z. (2019) Transport phenomena in the Knudsen layer near an evaporating surface. *Physical Review E*, **100**, 043108. DOI: https://doi.org/10.1103/PhysRevE.100.043108
23. Godyak, V.A., Sternberg, N. (2002) Smooth plasma-sheath transition in a hydrodynamic model. *IEEE Transact. on Plasma Sci.*, **18**, 159–168. DOI: https://doi.org/10.1109/27.45519
24. Zhang, Y., Evans, J.R., Yang, S. (2011) Corrected values for boiling points and enthalpies of vaporization of elements in handbooks. *J. of Chemical & Engineering Data*, **56**, 328–337. DOI: https://doi.org/10.1021/je1011086
25. Kramida, A., Ralchenko, Yu., Reader, J., NIST ASD Team (2024) *NIST Atomic Spectra Database* (ver. 5.12), Online. https://physics.nist.gov/asd National Institute of Standards and Technology, Gaithersburg, MD. DOI: https://doi.org/10.18434/T4W30F
26. Loock, H.P., Beaty, L.M., Simard, B. (1999) Reassessment of the first ionization potentials of copper, silver, and gold. *Physical Review A*, **59**, 873. https://doi.org/10.1103/PhysRevA.59.873

ORCID
I.V. Krivtsun: 0000-0001-9818-3383,
A.I. Momot: 0000-0001-8162-0161,
I.B. Denysenko: 0000-0001-7343-086X,
U. Reisgen: 0000-0003-4920-2351,
O. Mokrov: 0000-0002-9380-6905,
R. Sharma: 0000-0002-6976-4530

CONFLICT OF INTEREST
The Authors declare no conflict of interest

CORRESPONDING AUTHOR
A.I. Momot
E.O. Paton Electric Welding Institute of the NASU
11 Kazymyr Malevych Str., 03150, Kyiv, Ukraine.
E-mail: momot.andriy@gmail.com

SUGGESTED CITATION
I.V. Krivtsun, A.I. Momot, I.B. Denysenko, U. Reisgen, O. Mokrov, R. Sharma (2025) Model of the anode boundary layer in welding arcs. *The Paton Welding J.*, **8**, 44–54.
DOI: https://doi.org/10.37434/tpwj2025.08.05

JOURNAL HOME PAGE
https://patonpublishinghouse.com/eng/journals/tpwj

Received: 12.05.2025
Received in revised form: 17.06.2025
Accepted: 24.07.2025

DOI: https://doi.org/10.37434/tpwj2025.08.06

COMPUTER SOFTWARE FOR MODELING A CIRCUMFERENTIAL WELDED JOINT

L.M. Lobanov, O.V. Makhnenko, O.S. Milenin, O.A. Velykoivanenko, G.P. Rozynka, N.R. Basystuk, G.Yu. Saprykina

E.O. Paton Electric Welding Institute of the NASU
11 Kazymyr Malevych Str., 03150, Kyiv, Ukraine

ABSTRACT

The specialized software "Girth Weld" is developed by specialists of the PWI and allows for typical cases of welded girth joints of pipelines and cylindrical pressure vessels to predict the mechanical properties of the weld metal and the heat-affected zone (HAZ), residual stresses and distortions, to determine the redistribution of the stress-strain state as a result of postweld heat treatment, operational and test loading, to assess the structure integrity and service life of welded structures with discontinuity defects that are detected by non-destructive testing or are postulated. The use of this software does not require special knowledge in the calculation methods due to the full automation of the processes of creating a mathematical model of a multipass girth welded joint, dividing the area into finite elements, searching for a solution and visualizing the results. At the same time, high accuracy of predictive results is ensured with limited requirements for computer and time resources through the use of modern approaches to modeling physical and chemical processes during welding and effective algorithms for solving nonlinear problems and systems of high-order differential equations.

KEYWORDS: girth welded joint, multipass welding, software, mathematical modeling, finite element method, mechanical properties, residual stresses, distortions, postweld heat treatment, operational loads, defect acceptability

INTRODUCTION

With the development of computer technology, methods for solving problems of thermoviscoplastic analysis and modeling changes in the material of the welded joint during welding heating, computational simulation and mathematical modeling of welding processes are widely used in industry. However, the issue of accessibility of such an approach for a user with limited access to commercial FEM software packages such as SYSWELD, SIMUFACT, ABAQUS, ANSYS, etc. is relevant. To solve this problem, a problem-oriented specialized software "Girth Weld" was created, which is included in the "Weldprediction" software package, for mathematical modeling of the stress-strain state and mechanical properties in the zone of a butt circumferential (girth) joint produced by multipass arc welding, oriented for engineering and scientific application, which does not require the user to have knowledge in the calculation methods.

The computer program "Girth Weld" allows in the typical cases of circumferential welded joints of pipelines and cylindrical pressure vessels to obtain information on the mechanical properties of the weld metal and the HAZ, residual technological stresses and distortions, to determine the redistribution of the stress-strain state as a result of postweld heat treatment (PWHT), the influence of operational and test loads, and to predict the structural integrity and service life of welded structures with discontinuity defects that are detected by non-destructive testing or are postulated.

The software "Girth Weld" was developed at the PWI. Its implementation is based on many years of experience in mathematical modeling of physical and chemical processes during welding, cladding, PWHT and related technologies, as well as modern achievements in numerical methods, mechanics of deformed bodies and fracture mechanics. At the same time, the developed specialized software has the following advantages:

- high accuracy of predicted results with limited requirements for computer and time resources (personal computer and relatively short calculation time) due to the use of modern approaches to modeling physical and chemical processes in welding [1, 2, 3, 10, 11] and effective algorithms for solving nonlinear problems and systems of high-order differential equations [4, 5];
- reduced labor intensity due to a simple data entry interface and automation of the processes of creating a mathematical model, forming a finite element mesh, finding a solution and visualizing the results;
- accessibility in use, since an engineer or welding technologist can work with the computer program without having special knowledge in the numerical methods for solving mathematical problems.

GENERAL DESCRIPTION AND PURPOSE OF THE COMPUTER PROGRAM

The specialized software "Girth Weld" is a problem-oriented software product for numerical FEM analysis of the technological and physical and mechanical process-

es during multipass welding of circumferential joints of pipeline elements and cylindrical pressure vessels. The computer program is intended for solving typical tasks of expert assessment of technological strength of critical structures when planning assembly or repair welding and PWHT of girth joints, as well as prediction of short-term and long-term static strength during further operation of the welded structure, taking into account both its residual post-weld state and the acting external operational loads.

The software "Girth Weld" is recommended for use in the energy, transport, aerospace and other industries in the design, optimization of assembly welding and planning of repair work of critical pipeline elements and pressure vessels with circumferential welded joints. This software is also recommended for use in expert assessment of structural integrity and service life of welded structures, taking into account both their predicted state and operating conditions, as well as the discontinuity defects (cracks, nonmetallic inclusions, local thinning, gas pores) detected during technical diagnostics.

The use of specialized software "Girth Weld" allows solving the following problems:

- prediction of the optimal arrangement of weld passes in multipass welding depending on the technical conditions of the process and welding optimization criteria;
- determination of the kinetics of the temperature field during multipass welding of circumferential joints of pipeline elements and cylindrical pressure vessels taking into account the technological parameters of the welding process, geometric features of a design, type and properties of the material depending on the chemical composition and temperature;
- numerical assessment of the specifics of the formation of the penetration zone along the thickness of the structural element;
- prediction of transient and residual properties, as well as microstructural phase composition of the weld metal and the HAZ depending on the process and welding conditions, base and filler materials, and the temperature cycles during welding;
- prediction of the kinetics of the distribution of elastic-plastic strains in the process of multipass welding of the butt circumferential joint until the structural element is completely cooled and of the subsequent operational internal pressure and temperature;
- calculation of the residual distortions of the structure as a result of uneven welding heating by assessing irreversible shrinkage phenomena in the welded joint area;
- numerical assessment of the kinetics of accumulation of plastic strains, which is an important characteristic of the susceptibility of the weld metal to hot cracking.

The user interface of the software "Girth Weld" implements a dialog mode for numerical analysis and provides the following options for displaying on the screen and saving as files or hard copies the following results of numerical experiments:

- optimal calculation schemes for the arrangement of weld passes in the groove of a circumferential joint;
- two-dimensional distributions of calculated values (maximum temperatures, melting zone, stresses, plastic strains, distortions) both in the form of drawings and tables;
- distribution of microstructural phase components and mechanical properties of the material in the weld area taking into account the influence of local heating in the process of multipass welding with given heat input parameters;
- tendency to the formation of cold and hot cracks;
- distortions of the structure after welding, taking into account irreversible welding shrinkage strains;
- relaxation of the residual stresses due to PWHT;
- redistribution of the residual stresses under loading conditions (temperature and internal pressure);
- assessment of fatigue fracture resistance of a circumferential welded joint under cyclic loading conditions;
- probabilistic assessment of the serviceability of a cylindrical structure in the presence of macroscopic defects of weld metal discontinuity.

METHODS OF NUMERICAL AND SOFTWARE IMPLEMENTATION OF COMPUTER PROGRAM ALGORITHMS

Development a mathematical model for simulation of the welding processes depends on the purpose of simulation. For prediction of temperature cycles, microstructure phase volume fractions, distortions and residual stresses in a multipass welded joint, the finite element models of volume heat source and nonisothermal deformation of material associated with von Mises yield stress condition are usually used [1, 2]. Modeling is based on tracking the kinetics of formation and development of plastic strains and stresses in a weldment during heating and cooling of each weld pass. Microstructural phase transformations, which induce volume effects and changes of physical and mechanical properties of material in the weld zone, are taken into account.

In the general form in a cylindrical system of coordinates r, β, z (Figure 1, *a*) for multipass circumferential (girth) welding during motion of the volume heat source center $r_0(t)$, $\beta_0(t)$, $z_0(t)$ in time (Figure 1, *b*) the heat flux equation at point (r, β, z) at time t can be written as follows

$$W(r, \beta, z, t) = \\ = W_0(t) \exp\left[-K_r(r-r_0)^2 - K_\beta(\beta-\beta_0)^2 - K_z(z-z_0)^2\right], \quad (1)$$

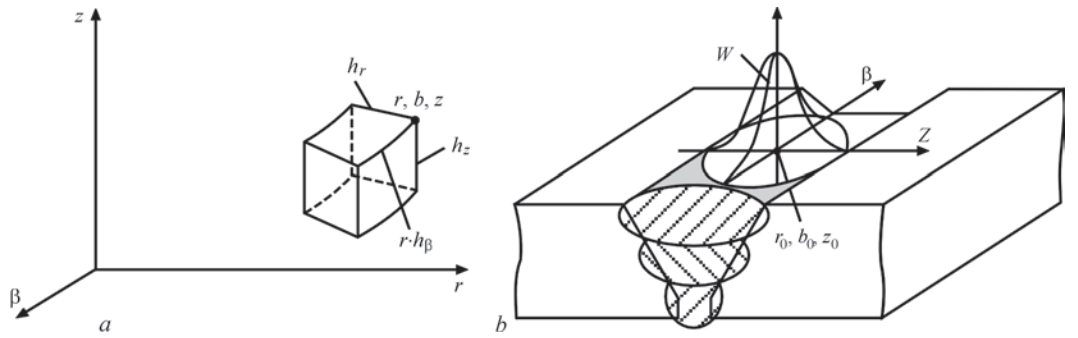

Figure 1. Scheme of finite volume element in cylindrical system of coordinates (r, β, z) (a) and distribution of heating power W(r, β, z, t) at multipass welding (b)

where $W_0(t)$ is the heating power at point (r_0, β_0, z_0); K_r, K_β, K_z are the coefficients of heating power concentration in the directions r, β, z. Between K_r, K_β, K_z and corresponding dimensions d_r, d_β, d_z of effective heating "spot" there is a relation $K_j \frac{d_j^2}{4} = 3.0$, i.e. $d_j = \frac{3.46}{\sqrt{K_j}}$. $W_0(t)$ can be expressed in terms of the effective heating power $q_{ef}(t)$, by integrating the equation (1) in coordinates r, β, z within the heated elements of welded joint. For example, if the heat source moves along the surface of the butt welded joint (Figure 1, b), then:

$$W_0(t) = \frac{2q_{\text{ef}}(t)\sqrt{K_x \cdot K_y \cdot K_z}}{\pi\sqrt{\pi}}. \quad (2)$$

With quite reasonable values K_r, K_β, K_z accurate results can be obtained for temperature distributions near the fusion zone (FZ) of welded elements, which is important from the point of view of microstructural phase changes, mechanical properties, etc.

The mathematical formulation of the problem of heat propagation in a thermally conducting body for the heat sources $W(r, z, \beta, t)$ and the relevant conditions of heat exchange with the environment with a temperature T_c by Newton's law may be presented in the form:

$$-\lambda \frac{\partial T}{\partial n} = \alpha_T (T - T_c), \quad (3)$$

where λ is the coefficient of thermal conductivity of the material at a temperature T, and α_T is the heat transfer coefficient of the surface are well known. [3]

In accordance with [9] we need to add to conditions (3) the initial condition at time $t = 0$ and the differential equation of heat conduction in the system of coordinates (r, β, z):

$$\frac{\partial}{\partial r}\left(r\lambda\frac{\partial T}{\partial r}\right) + \frac{\partial}{r\partial\beta}\left(\lambda\frac{\partial T}{\partial y}\right) + \frac{\partial}{\partial z}\left(r\lambda\frac{\partial T}{\partial z}\right) + W(r,\beta,z,t) = c\gamma\frac{\partial T}{\partial t}r; \quad (4)$$

$$T(r, \beta, z, t = 0) = T_0, \quad (5)$$

where $c\gamma$ is the volumetric heat capacity of the material at temperature T.

Volume effects caused by the change of temperature field are conventionally divided into the temperature effects and effects, caused by microstructural phase transformations [5]. Temperature volume effects at any point

$$\varphi = \alpha(T)(T - T_0), \quad (6)$$

where φ is the function of thermal expansions; $\alpha(T)$ is the coefficient of relative thermal elongation; $(T - T_0)$ is the temperature range.

When welding steels prone to quenching, the microstructural composition at any point in the FZ and HAZ is determined at time t by the values of the relative content of the j-th phase $V_j(T, t)$, $j = a$ corresponds to austenite, $j = m$ — martensite, $j = f$ — ferrite, $j = b$ — bainite, $j = fp$ — ferrite-pearlite mixture. In this case $\sum_j V_j(t) \equiv 1$. Volume effects at any point (r, β, z) due to microstructural phase transformations in the temperature range ($T_0 - T$) [5] are as follows:

$$3\varphi = \frac{\sum V_j(T,t)\gamma_j(T) - \sum V_j(T_0)\gamma_j(T_0)}{\sum V_j(T_0)\gamma_j(T_0)}, \quad (7)$$

where $\gamma_j(T)$ is the the volume of a unit mass of the j-th phase at temperature T. According to [6] for the structural steels:

$$\begin{aligned}
\gamma_m(T) &= 0.12282 + 8.56\cdot10^{-6}T + \\
&+2.15\cdot10^{-3}C, (\text{cm}^3/\text{g}); \\
\gamma_a(T) &= 0.12708 + 4.448\cdot10^{-6}T + \\
&+2.79\cdot10^{-3}C, (\text{cm}^3/\text{g}); \\
\gamma_{b,fp}(T) &= 0.12708 + \\
&+5.528\cdot10^{-6}T, (\text{cm}^3/\text{g}).
\end{aligned} \quad (8)$$

The yield stress of the finite volume material at temperature T considering the microstructural phase changes is calculated as:

$$\sigma_T(T) = \sum \sigma_j(T) V_j(T), \quad (j = a, f, fp, b, m)$$
$$\sigma_T^j(T) = \sigma_T^j(20) \cdot f_j(T), \tag{9}$$

where $\sigma_j(T)$ is the yield stress of the corresponding j-th phase of the microstructure at temperature T; C is the chemical content of carbon (% by weight).

High temperature gradient during welding and a strong irregularity in the distribution of function $\varphi(r, \beta, z, t)$ cause the appearance of both the elastic and inelastic strains. According to [5] a common strain tensor $\varepsilon_{ij}(r, \beta, z, t)$ is a sum of three tensors:

$$\varepsilon_{ij} = \varepsilon_{ij}^e + \varepsilon_{ij}^p + \varepsilon_{ij}^c, \tag{10}$$

where index e is the structural corresponds to the elastic strain; p is the instantaneous strain of plasticity; c is the strain of diffusion plasticity or creep.

Plastic strains are related to the stressed state by the equation of the theory of plastic nonisothermal flow and the associated von Mises yield condition:

$$d\varepsilon_{ij}^p = d\lambda(\sigma_{ij} - \delta_{ij}\sigma), \quad i, j = r, \beta, z, \tag{11}$$

where $d\varepsilon_{ij}^p$ is the tensor increment, which at a given time t is determined by the deformation history, stresses σ_{ij} and temperature T; $d\lambda$ is the scalar function determined by the flow conditions:

$d\lambda = 0$, if $f = \sigma_i^2 - \sigma_T^2(T) < 0$
or $f = 0$ and $df < 0$;
$d\lambda > 0$, if $f = 0$ and $df > 0$;
state $f > 0$ unacceptable,

σ_i is the stress intensity; $\sigma_T(T)$ is the yield stress of the material at temperature T.

For creep strains $_{ij}$, the constraint equation is used in the form:

$$d\varepsilon_{ij}^p = \Omega(T, \sigma_i)(\sigma_{ij} - \delta_{ij}\sigma)dt, \tag{12}$$

where $\Omega(\sigma_i, T)$ is the scalar creep function of the material at temperature T and the stress level, which is determined by the stress intensity σ_i.

For PWHT when it is most important to take into account creep strains, since the stress relaxation process significantly depends on creep, the function $\Omega(\sigma_i, T)$ is rationally chosen on the basis of experiments on deformation of samples from this material at elevated temperatures. The creep function in the general form depending on the material temperature can be approximated by a typical equation [1, 10]:

$$\Omega(T, \sigma_i) = A \cdot \sigma_i^n \cdot \exp\left(\frac{G}{T + 273}\right), \tag{13}$$

where A, G, n are the constants related to material properties.

The presented model of creep at elevated temperatures is quite general and allows to trace deformation processes during PWHT not only during holding at maximum temperature, but also during heating and cooling at temperatures of 550 °C and above, for example, for structural steels. This model can be effective in modeling the relaxation processes of residual stresses during local heat treatment of welded structures or in the case of overall furnace heat treatment for a short holding time, when uniform heating to a given maximum holding temperature is not ensured throughout the volume of the welded joint or structure.

The finite increment of the strain tensor $\Delta\varepsilon_{ij}$ in the time range from $(t - \Delta t)$ to t, where Δt is the step of tracking, is small enough:

$$\Delta\varepsilon_{ij} = \psi\left(\sigma_{ij} - \delta_{ij}\sigma\right) + \delta_{ij}\left(K\sigma + \varphi\right) - b_{ij},$$
$$\left(i, j = r, \hat{a}, z\right);$$
$$\psi = \frac{1}{2G} + \Delta\lambda + \Delta t \cdot \Omega\left(T, \sigma_i\right); \tag{14}$$
$$b_{ij} = \left[\frac{\sigma_{ij} - \delta_{ij}\sigma}{2G} + \delta_{ij}\left(K\sigma\right)\right]_{t-\Delta y} - \delta_{ij}\Delta\varphi.$$

where σ_{ij} is the stress tensor; σ is the average pressure; δ_{ij} is the unit tensor; bulk modulus $K = \frac{1-2\nu}{E}$; shear modulus $G = \frac{E}{2(1+\nu)}$; E is the Young's modulus; ν is the Poisson's ratio.

The equation (14) contains the function ψ, which is determined by the plastic flow condition (11) and the development of creep strains (12). This function significantly depends on the initial solution for the moment t and its determination requires certain approaches. The simplest approach is based on the use of the solution for the moment $(t - \Delta t)$. By reducing the step Δt, it is possible to significantly reduce the errors associated with the risk of obtaining unacceptable states (11), however, during welding heating, such a risk is very significant, therefore approaches based on the construction of appropriate iterative processes are used to determine the physical nonlinearity associated with $\Delta\lambda$ and $\Omega(T, \sigma_i)$.

The following iterative process has been well tested in practice:

$$\psi^{(n+1)} = \left[\frac{1}{2G} + \Delta t \cdot \Omega\left(T, \sigma_i^{(n-1)}\right)\right](1 - p) + p\psi^{(n)},$$
$$\text{if } \sigma_i^{(n)} - \sigma_T\left(T, \sigma_i^{(n)}\right) < -m;$$
$$\psi^{(n+1)} = \psi^{(n)}, \text{ if } -m < \sigma_i^{(n)} - \sigma_T\left(T, \sigma_i^{(n)}\right) < m; \tag{15}$$
$$\psi^{(n+1)} = \psi^{(n)} \frac{\sigma_i^{(n)}}{\sigma_T\left(T, \sigma_i^{(n)}\right)}, \text{ if } \sigma_i^{(n)} - \sigma_T\left(T, \sigma_i^{(n)}\right) > m.$$

Process (15) is stopped if:

$$\left|\psi^{(n+1)}/\psi^{(n)}-1\right|<\delta, \qquad (16)$$

where n, $n+1$ are the iteration numbers, $0 \le p < 1$, $m << \sigma_T\left(T,\sigma_i^{(n)}\right)$, $\delta \le 1$ are the iterative process parameters.

After the linearization procedure the structure of the equation of continuity (14) formally corresponds to the equation of continuity of the theory of elasticity with variable parameters of elasticity (ψ instead of $1/2G$) and additional strains b_{ij}, the value of which is known according to the solution in the previous step of tracking ($t - \Delta t$) and the temperature distributions at moments t and ($t - \Delta t$).

Since in most typical cases of welding and operation of pipeline elements and cylindrical pressure vessels, the distribution of stresses and strains is characterized by a slight change in the circumferential direction (along the weld), in order to reduce the time of numerical investigation and the requirements for the power of computing resources, the numerical schemes in the program code are implemented in a 2D axisymmetric formulation. To develop 2D FE model the assumption of a fast moving welding source and 'plain strains' hypothesis are used.

The software includes a database of input data on the physical and mechanical properties of typical steels and aluminum alloys used for the production of pipeline elements and pressure vessels, which simplifies the procedure for performing calculations and reduces the error of the results of numerical analysis due to the incompleteness of the reference information available to the user. Similarly, the geometry of the welded butt joint can be both determined from a set of available pre-installed options used for structural elements of critical purpose, and entered by the user in the presence of the necessary information regarding a specific design solution.

USER INTERFACE

The user interface of the software is designed for welding engineers who do not have special knowledge in mathematical methods. All tasks for developing a finite element model of a multipass girth welded joint are fully automated. All calculation results can be presented in both the graphical and tabular form. It is possible to copy information from any window to a graphic file, clipboard or to a printer. To save all input data and calculation results, there is a function for saving a variant. Figures 2, 4 show the computer program windows: the main window (Figure 2) for entering the geometrical parameters of the cylindrical structure and circumferential welded joint, the base and filler materials, welding conditions and operational load. Also shown are the PWHT simulation windows (Figure 3) and the module for probabilistic assessment of crack-like defect acceptability in the zone of the welded joint (Figure 4).

THE MAIN LIMITATIONS OF THE COMPUTER PROGRAM:

- metallic materials: steel, light alloys, titanium and nickel alloys;
- geometrical parameters of the cylindrical structure: diameter D = 2–10000 mm; wall thickness H = 1.0–20.0 mm, $H < D/2$; length $2L$ = 60–2000 mm, $L > 30H$;
- preparation of the edges of the circumferential welded joint is one-sided (from the outside);
- the number of welding passes in the circumferential joint is from 1 to 200;
- the material of the structure is considered as a macrocontinuous isotropic elastic-plastic medium capable of strain hardening;

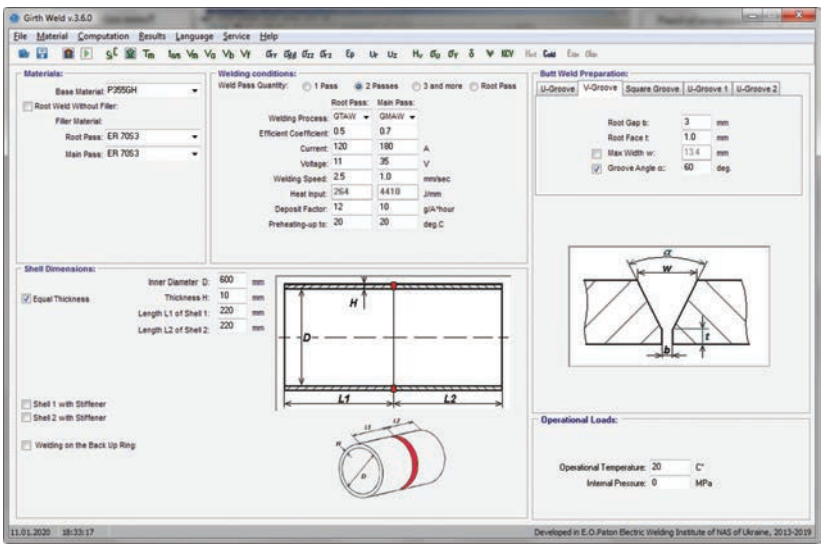

Figure 2. The main window of the computer program "Girth Weld"

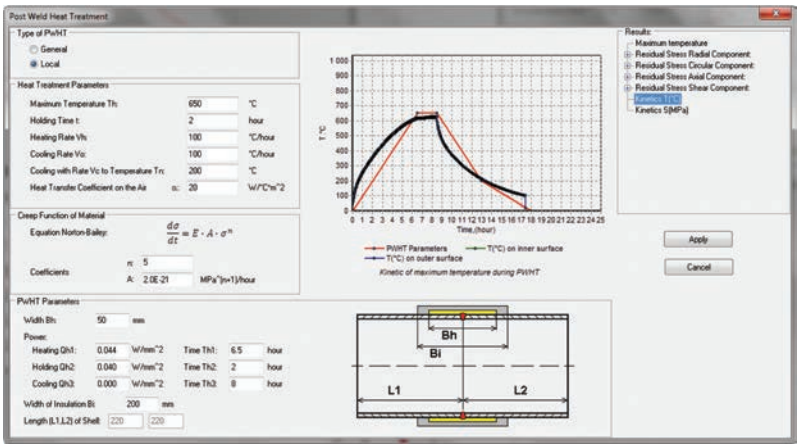

Figure 3. The window of PWHT simulation

● maximum temperatures during welding do not exceed the boiling point of the metal of the structure;

● the structures are not subject to the influence of cryogenic temperatures during operation;

● operational loads: internal pressure from 0 to $P < (0.5\sigma_T 2H/D)$, for example, if H = 5 mm, D = 400 mm, σ_T = 170 MPa, then $P < 2.125$ MPa.

● defect acceptability is determined by the conditions of static or quasi-static strength, while the application of assessment methods corresponds to the framework of application of specific criteria used in accordance with the relevant regulatory documents.

Cracks: semi-elliptical in the axial and circumferential directions, on the outer and inner surfaces. Crack dimensions: depth $a_0 < H$, length $2c_0$, $a_0/c_0 < 0.7$. Crack growth occurs by the fatigue mechanism.

Pores: diameter $d_0 < 1.0$ mm, depth r_0: $d_0/2 < r_0 < H - d_0/2$.

Wall thinning [11]: on the outer and inner surfaces. Thinning dimensions: depth a_0: $a_0 < H/2$, length $2s_0$: $2s_0 < L/2$. Thinning increase occurs by corrosion mechanism.

THE ERROR ENSURED IN THE RANGE OF ACCEPTABLE PARAMETERS OF NUMERICAL ANALYSIS

The adequacy of the developed models and their software implementation is ensured and confirmed both by the validation and verification procedures carried out, and by the experience of successful implementation and use of calculation methods and software in optimizing the industrial technologies of welding circumferential joints of critical structures and confirming their operability and service life by domestic and foreign enterprises of the energy, machine-building, transport, and aerospace industries. As shown by comparison of the results of calculations using the computer program "Girth Weld" with experimental measurements, the error of numerical analysis generally does not exceed 10–15 %.

VERIFICATION OF SIMULATION RESULTS FOR WELDING OF A DISSIMILAR GIRTH PIPELINE JOINT

Residual stresses are important for considering the problems of cracking and fracture of welded struc-

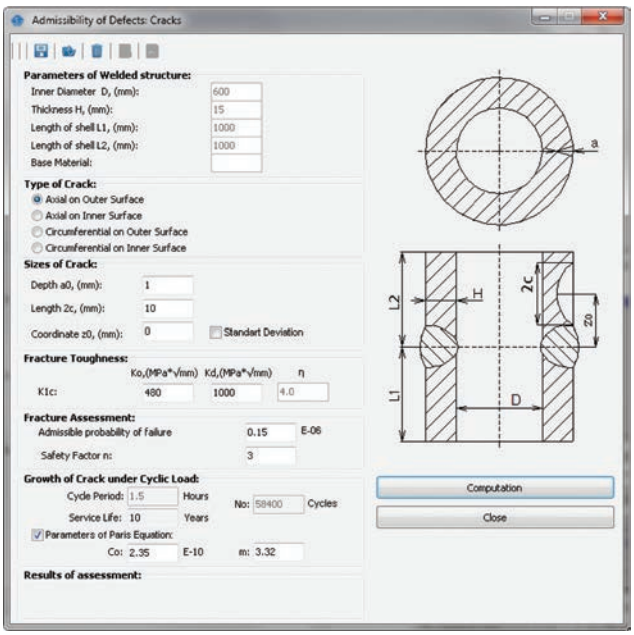

Figure 4. The window of the module for probabilistic assessment of the crack-like defect acceptability

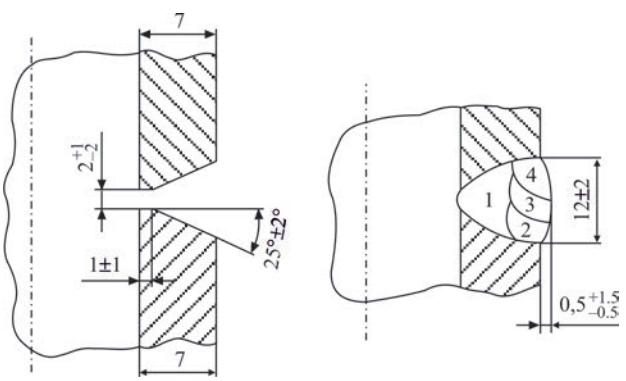

Figure 5. Preparation of edges of U-type for the welded pipe joint (SMAW) (*a*), arrangement of the weld passes (*b*)

Table 1. Mechanical and thermophysical properties of the materials

T, °C	*E*, MPa	α, (10*e*–6·1/K	λ, J/cm·s·deg	*C*, J/cm³·deg
Martensitic steel 12 % Cr				
20	215404	12.1	0.18	3.53
100	211697	12.1	0.19	3.75
200	205591	12.4	0.20	4.02
300	197750	12.8	0.22	4.32
400	188169	13.1	0.23	4.68
500	177028	13.5	0.24	5.15
600	164580	13.9	0.25	6.09
700	154030	13.0	0.27	6.00
800	131900	12.1	0.29	5.20
900	120604	11.1	0.31	4.64
1000	111687	12.5	0.32	4.75
1100	102607	13.6	0.33	4.90
1400	34172	17.5	0.36	9.50
1500	0	24.1	0.35	5.64
Austenitic steel 0.12C–Cr18Ni10T				
20	196531	19	0.146	3.54
100	191369	19	0.156	3.70
200	184280	19	0.168	3.86
300	176922	20	0.180	3.99
400	169296	20	0.193	4.11
500	161416	20	0.205	4.24
600	153303	20	0.218	8.32
700	141463	21	0.236	4.73
800	133320	21	0.249	4.56
900	125217	21	0.262	4.77
1000	116988	22	0.275	4.80
1100	108545	22	0.288	4.96
1200	99881	22	0.301	5.13
1300	88793	23	0.316	5.87
1400	2102	26	0.319	27.00
1500	0	30	0.319	5.64

tures and can be simulated for the welding process. The development of new heat-resistant steels for the power industry, where pipes joined by circumferential welding are often used, requires studying the influence of welding processes and residual stresses on the safe and reliable operation of power plants.

Finite element modeling of the multipass SMAW process (manual arc stick welding) was performed for a girth weld of a pipe with an outer diameter of 42 mm and a wall thickness of 7 mm made of 12 % Cr martensitic steel and dissimilar materials (austenitic or pearlitic steel). Such welded joints are used for pipes in the superheater of a boiler in thermal power plants.

The purpose of mathematical modeling is to predict temperature fields and kinetics of the stress-strain state during multipass welding, taking into account

Table 1. Cont.

T, °C	*E*, MPa	α, (10*e*–6·1/K	λ, J/cm·s·deg	*C*, J/cm³·deg
Welding material E–0.11C–Cr16Ni25Mo6Mn2N (austenitic)				
20	203437	18	0.119	3.58
100	198385	18	0.130	3.73
200	191493	18	0.145	3.87
300	184422	18	0.160	3.99
400	177172	19	0.175	4.10
500	169742	19	0.190	4.21
600	162130	19	0.205	4.41
700	153178	19	0.220	4.57
800	144799	20	0.235	4.84
900	135985	20	0.249	5.05
1000	126625	21	0.263	5.32
1100	117816	21	0.277	4.88
1200	109326	21	0.292	4.99
1300	100669	21	0.307	5.10
1400	74695	22	0.320	11.56
1500	0	28	0.319	5.74

the martensitic steel class, the choice of welding materials, welding conditions, preheating temperature, as well as determining the residual stressed state after welding and PWHT.

After preliminary experiments with testing of the welding technology, more acceptable welding parameters were selected, with filling of the weld groove in 4 passes (Figure 5). For a dissimilar welded joint (steel 12 % Cr + austenitic steel 0.12C–Cr18Ni10T), electrodes of the E–0.11C–Cr16Ni25Mo6Mn2N type with a diameter of 3.0 mm were selected with the following parameters: for 1 pass $I = 75–85$ A, $U = 24$ V, $V \approx 1.8$ mm/s, for 2–4 passes $I = 85–90$ A, $U = 24$ V, $V \approx 2.6$ mm/s. Welding procedure was elaborated by V. Skulskyi, A. Gavrik, M. Nimko in PWI.

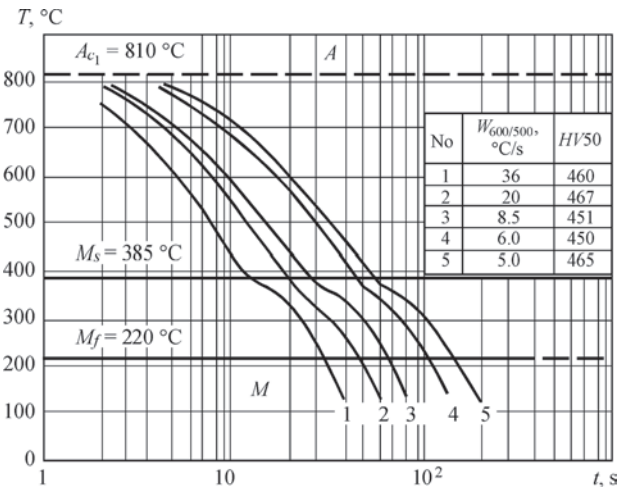

Figure 6. CCT diagram for steel X10CrMoVNb91 [7]

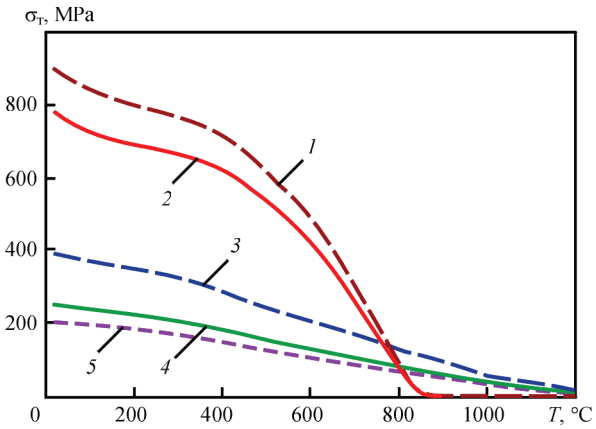

Figure 7. Yield stress versus temperature and microstructure: *1* — V_m = 1.0 martensite Thermanit MTS616; *2* — V_m = 1.0 martensite of 12 Cr steel; *3* — V_a =1.0 austenite of 12 Cr steel; *4* — austenitic filler E–0.11C–Cr16Ni25Mo6Mn2N; *5* — austenitic base material 0.12C–Cr18Ni10T

The chemical composition, mechanical and thermal properties of the base and filler materials are presented in Table 1.

Considering the martensitic class of high-chromium (12 %) steel, the following conditions for the phase transformation of the HAZ microstructure are accepted:

$$\text{if } T > A_c, \text{ then } V_a = 1.0\ ,\ V_m = 0$$

$$\text{if } T < A_c \text{ and } \left(\frac{\partial T}{\partial t} < 0\right), \text{ then } V_j = V_j(T, t), j = a,m$$

$$V_m(T) = 1 - \exp\left(3\frac{T_s^{(m)} - T}{T_s^{(m)} - T_e^{(m)}}\right); \qquad (17)$$

$$V_a(T) = 1 - V_m(T), \quad \sum_j V_j(t) \equiv 1,$$

where $j = a$ corresponds to austenite, $j = m$ — to martensite, $V_j(T, t)$ — is determined from the CCT diagram for the steel with the corresponding chemical composition. An example of CCT diagram of austenite decomposition for steel X10CrMoVNb91 is given in Figure 6 [7]. Dependences of yield stress of base and welding materials on temperature and microstructure are presented in Figure 7.

Comparison of the results of numerical calculations using 2D and 3D models (Figure 8) for butt welding of pipes made of dissimilar materials (12 % Cr steel + austenitic steel) shows a good agreement.

The results in Figure 9 demonstrate a rather close distribution of maximum temperatures during welding of all four passes using 2D and 3D models. In the diagrams, the red color corresponds to the shape of the FZ, the size of the HAZ is limited by the isotherm of 800–850 °C and reaches approximately 1.5–2–5 mm, the depth of the weld metal penetration into the base material is approximately 1 mm. The FZ, the depth of the weld penetration and the temperature range in the HAZ correspond to general expectations.

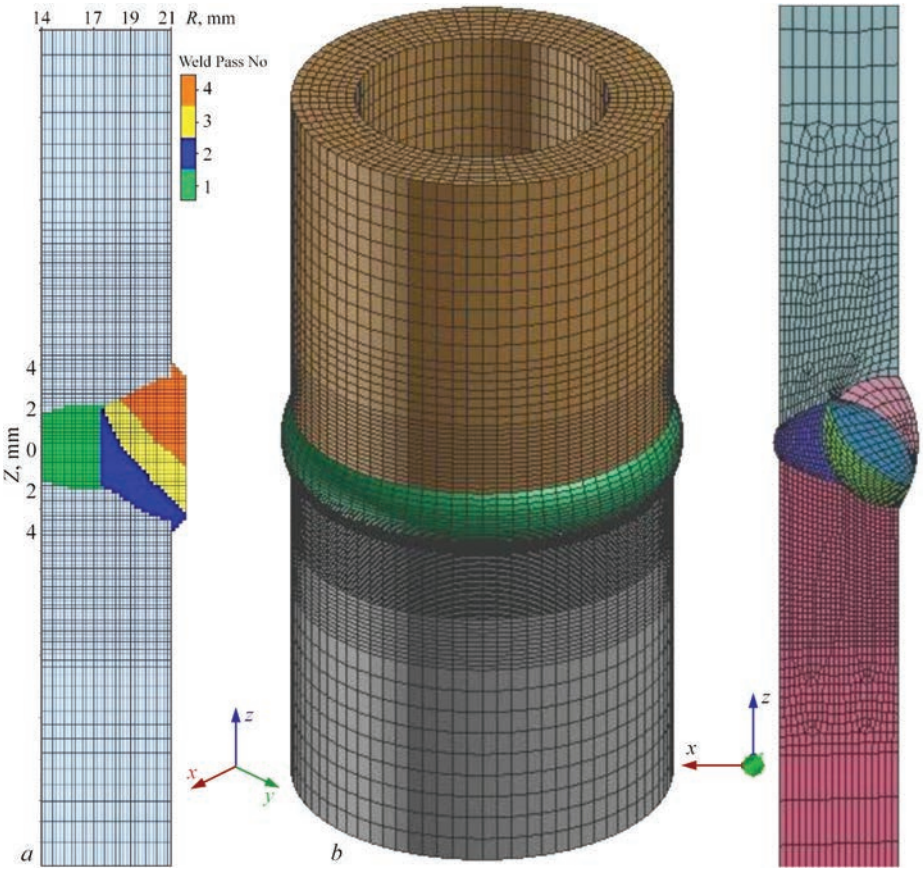

Figure 8. FE mesh of 2D (*a*) and 3D (*b*) models of a girth welded joint

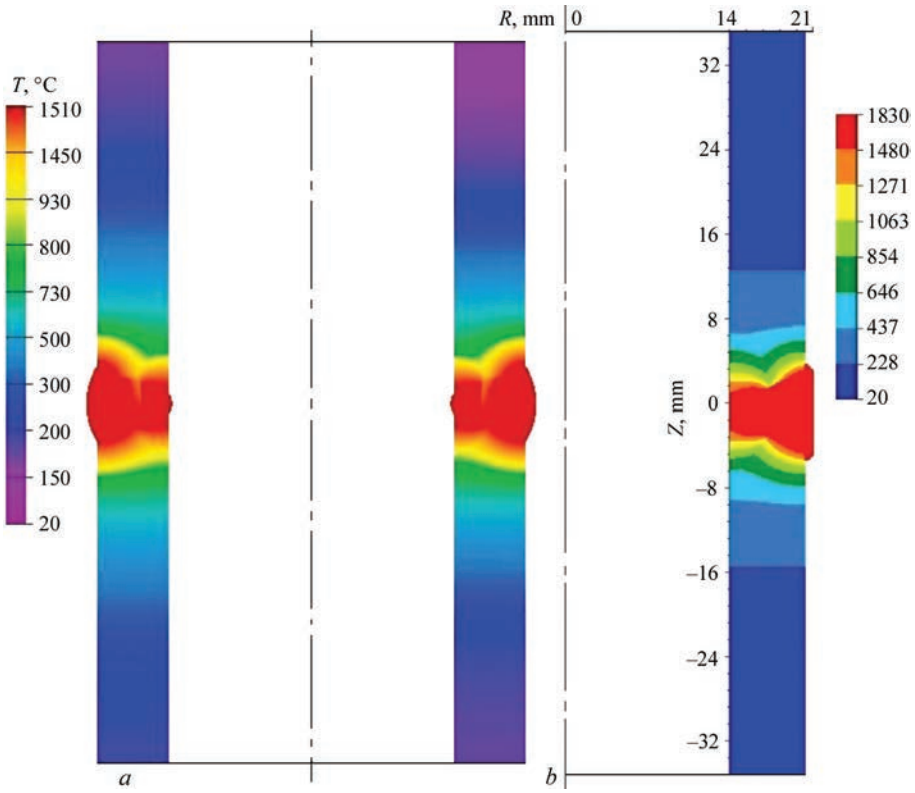

Figure 9. Comparison of calculated distributions of maximum temperature and FZ (red color) in the cross section of a girth welded joint: *a* — 3D model; *b* — 2D model by software "Girth Weld"

Figure 10 shows the calculated distributions of welding residual stresses (circumferential component). In the FZ, where the filler material has an austenitic microstructure, high tensile stresses of up to 450 MPa are produced. In the HAZ of the base material of 12 % Cr steel (lower part of the pipe in Figure 10), due to martensitic transformation, local high compressive stresses of up to –350 MPa appear, as well as local tensile stresses of up to 180–300 MPa according to 2D analysis and up to 50 MPa according to 3D analysis, which balance the compressive stresses. The width of the zone of tensile circumferential residual stresses in the pipe is quite small (approximately 2.0 mm). Further, on the periphery of the pipe

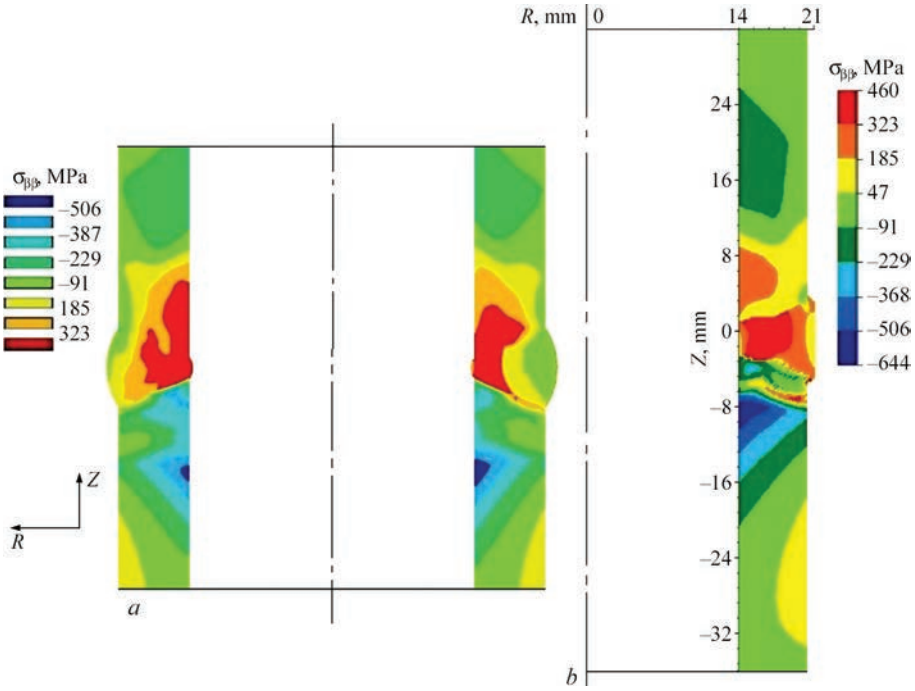

Figure 10. Comparison of numerically calculated distributions of welding residual stresses (circumferential component): *a* — 3D model; *b* — 2D model by software "Girth Weld"

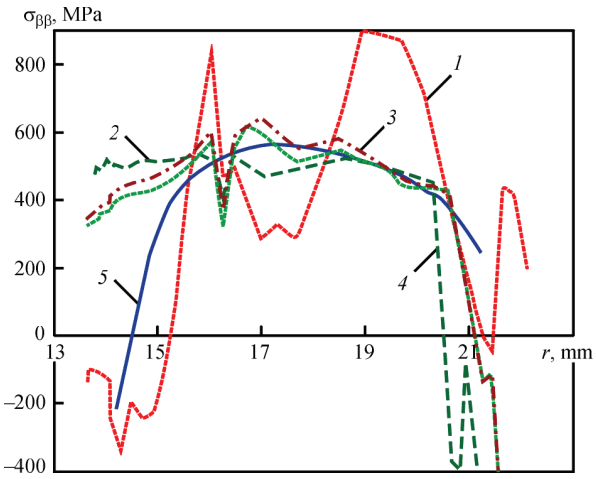

Figure 11. Residual circumferential stresses through the thickness in the center of welded joint for the 2D model and for the 3D model in different sections along the angular coordinate from the start-end of the welding (0, 90, 180, 270°): *1* — start-end; *2* — 90°; *3* — 180°; *4* — 270°; *5* — 2D

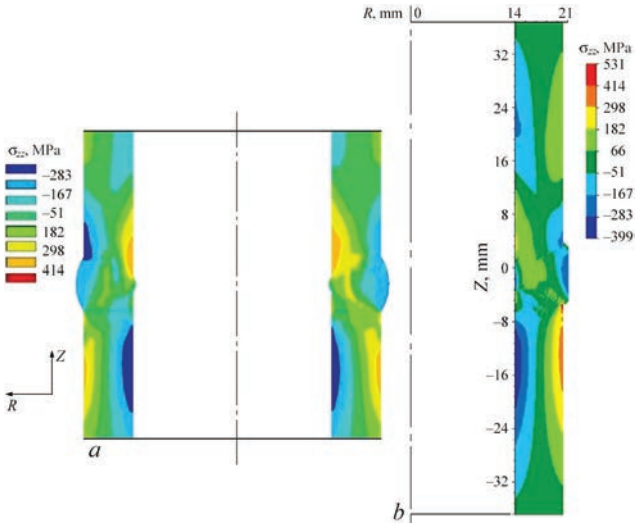

Figure 12. Comparison of numerically calculated distributions of welding residual stresses (axial component): *a* — 3D model; *b* — 2D model "Girth Weld"

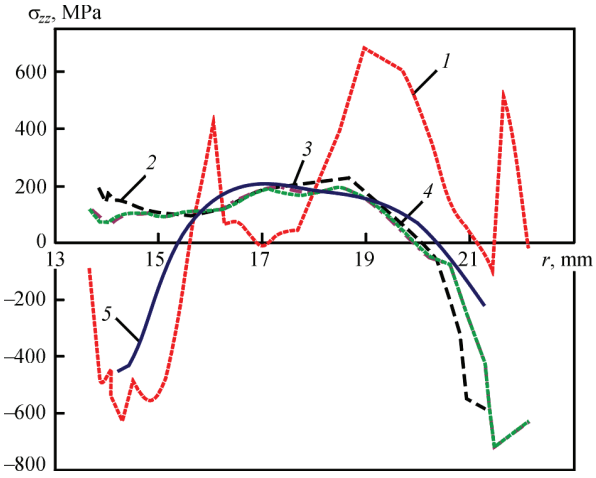

Figure 13. Residual axial stresses through the thickness in the center of welded joint for the 2D model and for the 3D model in different sections along the angular coordinate from the start-end of welding (0, 90, 180, 270°): *1* — start-end; *2* — 90°; *3* — 180°; *4* — 270°; *5* — 2D

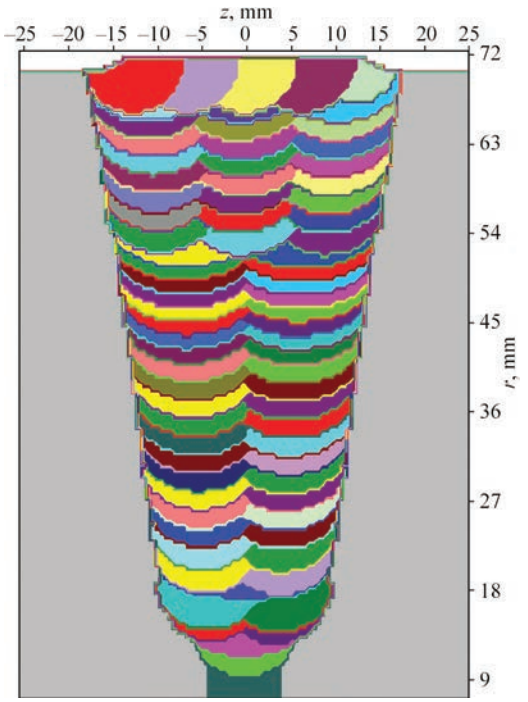

Figure 14. Simulation results of the weld groove filling (weld passes arrangement) for the girth joint of MCP DN-850

made of 12 % Cr steel, compressive stresses of up to –640 MPa are produced on the inner surface and tensile stresses of up to 180 MPa on the outer surface. Figure 11 shows the residual circumferential stresses through the thickness in the center of welded joint for the 2D model and for the 3D model in different sections along the angular coordinate from the start-end of welding (0, 90, 180, 270°). One stress curve differs significantly from the other due to the effect of the start and end of welding in the 3D model. In general, the circumferential stresses determined by the 2D model are close to the results by the 3D model.

The results of the distribution of welding residual stresses for the axial component in Figures 12 and 13 according to the 2D and 3D models also agree well. The martensitic structure of the 12 % Cr steel causes

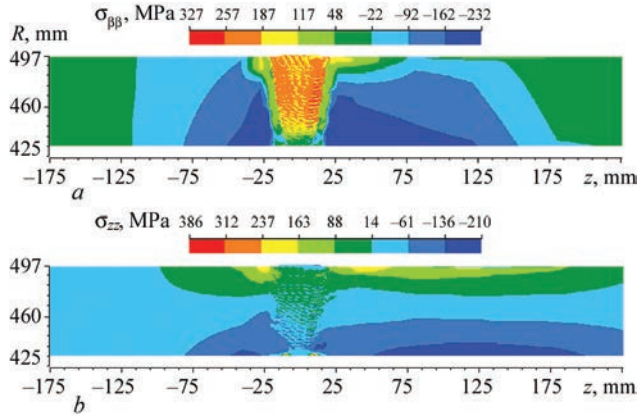

Figure 15. Calculated data on the distribution of residual stresses in the circumferential weld zone of MCP DN-850 after PWHT: *a* — circumferential component; *b* — axial component

a change in the traditionally produced residual axial tensile stresses on the inner surface to compressive stresses up to –400 MPa and, accordingly, of the compressive stresses on the outer surface to tensile stresses up to 400 MPa. This effect can be positive for pipes with a corrosive environment on the inside.

Despite the slight difference in the distribution of residual stresses determined by the 3D model in different cross-sections of the pipe by the angular coordinate, a good agreement with the 2D model is obtained. Thus, the 2D model of the girth weld joint can be used to simulate the distributions of maximum temperatures, microstructural phase composition, mechanical properties, residual stresses and strains in multipass welding of a butt joint of pipelines and cylindrical shells (vessels).

VALIDATION OF MULTIPASS WELDING SIMULATION FOR A PIPELINE GIRTH WELDED JOINT

Calculations performed using the "Girth Weld" computer program provided comprehensive information regarding the distribution of residual welding stresses throughout the volume of the welded joint of the main circulation pipeline (MCP) DN-850 for WWER-1000 type reactors. For validation of the simulation results, experimental measurement data were used. These measurements were carried out on a specimen-model of the girth welded joint of MCP DN-850 on accessible surfaces of the welded components after PWHT, in order to compare with the calculated data.

The computational methodology is based on sequential tracking of the development of temperature fields, stresses, and deformations during the step-by-step filling of the weld groove with weld passes (Figure 14). For each pass, based on experimental data on the parameters of the GTAW process in an argon environment, the dimensions of the FZ and the HAZ of the base material (steel grade 10GN2MFAA) were determined. Based on the size of the FZ and the chemical composition of the filler (Sv-08G1NMA wire), the chemical composition of the metal for each weld pass was calculated.

To simulate the microstructural phase transformations in the FZ and HAZ of low-alloy steels during welding, an approach based on the use of parametric

Table 2. Welding parameters for the girth joint of MCP DN-850 (using ∅ 0.9 mm wire)

Welding passes	Welding parameters					
	I, A pulse/pause	U, V	v, mm/min	Wire feed rate, v_f, mm/min, pulse/pause	Time, μs pulse/pause	Argon flow rate, l/min
First root pass (1)	150/120	9.5	80	880/360	100/100	20–25
Smoothing layer (2)	160/90	10	86	–	100/100	
Third root pass (3)	220/130	11.5	91	2000/1000	225-275	
Fourth root pass (4)	250/150	11.5	89	2600/1300	225/275	
Intermediate filling layer (5–8)	300/180	11.5	89	3400/1620	225/275	
Main filling layer (9–104)	340/200	12	110	3200/1620	225/275	
Reinforcement layer (105–112)	260/110	11.5	80.3	1520/1000	175/325	

Table 3. Mechanical and thermophysical properties of 10GN2MFA steel depending on temperature [1]

T, °C	$E\cdot10^{-5}$, MPa	$\sigma_T(T)$, MPa	λ, J/(cm·s·°C)	$c\gamma$, J/(cm^3·°C)	v	α, 1/°C
100	2.01	488	0.375	3.88	0.25	1.14
200	1.96	466	0.370	3.98	0.25	1.18
300	1.90	443	0.360	4.21	0.25	1.22
350	1.87	415	0.355	4.44	0.25	1.25
400	1.85	380	0.350	4.76	0.25	1.30
500	1.78	355	0.337	5.10	0.25	1.34
600	1.70	300	0.320	5.80	0.25	1.39
700	1.60	200	0.305	7.35	0.25	1.42
800	1.50	60	0.285	8.10	0.25	1.47
900	1.35	40	0.280	5.60	0.25	1.52
1000	1.15	20	0.275	5.00	0.25	1.65
1100	1.00	20	0.270	4.90	0.25	1.70
1200	1.00	20	0.267	4.90	0.25	1.62

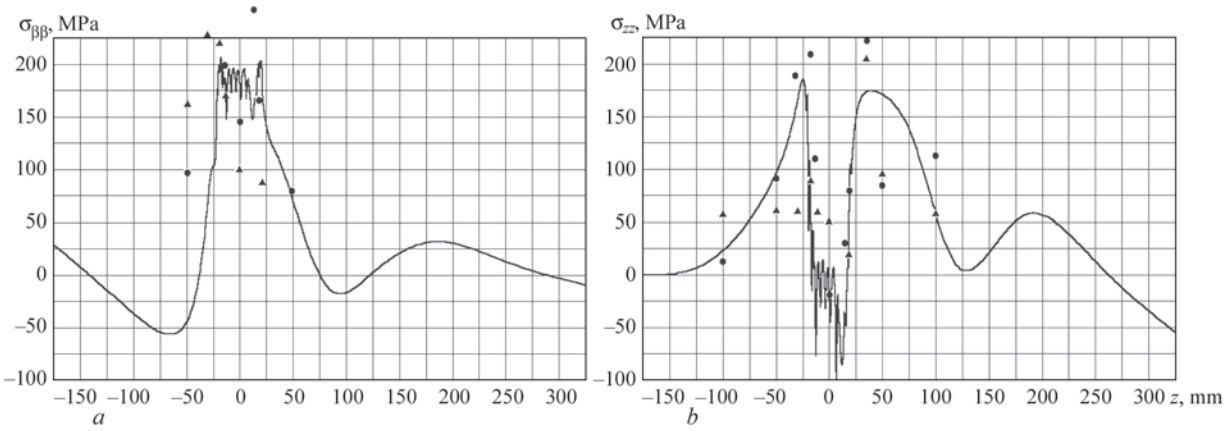

Figure 16. Comparison of calculated and experimental data on residual stress distribution on the outer surface of the MCP DN-850 welded joint [1]: *a* — circumferential component; *b* — axial component

(regression) equations developed at the PWI [8] can be applied.

According to the kinetics of microstructural transformations in the weld metal and the HAZ, the volumetric effects were determined at respective time moments t and temperature T. For steel grade 10GN2MFAA, dependencies (8) were used to determine the parameter γ_j.

The yield stress of the finite volume material at temperature T allowing for the microstructural phase changes was calculated according equation (9). For the type of steels considered, data for the yield stress of the j-th microstructure of the material at temperature T are presented in Figure 16.

The creep function coefficients for the base material of the welded joint (steel 10GN2MFA) were determined in [1] based on processing of experimental data: $n = 5$, $A = 8.46 \cdot 10^{17}$ MPa$^{-(n+1)} \cdot h^{-1}$, $G = -66394$ °C.

Experimental measurements were performed on a welded and heat-treated specimen-model of a welded joint with standard processing. Measurements were carried out on the surfaces, i.e., in places accessible for installing strain gauges and further drilling holes to implement the well-known Matara method. Measurements were performed at 24 locations. Figure 16 shows a comparison of calculated and experimental data on the distribution of residual stresses on the outer surfaces of the MCP DN-850, which confirmed the rather high accuracy of the calculation method for determining residual welding stresses.

CONCLUSIONS

The software "Girth Weld" allows in the typical cases of circumferential (girth) welded joints of pipelines and pressure vessels to obtain information on the mechanical properties of the weld metal and HAZ, residual stresses and deformations, to determine the redistribution of the stress-strain state as a result of PWHT, the influence of operational and test loads, to predict the structural integrity and service life of welded structures with discontinuity defects, which are detected as a result of non-destructive testing or postulated.

The computer program is oriented for engineering and scientific application and does not require the user to have special knowleadge in the calculation methods due to the full automation of the processes of creating a mathematical model, dividing the area into finite elements, finding a solution and visualizing the results.

At the same time, the software provides high accuracy of prediction results with limited requirements for computer and time resources due to the use of modern approaches to modeling physical and chemical processes in welding and economical algorithms for solving nonlinear problems and systems of high-order differential equations.

Calculations were carried out for two test problems that are of practical interest and show the main declared capabilities of the computer program "Girth Weld". The verification results indicate that the physical models and processes implemented in the computer program are correct, correspond to the accepted modern approaches for the description of physico-chemical processes during welding heating, mechanics of a deformable body and fracture mechanics. Based on the satisfactory agreement of the calculation results with the experimental measurements on the test sample of the girth welded joint of the pipeline DN850 of the first circuit of the WWVER-1000 reactor made of pearlitic steel, the software "Girth Weld" has been validated and can be used for modeling mechanical properties and the stress-strain state in the zone of butt circumferential welded joints of pipelines and pressure vessels.

REFERENCES

1. Makhnenko, V.I. (2006) *Resource of safe operation of welded joints and units of modern structures*. Kyiv, Naukova Dumka [in Russian].
2. Makhnenko, V.I., Velikoivanenko, E.A., Pochinok, V.E. et al. (1999) Numerical methods for the predictions of welding stresses and distortions. *Welding and Surfacing Rev*., Vol. 13, Pt 1, 1–146.

3. Velikoivanenko, E.A., Milenin, A.S., Popov, et al. (2020) High-performance methods for analyzing the statistical strength of welded pipelines and pressure vessels using the Monte Carlo method. *J. of Automation and Information Sci*., 52(**11**), 12–27. DOI: https://doi.org/10.1615/JAutomatInfScien.v52.i11.20
4. Velikoivanenko, E.A., Milenin, A.S., Popov, A.V. et al. (2020) High-performance methods for analyzing the statistical strength of welded pipelines and pressure vessels using the Monte Carlo method. *J. of Automation and Information Sci*., 52(**11**), 12–27. DOI: https://doi.org/10.1615/JAutomatInfScien.v52.i11.20
5. Milenin, A., Velikoivanenko, E., Rozynka, G. et al. (2025) Methodology of multi-scale numerical prediction of the stress-strain state of welded large-size structures. *Lecture Notes in Mechanical Eng*., **2**, 167–175. DOI: https://doi.org/10.1007/978-3-031-82979-6_17
6. Yuryev, S.F. (1950) Specific volumes of phases in the martensitic transformation of austenite. Moscow, Metallurgizdat [in Russian].
7. Skulsky, V.Yu. (2006) Effect of the degree of alloying of heat-resistant chromium steels on hardness of metal within the welded joint zone. *The Paton Welding J*., **9**, 17–20.
8. Zeiffarth, P., Kasatkin, O.G. (2002) Calculation models for evaluation of mechanical properties of HAZ metal in welding of low-alloy steels. In: *Proc. of the Inter. Conf. on Mathematical Modeling and Information Technologies in Welding and Related Processes, Kyiv, 2002*, 103–106. https://patonpublishinghouse.com/proceedings/mmw2002.pdf
9. Belomytsev, M.Yu., Molyarov, V.G. (1994) Study of the structure and construction of the thermokinetic diagram of the decomposition of austenite in 10GN2MFA steel. *Izv. Vuzov, Chyorn. Metallurgiya*, **3**, 47–49 [in Russian].
10. Makhnenko, O.V., Milenin, O.S., Muzhychenko, O.F. et al. (2023) Mathematical modeling of residual stress relaxation during performance of postweld heat treatment. *The Paton Welding J.,* **6**, 32–40. DOI: https://doi.org/10.37434/tpwj2023.06.05
11. Milenin, O.S., Velykoivanenko, O.A., Rozynka, G.P., Pivtorak N.I. (2020) Numerical methodology of prediction of the reliability and residual life of welded pipeline elements with corrosion-erosion defects. *The Paton Welding J*., **9**, 4–13. DOI: https://doi.org/10.37434/tpwj2020.09.01

ORCID
L.M. Lobanov: 0000-0001-9296-2335,
O.V. Makhnenko: 0000-0002-8583-0163,
O.S. Milenin: 0000-0002-9465-7710,
O.A. Velykoivanenko: 0009-0007-3704-2000,
G.P. Rozynka: 0009-0009-1750-7266,
G.Yu. Saprykina: 0000-0003-1534-7253

CONFLICT OF INTEREST
The Authors declare no conflict of interest

CORRESPONDING AUTHOR
O.V. Makhnenko
E.O. Paton Electric Welding Institute of the NASU
11 Kazymyr Malevych Str., 03150, Kyiv, Ukraine.
E-mail: makhnenko@paton.kiev.ua

SUGGESTED CITATION
L.M. Lobanov, O.V. Makhnenko, O.S. Milenin, O.A. Velykoivanenko, G.P. Rozynka, N.R. Basystuk, G.Yu. Saprykina (2025) Computer software for modeling a circumferential welded joint. *The Paton Welding J*., **8**, 55–67.
DOI: https://doi.org/10.37434/tpwj2025.08.06

JOURNAL HOME PAGE
https://patonpublishinghouse.com/eng/journals/tpwj

Received: 28.05.2025
Received in revised form: 03.07.2025
Accepted: 07.08.2025

DOI: https://doi.org/10.37434/tpwj2025.08.07

IRON-BASED BINDER ALLOY FOR PLASMA TRANSFERRED-ARC SURFACING OF COMPOSITE ALLOYS REINFORCED WITH CAST TUNGSTEN CARBIDES

O.I. Som

Plasma-Master Co., Ltd.
3 Omelian Pritsak Str., 03142, Kyiv, Ukraine

ABSTRACT

Five iron-based industrial alloys with different alloying systems have been studied for the purpose of using them as a binder alloy for plasma-transferred arc surfacing of composite alloys, reinforced with cast spherical tungsten carbides (relite). It is shown that hard and wear-resistant alloys, such as Sormite-1 (PG-S1) and others do not provide an overall increase in the deposited metal wear resistance. Contrarily, they reduce it, as they poorly hold the tungsten carbide grains, which break away and are removed from the friction zone together with the matrix, not contributing to the resistance to wear. Alloys of Kh18N9 type are not suitable, either, as they significantly increase their hardness and thus lower their ductility during surfacing due to additional alloying with carbon and tungsten. The best result was shown by a relatively soft copper-nickel alloy (cast iron) Ni-Resist.

KEYWORDS: plasma transferred-arc surfacing (PTA surfacing), spherical tungsten carbides, binder alloy (matrix), wear resistance, hardness, metal formation

INTRODUCTION

Binder alloy plays a big role in surfacing the wear-resistant composite alloys based on cast tungsten carbides (relite). It should reliably hold the carbide particles from breaking away and provide a high wear resistance of the deposited metal on the whole, particularly under the conditions of impact-abrasive wear. Moreover, it should ensure good formation of the deposited metal and resistance to cracking in welding.

In practice low-melting self-fluxing nickel-based alloys of Ni–Si–B or Ni–Cr–Si–B–C systems of different hardness are widely used as binder alloy for plasma transferred arc (PTA) surfacing of composite alloys reinforced with tungsten carbides [1, 2, 12].

A disadvantage of application of such alloys, particularly in high-productivity surfacing (>3 kg/h), is spatter deposition on the plasma torch edge, which over time clogs the powder feed channel in long-term operation, and, consequently, disrupts the technological process of surfacing. During application of plasma torches with inner powder feed [3] the surfacing process disruption occurs even faster, because of metal drops appearing at the outlet of the focusing nozzle.

Proceeding from that, iron-based alloys are attractive in terms of increasing the stability of the surfacing process. They have higher melting temperature and are less prone to drops forming at the plasma torch outlet during surfacing. In addition, they are much less expensive than the nickel alloys. Attempts to use iron-based alloys as a binder alloy were made before [4, 5], but they are not of a systemic nature, and do not provide replies or recommendations as to alloy selection.

OBJECTIVE OF THE WORK

The objective of this work is searching for an iron-based commercial alloy for using it as a binder during PTA surfacing of composite alloys based on tungsten carbides.

Selection criteria are as follows: formation of the deposited metal; crack resistance of the deposited composite metal; surfacing process stability; wear resistance under the conditions of abrasive wear; strength of deposited metal adhesion to the base.

INVESTIGATION MATERIALS

The following industrial alloys, which in the author's opinion can be used as the binder alloy, were selected for investigations (Table 1). These alloys are produced by various foreign manufacturers in the form of powders suitable for PTA surfacing. Powders of 63–160 μm fraction were used in the experiments.

To compare the service properties of the deposited metal, we also used in the experiments the known surfacing composite powder Durmat 61-PTA produced by DURUM Verschleißschutz GmbH (Germany), which is a mixture of powders of Durmat 59-PTA grade (nickel-based alloy of Ni–Si–B system of 50 *HRC* hardness) and crushed tungsten carbide in the proportion of 40:60 wt.%, respectively.

The selected alloys differ significantly by chemical composition, deposited metal type, hardness and wear

Table 1. Chemical composition of iron-based alloys used in the experiments as binder alloy

Binder alloy type (powder grade)	Chemical element composition, wt.%								Hardness, *HRC*
	C	Mn	Si	Cr	Ni	V	Mo	Cu	
1. 08Kh18N9 (PR-Kh18N9)	0.08	0.7	0.5	18.0	9.5	–	–	–	140 *HB*
2. 270N15D7Kh3CS2 (PR-ChN15D7)	2.7	0.8	2.1	2.8	14.8	–	–	6.5	26
3. 220Kh18F7N3M2 (PMalloy 21)	2.2	0.8	0.7	17.8	2.8	7.1	2.4	–	46
4. 300F11Kh6NM (Plasweld™FerroV10)	3.0	0.9	0.8	6.0	0.6	10.8	1.4	–	60
5. 300Kh30N4S2 (PG-S1)	3.0	1.2	3.2	29.8	4.0	–	–	–	54

resistance. Such a wide range of the alloys allows for better assessment of the influence of matrix type on the welding-technological and service properties of the composite deposited metal.

BRIEF CHARACTERISTICS OF THE ALLOYS

Alloy No. 1 is the classic (18–9) chromium-nickel steel of austenitic class. It is characterized by a high corrosion resistance and ductility, which is highly important under the conditions of abrasive wear with impacts. Application of such steel as the binder alloy is described in work [5].

Alloy No. 2 is the copper-nickel cast iron of austenitic class, known under the Ni-resist brand name [6]. It also has high corrosion resistance and ductility. In addition, it is non-magnetic and has high antifriction properties. The high carbon content ensures its good welding technological properties.

Alloys Nos 3 and 4 belong to the class of wear-resistant high-vanadium cast irons, the valuable properties of which are a fine-grained structure and increased impact toughness [7]. The main wear-resistant phase in them is primary vanadium carbides VC. We selected two compositions for the experiments, which differ by matrix type, hardness and wear resistance.

Alloy No. 3 has an austenitic-martensitic matrix with 44–46 *HRC* hardness, which ensures that it optimally combines high wear resistance with ductility required for resistance to impact loads and to cracking during surfacing [8].

Alloy No. 4 has a martensitic matrix with low austenite content (6–8 %). Its hardness after PTA surfacing is equal to 60–62 *HRC*. Compared to alloy No. 3, the deposited metal has more carbide phase, due to a higher alloying with vanadium and carbon.

Alloy No. 5 is a high-chromium cast iron of hypereutectic type, known as Sormite 1, which is characterized by a high wear-resistance under the conditions of abrasive wear. The structure of metal deposited with it consists of coarse chromium carbides of $Cr_{23}C_6$ type, carbide eutectics and residual austenite [9].

Used as the reinforcing wear-resistant material was powder of spherical tungsten carbide of 100–200 μm fraction, produced by Resurse-1 Ltd., Ukraine [10].

Deposition was performed on ground plates from steel 20 of 120×120×25 mm size, using equipment of Plasma-Master LTD Company with a plasma torch of RR-6-03 model (Figure 1).

The matrix and reinforcing powders were fed separately from two feeders in the proportion of 40:60 wt.% to avoid their separation and to maintain this proportion constant during the surfacing process. The powders were supplied to the weld pool as a mixture, formed by merging of the two flows directly at the inlet to the plasma torch.

Several surfacing variants were realized in the experiments. Both single and double beads were deposited with an overlap (Figure 2). Surfacing

Figure 1. Plasma transferred-arc surfacing unit with two powder feeders and RR-6-03 plasma torch

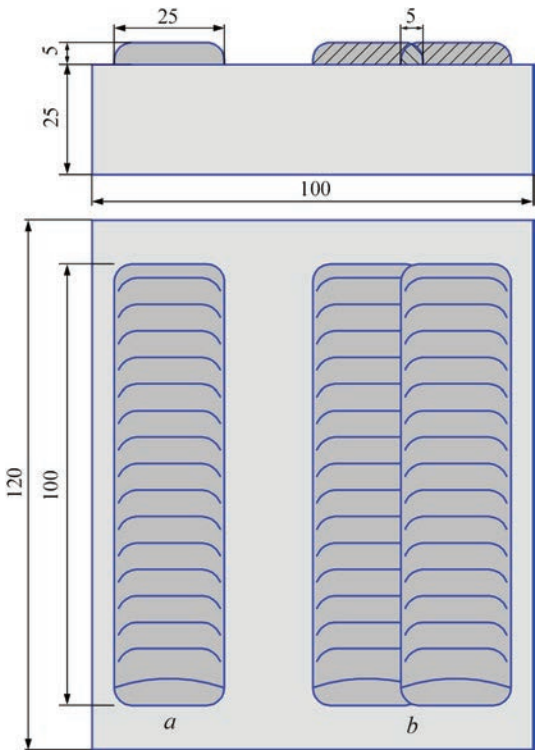

Figure 2. Schematic of surfacing the plates to study the formation and crack resistance of the deposited metal: *a* — single bead; *b* — double bead with an overlap

was performed without the sample preheating, with preheating to 300 °C and using an underlayer from chromium-nickel austenitic steel 08Kh18N9. The preheating and the underlayer were used as methods to prevent cracks in the deposited metal. Samples of 16×16×6 mm size (Figure 3, *a*) for testing the alloys for wear resistance in NK machine (stationary ring) [11] and samples of 50×16×8 mm size for surfaced metal testing for delamination during bending (Figure 3, *b*) were cut out of the surfaced plates by spark method. The upper part of the deposited layer in both the cases was ground to the level, at which the tungsten carbide particles were relatively uniformly distributed over the cross-section. The same samples were used for metallographic studies.

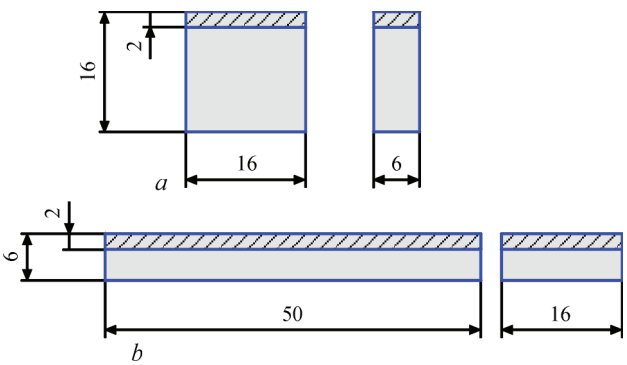

Figure 3. Samples for studying the deposited metal wear resistance in NK machine (*a*) and its delamination from the base during bending (*b*)

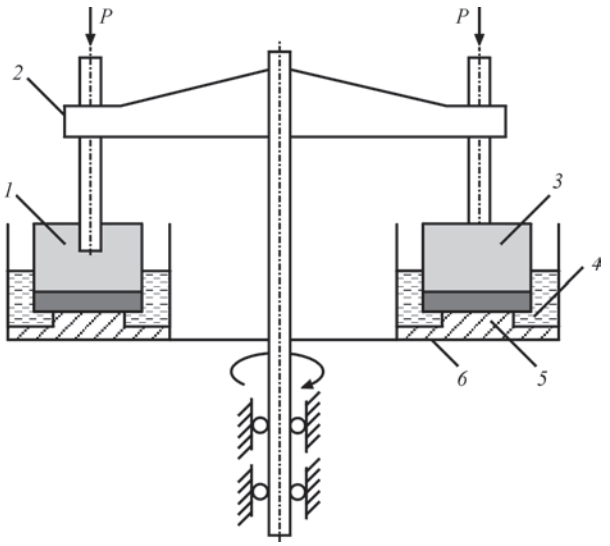

Figure 4. Schematic of wear resistance testing of surfaced samples in NK machine: *1* — test sample; *2* — rotating cross-piece; *3* — standard; *4* — abrasive with water; *5* — copper ring; *6* — bed plate

Quality of the deposited metal formation was assessed visually, and presence of cracks — visually and using dye penetrant flaw detection.

Schematic of wear resistance testing of the surfaced samples is shown in Figure 4.

Testing conditions were as follows: load on the sample — 3 kg, friction path — 700 m, sliding (friction) speed — 6 m/s, abrasive medium — wet river quartz sand.

The standard was annealed steel 45, which was used to control the wear conditions. The friction path length was selected from the condition of producing a noticeable wear of samples. Wear resistance was assessed by the loss of sample weight, using scales with up to 0.001 g precision.

Testing the samples for deposited metal delamination from the base was performed under static loading in the press by the schematic shown in Figure 5. Loading was applied from the base metal side. Bend angle was 150°.

Deposited metal microstructure was studied using Neophot-21 photomicroscope, and the microhardness was measured in Leco M400 Instrument.

ANALYSIS OF EXPERIMENTAL RESULTS. BEAD FORMATION

All the considered compositions without exception provide very good formation of the deposited metal, both during deposition of single beads and double

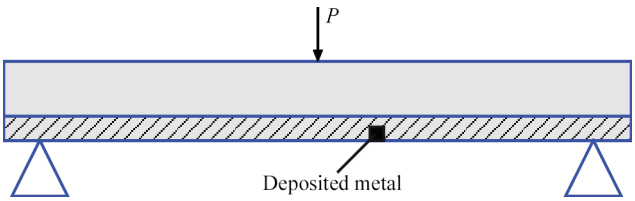

Figure 5. Schematic of testing samples for deposited metal delamination from the base

beads with an overlap. The beads are even and clean, without any traces of slag. In the points of bead overlapping in two-pass surfacing the metal is also clean. Base metal penetration is practically absent, which confirms the optimal balance of the surfacing parameters. Figure 6 shows as an example the appearance of the beads deposited using a composite alloy with binder No. 2 (270N15D7Kh3S2).

CRACKS IN THE DEPOSITED METAL

Visual examination and dye penetrant testing showed that cracks are present in some of the deposited beads. In case of deposition of individual beads without preheating cracks were observed in compositions Nos 1 and 5 (Table 2). They were located across the beads with minimal opening.

For variant No. 1 this is unexpected to some extent, considering the soft austenitic matrix. As shown by metallographic studies, however, it is soft only in surfacing without tungsten carbides (Table 2). In the presence of tungsten carbides its hardness HV_{01} is significantly increased from 150 to 600. It occurs due to additional alloying of the matrix with carbon and tungsten as a result of partial dissolution of tungsten carbide grains during surfacing, which is confirmed by X-ray microprobe analysis. With increase of the matrix hardness its ductility decreases naturally, leading to appearance of cracks in the deposited metal. During surfacing with preheating, no cracks were further observed in composition No. 1, and in composition No. 5 their number was greatly reduced. They disappeared completely in case of surfacing with preheating on the underlayer (Table 2).

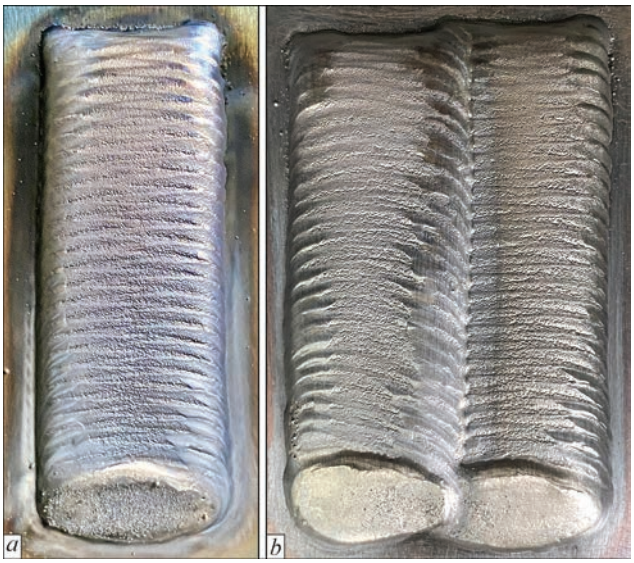

Figure 6. Appearance of beads deposited using a composite alloy with binder No. 2 (270N15D7Kh3S2): *a* — single bead; *b* — double bead with an overlap

Crack situation deteriorates considerably during deposition of beads with an overlap without sample preheating. Such a variant is observed during continuous surfacing of large surfaces (for instance, armor plates) and in deposition of closed circular beads. Cracks are observed both in the first and in the next beads. Their nature is different in different alloys. In compositions Nos 1 and 5 (Table 2) they look like a net (Figure 7, *a*), and in compositions Nos 3, 4 and 6 they look like isolated cracks, located approximately normal to the solidification layers. Only one crack was revealed in composition No. 2 (Figure 7, *b*).

Table 2. Results of investigation of cracking resistance of experimental composite alloys during surfacing

Composition	Number of cracks per 100 mm of the deposited bead length						Average microhardness of the matrix, HV_{01}	
	Single bead deposition			Deposition of two beads with overlap				
	Without preheating	With preheating 300 °C	With preheating on underlayer 300 °C	Without preheating	With preheating 300 °C	With preheating on underlayer 300 °C	Pure (without tungsten carbides)	With tungsten carbides
1. 08Kh18N9 + tungsten carbides	1	0	0	Network of cracks	1	0	150	600
2. 270N15D7Kh3S2 + tungsten carbides	0	0	0	1	0	0	270	400
3. 220Kh18F7N3M2 + tungsten carbides	0	0	0	2	1	0	440	460
4. 300F11Kh6NM + tungsten carbides	0	0	0	4	1	0	690	720
5. 300Kh30N4S2 + tungsten carbides	3	1	0	Network of cracks	2	1	580	610
6. Ni–Si–B + tungsten carbides	0	0	0	2	1	0	–	600

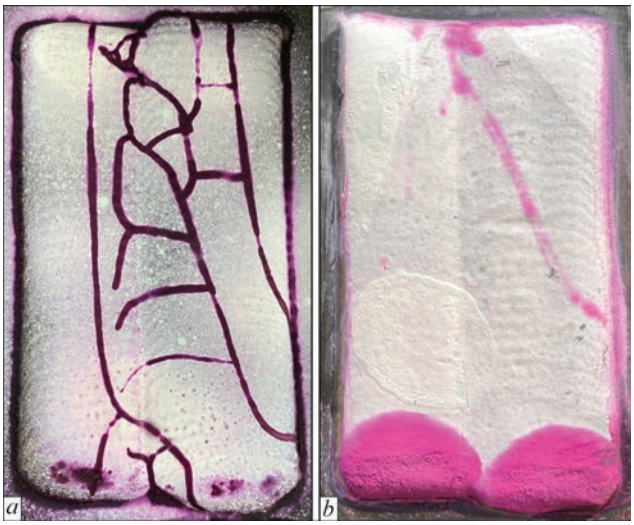

Figure 7. Cracks in deposited compositions: *a* — 08Kh18N9 + tungsten carbides; *b* — 220Kh18F7N3M2 + tungsten carbides

The cause for appearance of additional cracks is the thermal impact on the previous bead, having a high level of internal stresses, as well as higher rigidity of the joined beads.

Preheating noticeably decreases the number of cracks in the deposited metal, and presence of an underlayer from austenitic chromium-nickel steel even more promotes their reduction (Table 2). Cracking cannot be avoided only in deposition of composition No. 5 with binding alloy 300Kh30N4S2 (Sormite 1).

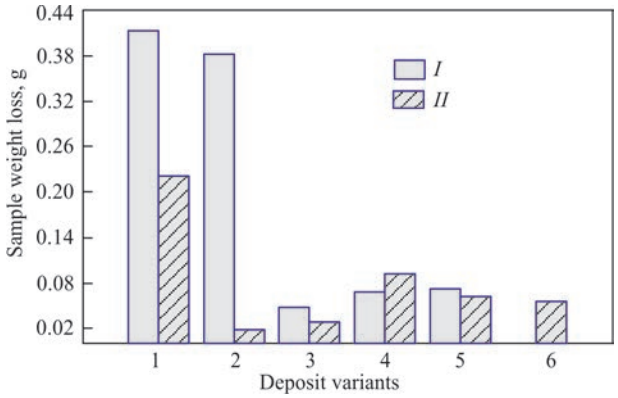

Figure 8. Diagram of wear resistance of the deposited metal variants tested in NK machine: *I* — pure binder alloy; *II* — composite alloy with tungsten carbides

DEPOSITED METAL WEAR RESISTANCE

As was mentioned above, the wear resistance of the surfaced samples was tested in the NK laboratory machine. The results are given in Table 3 and in Figure 8.

For better understanding of the matrix influence on the composite alloy wear resistance, an investigation of wear resistance of the matrices proper without the tungsten carbides was conduced separately. The results are given in the same work.

From the given results it is clearly seen that the composition in which a relatively soft copper-nickel austenitic cast iron Ni-resist (No. 2) is used as the binder alloy has the highest wear resistance in the

Table 3. Results of wear resistance testing of the deposited alloys

Type of binder alloy	Loss of sample weight, g		Binder alloy hardness, *HRC*
	Pure binder alloy	Composite alloy (binder alloy + tungsten carbides)	
1. 08Kh18N9	0.412	0.221	140 *HB*
2. 270N15D7Kh3S2	0.382	0.018	26
3. 220Kh18F7N3M2	0.048	0.028	46
4. 300F11Kh6NM	0.068	0.092	60
5. 300Kh30N4S2	0.072	0.062	54
6. Ni–Si–B–C	–	0.055	50

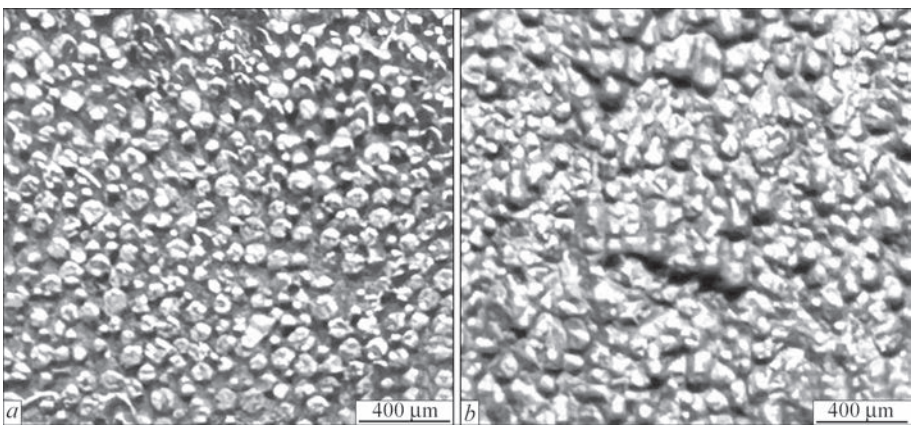

Figure 9. Texture of friction surfaces of the deposited composite alloys after testing: *a* — 270N15D7Kh3S2 (No. 2) + tungsten carbides; *b* — 300F11Kh6NM (No. 4) + tungsten carbides

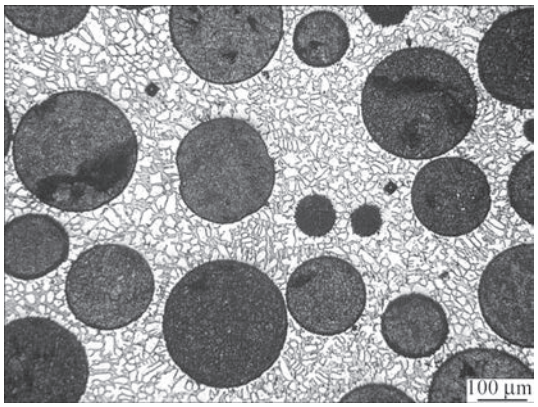

Figure 10. Deposited metal microstructure

abrasive wear conditions. Compared to pure alloy, the deposited metal wear resistance when adding tungsten carbides to it rose more than 20 times. This is due to the fact that this alloy holds the tungsten carbide grains in the matrix very well, forcing them to take on all the wear energy. Tungsten carbide grains on the friction surface wear relatively evenly, maintaining a flat round shape (Figure 9).

Figure 10 is the microstructure of this composite deposited metal, which clearly shows the shape and distribution of the spherical tungsten carbide grains in the matrix. As we can see, they are well preserved without any noticeable melting or dissolution. The matrix proper has a fine-grained eutectic structure, consisting of an iron-based solid solution and carbides of cementite type $(Fe, Cr)_3C$. No free graphite is visible.

A somewhat worse result was demonstrated by the variant with the austenitic-martensitic matrix 220Kh18F7N3M2 (No. 3) (Figure 8). At the same time, it is worth mentioning that the wear resistance of this composition with tungsten carbides, compared to the pure alloy, increased only slightly, just 1.7 times. The alloy proper without the tungsten carbides resists wear well, due to the presence in its structure of up to 70 % of metastable alloyed austenite and a large quantity of primary vanadium carbides VC [8]. During friction such austenite transforms into deformation martensite, while absorbing the fracture energy.

The hope for a high wear resistance of the composition with binder alloy 300F11Kh6NM (No. 4) was not

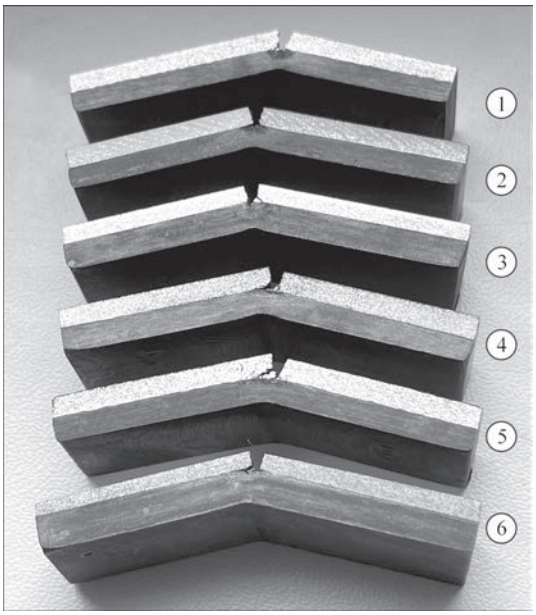

Figure 11. Deposited samples after testing for delamination from the base during bending. Sample numeration is given according to Table 2

justified. Despite the high hardness of the binder alloy (60 *HRC*) and large quantity of vanadium carbides in it, its wear resistance is generally not high (Figure 8). Paradoxically, it is lower than that of the pure alloy. The explanation of that may be that the hard martensitic matrix does not hold the carbide grains well, which under such conditions are just torn out and are carried out of the friction zone together with the matrix and thus the wear resistance is reduced. This is clearly visible in the texture of the friction surface (Figure 9). Since the density of tungsten carbides is much higher than that of the matrix, its influence on the total loss of sample weight is more noticeable in this case.

Wear resistance is not noticeably increased in composition No. 5 based on 300Kh30NH4S2 (Sormite 1), either, by just 12–15 %. Here also the strength of tungsten carbide grains fixing to the matrix plays a role.

Composition No. 6 (Durmat 61-PTA) based on nickel alloy of Ni–Si–B system showed a good result (Figure 8), although it is noticeably inferior to compositions Nos 2 and 3. This leads to the conclusion that the latter can be a good replacement for it.

Figure 12. Examples of effective application of PTA surfacing of a composite alloy with 270N15D7Kh3S2 binder alloy: *a* — tangential cutter; *b* — calibrator; *c* — leveling valve of blast furnace

DEPOSITED METAL DELAMINATION

Results of testing the deposited samples for delamination are shown in Figure 11. As we can see, the deposited layer fracture is brittle in all the compositions, without bending. All the samples have one crack each in the site of load application. No delamination from the base metal was noted. This gives grounds to state that the deposited metal adhesion to the base in all the variants of the composition is strong, and under the real conditions presence of cracks in it should not have any noticeable influence on its total performance.

Thus, analysis of laboratory studies showed that there are iron-based alloys, which cannot be used as the binder alloys for PTA surfacing with composite alloys based on tungsten carbides, and there are alloys which are highly promising for this purpose, for instance Nos 2 and 3 (Table 1).

Alloy No. 2 (270N15D7Kh3S2) was selected for industrial trials, which showed the best wear resistance and good formation of the deposited metal.

Figure 12 shows examples of effective application of PTA surfacing of the composite alloy using this binder alloy.

CONCLUSIONS

1. Iron-based alloy can be used with success as binder alloy for PTA surfacing of tungsten carbides. However, one should not use alloys, which, in combination with tungsten carbides significantly increase their hardness during surfacing, thus lowering the ductility. The high hardness impairs the fixation of the tungsten carbide grains, they are torn off, as a result of which a high wear resistance of the deposited metal is not achieved.

2. Wear-resistant alloys with a high hardness when applied as the binder alloy do not provide any noticeable increase in the deposited metal wear resistance.

3. The relatively soft copper-nickel austenitic cast iron Ni-resist yielded the best result as the binder alloy. It provides excellent formation of the deposited metal, high wear resistance, and it is not too prone to cracking. This alloy can be recommended for wide application as a binder alloy for PTA surfacing based on tungsten carbides.

REFERENCES

1. Harper, D., Gill, M., Hart, K.W.D., Anderson, M. (2002) Plasma transferred arc overlays reduce operating costs in oil sand processing. In: *Proc. of Inter. Spray Conf. on YTSC 2002, Essen, Germany, May*, 278–283.
2. Bouaifi, B., Reichmann, B. (1998) New areas of application through the development of the high-productivity plasma-arc powder surfacing process. *Welding and Cutting*, 50(**12**), 236e–237e.
3. Som, A.I. (1999) New plasmatrons for plasma-powder surfacing. *Avtomaticheskaya Svarka,* **7**, 44–48.
4. Som, A.I. (2004) Plasma-powder surfacing of composite alloys based on cast tungsten carbides. *The Paton Welding J.,* **10**, 43–47.
5. Renyue Yuan, Xuewei Bai, Haozhe Li et al. (2021) Effect of WC content on microstructure, hardness, and wear properties of plasma cladded Fe–Cr–C–WC coating. *Materials Research Express,* 8(**6**), 066302. DOI: https://doi.org/10.1088/2053-1591/ac0b79
6. Fischer, J. (2022) Properties and applications of Ni-resist and ductile Ni-resist alloys. 2nd Edition. www: https://nickelinstitute.org/media/8da7c3cd6014c9b/11018_properties_and_applications_of_ni-resist_alloys.pdf
7. Pereplyotchikov, E.F., Ryabtsev, I.A., Gordan, G.M. (2003) High-vanadium alloys for plasma-powder cladding of tools. *The Paton Welding J.*, **3**, 14–17.
8. Som, A.I. (2016) Iron-based alloy for plasma-powder surfacing of screw conveyors of extruders and injection molding machines. *The Paton Welding J.,* **7**, 21–25. DOI: https://doi.org/10.15407/tpwj2016.07.04)
9. Frumin, I.I. (1977) Modern types of clad metal and their classification. In: *Theoretical and technological fundamentals of cladding. Clad metal.* Kyiv, Naukova Dumka, 3–17.
10. Zhudra, A.P. (2014) Tungsten carbide based cladding materials. *The Paton Welding J.,* **6–7**, 66–71. DOI: https://doi.org/10.15407/tpwj2014.06.14
11. Yuzvenko, Yu.A., Gavrish, V.A., Marienko, V.Yu. (1979) Laboratory units for assessment of wear resistance of clad metal. In: *Theoretical and technological fundamentals of cladding. Properties and tests of clad metal.* Kyiv, PWI, 23-27.
12. Augustine Nana Sekyi Appiah, Oktawian Bialas, Artur Czupryński, Marcin Adamiak (2022) Powder plasma transferred arc welding of Ni–Si–B+60 wt% WC and Ni–Cr–Si–B+45 wt% WC for surface cladding of structural steel. *Materials,* 15(1**4)**, 4956. DOI: https://doi.org/10.3390/ma15144956

ORCID

O.I. Som: 0009-0009-4152-4832

CORRESPONDING AUTHOR

O.I. Som
Plasma-Master Co., Ltd.
3 Omelian Pritsak Str., 03142, Kyiv, Ukraine
E-mail: info@plasma-master.com

SUGGESTED CITATION

O.I. Som (2025) Iron-based binder alloy for plasma transferred-arc surfacing of composite alloys reinforced with cast tungsten carbides.
The Paton Welding J., **8**, 68–74.
DOI: https://doi.org/10.37434/tpwj2025.08.07

JOURNAL HOME PAGE

https://patonpublishinghouse.com/eng/journals/tpwj

Received: 10.04.2025
Received in revised form: 26.06.2025
Accepted: 04.08.2025

PATON INTERNATIONAL — EVOLUTIONS IN YEARS

The history of welding equipment manufacturing in Ukraine spans nearly a century. For over six decades, this legacy has been intrinsically linked to **PATON INTERNATIONAL**, a company **founded in 1959** at the renowned E.O. Paton Electric Welding Institute. Established to bring cutting-edge welding technologies developed by the Institute to market, PATON INTERNATIONAL has since produced hundreds of thousands of units of welding equipment for industries across virtually every continent. Today, PATON INTERNATIONAL stands as a leading Ukrainian manufacturer of welding equipment and consumables and holds a prominent position in the markets of the CIS region.

PATON's **two production facilities in Kyiv** form the nucleus of its operations. These facilities collaborate closely with the E.O. Paton Electric Welding Institute, one of the world's foremost research centers in the field of welding. The company's in-house R&D laboratories manage every aspect of product development — from mechanical design and enclosure fabrication to the creation of advanced electronic circuits and proprietary software. As a result, PATON currently **manufactures over 60 models** of welding equipment, including:

- manual arc welding (**MMA**) inverters rated from 150 to 630 A;
- **MIG/MAG** semi-automatic welding machines from 150 to 630 A;
- argon arc (**TIG**) inverters from 200 to 350 A;
- air-plasma cutting machines (**CUT**) from 40 to 100 A;
- **multifunctiona**l welding inverters from 250 to 350 A.

PATON equipment integrates components sourced from leading global manufacturers such as **INFINEON**, **VISHAY, KENDEIL, NXP, TOSHIBA, and TEXAS INSTRUMENTS**. Complemented by high-quality welding accessories produced in Germany and Ukraine, the equipment reflects the company's commitment to excellence. This dedication is backed by extended **warranties of up to 5 years**, demonstrating PATON's confidence in the durability and reliability of its products.

In addition to equipment, PATON INTERNATIONAL **produces a comprehensive range of welding accessories and electrodes**, including the 10 most popular grades that meet international standards such as **AWS 5.1:E6013, E7015, E7018; A5.4:E347-16; 5.15:ESr; and EN 14700: E Z Fe14.** Manufactured using refined formulations and raw materials from top-tier Ukrainian and international suppliers, PATON electrodes are certified by leading international quality bodies and are known for their excellent performance, arc stability, and user-friendly operation.

At the end of 2024, PATON once again reaffirmed its position as a technological leader by launching a **new generation of welding machines**. This release is the result of continuous improvement driven by feedback from professional welders and the evolving needs of modern manufacturing. Rather than being a routine upgrade, the

new generation marks a significant leap forward in welding technology.

At the core of the new series is a completely redesigned hardware architecture that operates **five times faster** than its predecessor. This advancement enables much higher precision and responsiveness in controlling the welding process. User experience has also seen a major boost: a new encoder makes parameter adjustments intuitive, while a large **LCD display with a graphical interface** provides clear, real-time visual feedback during setup and operation.

The feature set has been significantly expanded, with enhancements to existing functions and the introduction of entirely new ones, including **inductance adjustment**, **Smart Stop**, **SPOT mode**, **PULSE welding**, and more. The interface now updates dynamically in real time, giving welders complete visibility and control throughout the welding process.

Thanks to its engineering innovations, high manufacturing standards, and decades of expertise, PATON's products enjoy strong recognition among welding professionals both in Ukraine and around the world. Expanding its global reach remains a strategic priority for PATON. Today, the **company exports to over 50 countries**, spanning Latin America, Europe, Asia, Africa, and Australia.

One of PATON's top priorities is strengthening its position on the European market — and it's making bold strides forward.

By combining European-level quality, cutting-edge functionality, energy efficiency, and compact design, PATON delivers a powerful alternative to many global brands. And to ensure maximum convenience for European customers, the company has established official branches in Poland (**PATON Europe**) and the United Kingdom (**PATON Welding UK Ltd**). These regional offices oversee logistics, service, and product distribution across the EU and the UK — bringing PATON even closer to its customers.

To make PATON equipment more accessible than ever, the company has gone far beyond the traditional distributor model. PATON INTERNATIONAL has launched over 30 official regional online stores and ensured its presence on nearly all major European and global e-commerce platforms — **Amazon, eBay, Kaufland, CDiscount, OnBuy, Leroy Merlin, Rakuten**, and more. Whether you're a DIY enthusiast or an industrial professional, finding and ordering PATON products is just a few clicks away.

And there's even more good news for European buyers: thanks to partnerships with leading financial platforms like **PayPal, Klarna, Comgate, Santander**, and others, PATON equipment can now be purchased in convenient monthly installments. High-quality welding solutions are now more affordable and accessible than ever.

What truly sets PATON apart is its absolute transparency and confidence in the quality of its products. With one of the longest warranty periods on the market, PATON proudly stands behind every machine it builds. The company is also actively represented on top reputation platforms like **Trustpilot** and **Trustmate**, where real users and customers freely share their experiences, leaving honest and qualified reviews.

PATON INTERNATIONAL is not just a manufacturer — it's a driver of innovation. Constantly investing in research and development, the company is committed to its global mission: to empower welders around the world with accessible, reliable, and high-performance welding solutions.

Learn more at **paton-welding.com/en**